University of Alberta

Generation of Electromagnetic Ion Cyclotron (EMIC) Waves in a Compressed Dayside Magnetosphere

by

Maria E. Usanova

A thesis submitted to the Faculty of Graduate Studies and Research in partial fulfillment of the requirements for the degree of Doctor of Philosophy

Department of Physics

©**Maria E. Usanova**
Fall 2010
Edmonton, Alberta

Examining Committee

Prof. Ian R. Mann, Physics

Prof. Richard D. Sydora, Physics

Prof. Frances R. Fenrich, Physics

Prof. Carlos F. Lange, Mechanical Engineering

Prof. Brian J. Anderson, Applied Physics Laboratory, The Johns Hopkins University, Laurel, Maryland, USA

Abstract

Electromagnetic Ion Cyclotron (EMIC) waves are believed to play an important role in the dynamics of energetic particles (both electrons and ions) trapped by the Earths magnetic field causing them to precipitate into the ionosphere via resonant interaction. In order to incorporate the EMIC-related loss processes into global magnetospheric models one needs to know solar wind and magnetospheric conditions favourable for EMIC wave excitation as well as the localization of the waves in the magnetosphere. EMIC waves are generated by anisotropic ($T_\perp / T_\parallel > 1$) ion distributions. Generally, any process that leads to the formation of such distributions may be responsible for EMIC wave initiation. This thesis discusses magnetospheric compression as a new principal source of EMIC wave generation in the inner dayside magnetosphere.

First, using ground-based and satellite instrumentation, it is shown that EMIC waves are often generated in the inner dayside magnetosphere during periods of enhanced solar wind dynamic pressure and associated dayside magnetospheric compression. The compression-related EMIC wave activity usually lasts for several hours while the magnetosphere remains compressed. Also, it is demonstrated that EMIC waves are generated in radially narrow (~ 1 R$_e$ wide) region of high plasma density, just inside the plasmapause.

Test particle simulations of energetic ion dynamics performed for this study confirmed that anisotropic ion distributions are generated in the compressed dayside magnetosphere, the temperature anisotropy being dependant on the strength of magnetospheric compression. It is found that in the inner magnetosphere these anisotropic particle distributions are formed due to particle drift

shell-splitting in an asymmetric magnetic field.

Finally, the generation of EMIC waves was studied self-consistently using a hybrid particle-in-cell code in order to determine whether the degree of anisotropy estimated from the test particle simulations is sufficient to produce EMIC waves like those detected and to explain some of the observed wave properties.

Acknowledgements

Table of Contents

List of Tables

List of Figures

List of Symbols and Abbreviations

α	pitch angle
β	plasma beta, i.e. thermal to magnetic pressure ratio
γ	growth rate
ϵ_0	vacuum dielectric constant
λ	wavelength
μ_0	free space magnetic permeability
μ	magnetic moment
Ω	cyclotron frequency
$\omega = \Omega + i\gamma$	complex instability frequency
ω_{pi}	ion plasma frequency
ω_{pe}	electron plasma frequency
ρ	charge density
θ	angle between a wavevector and magnetic field direction
A	temperature anisotropy, i.e. $T_\perp/T_{||}$
AE	auroral electrojet index
B	magnetic field
c	speed of light
CARISMA	CARISMA magnetometer array

Cluster	Cluster satellite
Dst	worldwide magnetic storm time disturbance index
$\mathbf{E}$	electric field
E	particle kinetic energy
EMIC	electromagnetic ion cyclotron
f	particle distribution function
GOES	GOES satellite
IMF	interplanetary magnetic field
$\mathbf{j}$	electric current density
$\mathbf{k}$ and k	wavevector and wavenumber
Kp	Kp index
L	L-shell or L-value
LEO	low Earth orbit
M	Earth's dipole moment
m	particle mass
m_i and m_e	ion and electron masses
MLT	magnetic local time
n	particle number density
NOAA	NOAA satellite
OMNI	combined solar wind data
PSD	phase space density
q	elementary charge
R_e	Earth's radius
STEP	STEP magnetometer array
$T_\perp$ and $T_\parallel$	perpendicular and parallel temperatures

THEMIS   THEMIS satellite

ULF   ultra low frequency

UT   universal time

$v_\perp$ and $v_\parallel$ perpendicular and parallel speed

V_A Alfvén speed

$v_{th,i}$ ion thermal speed

$v_{th,e}$ electron thermal speed

$\mathbf{v_{ph}}$ wave phase velocity

Z plasma dispersion function

Chapter 1

Solar-Terrestrial Environment

1.1   The Sun and the Solar Wind

The Sun is a plasma ball with radius $R_\odot = 6.96 \cdot 10^8$ m and mass $M_\odot = 1.99 \cdot 10^{30}$ kg consisting of $\sim 90\%$ (in number density) of hydrogen, $\sim 10\%$ of helium and $\sim 1\%$ of 67 other elements *Parks* (2004).

The solar plasma is not evenly distributed but forms distinct layers shown in Figure 1.1. The core of the Sun is the hottest (13.6 MK) and the most dense (150 g/cm^3) region which produces energy by thermonuclear reactions and powers the star and the entire solar system. The heat is transferred outwards from the core in the so-called *radiative zone*, where the density gradually drops from 20 g/cm^3 to 0.2 g/cm^3. Above this layer (at distances of $\sim 0.7 - 0.8$ $R_\odot$) thermal convection becomes more efficient in transporting the energy outward. On top of the *convective layer*, lies the visible surface of the Sun, the *photosphere*, which is only ~ 350 km wide. The photosphere radiates electromagnetic energy as a black body at temperature ~ 6000 K. The environment directly above the pho-

tosphere is referred to as the solar atmosphere including the *chromosphere* and *corona*, the upper atmosphere of the Sun.

The *solar wind* is a continuous outflow of plasma from the solar corona due to its expansion into the interplanetary space. It consists of mainly protons and electrons, and a less than 10% (in number density) admixture of helium and heavy atoms. The solar wind is divided into two components, called the *slow* and the *fast solar wind*. The slow solar wind originates from the equatorial regions of the Sun, has a velocity of $300 - 400$ km/sec and a density of up to ~ 60 cm^{-3} (measured upstream of the Earth). In contrast, the fast solar wind is released from the polar regions with a speed of $600 - 1400$ km/sec and has a typical density of $2 - 5$ cm^{-3}. The solar wind also carries the "frozen in" coronal magnetic field forming the *interplanetary magnetic field* (IMF) which, despite having a relatively small energy density ($\sim 1\%$ of solar wind kinetic energy), plays an important role in the interaction among different objects in the Solar system. The combination of expansion and rotation of the Sun gives the IMF its shape resembling the Archimedean spiral and named the Parker spiral (shown in Figure 1.2). At the Earth's orbit the angle between the IMF and the sunward direction is $\psi \approx 45°$. The solar wind flows generated above regions of the Sun with opposite magnetic field polarity carry IMF with corresponding direction (towards or away from the Sun), and thus divide the interplanetary space into sectors of opposite IMF orientation. As the Sun rotates, the Earth moves from one sector into another. During the years of minimum solar activity, these sectors of opposite IMF "polarity", cause regular disturbances of the geomagnetic field, repeating every 27.4 days (the period of solar equatorial rotation in the Earth's frame).
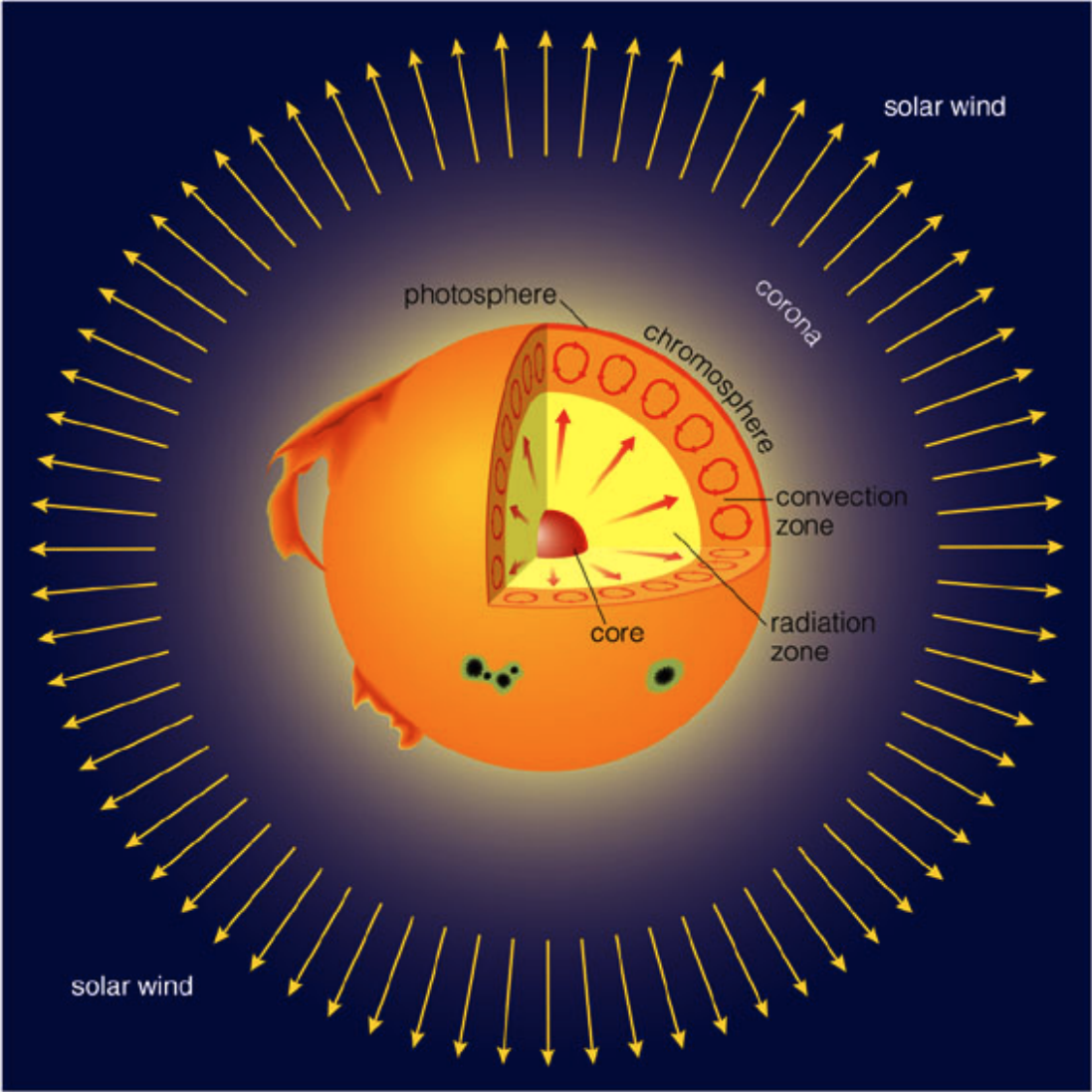
Figure 1.1: Schematic illustration of the internal Sun structure. Image taken from http://www.physast.uga.edu/ rls/astro1020/ch15/ovhd.html.
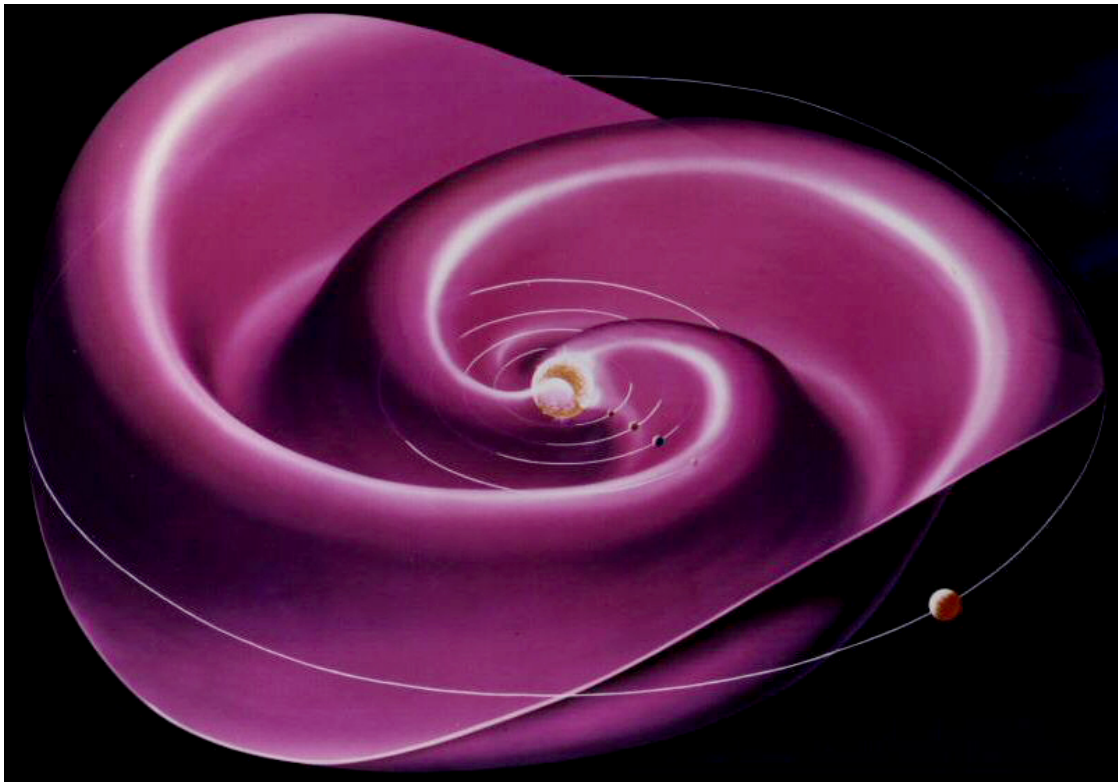
Figure 1.2: A 3D model of the Parker spiral. Image courtesy of NASA (taken from Wikipedia).

Superposed on top of the steady expansion of the upper corona, there are also non-stationary processes in the solar corona that lead to a plasma ejection and cause non-recurrent disturbances of the geomagnetic field. These processes often give rise to the largest geomagnetic storms. Unstable regions in the solar corona can release large amounts of energy and matter called *coronal mass ejections* (CMEs) which occur most often during the maximum of the 11-year solar cycle. It takes around two days for a large CME to reach the Earth and cause a magnetic storm. The major features of a magnetic storm are the enhanced magnetospheric convection, injection of energetic particles into near-Earth space and resulting strong depression of the terrestrial magnetic field. We will consider this process in more detail in the following sections.

1.2 The Earth's Magnetosphere

As the solar wind moves with supersonic (with respect to the surrounding interplanetary medium) speed, a bow shock is formed upstream of the Earth. Behind the bow shock, the solar wind slows down and kinetic energy is transformed into thermal energy, creating the region called the *magnetosheath*.

The solar wind deforms the terrestrial magnetic field, producing the asymmetric field configuration shown in Figure 1.3, compressed on the dayside and elongated on the nightside, and creates a cavity in the interplanetary medium called the *magnetosphere*. The shape of the magnetosphere is defined by the dynamic equilibrium between the solar wind dynamic pressure $P_{dyn} = n_{sw} m_i v_{sw}^2$ (neglecting electron mass) and the Earth's magnetic field pressure $p_B = B^2/2\mu_0$, where n_{sw}, m_i and v_{sw} are the average number density, mass and flow speed of
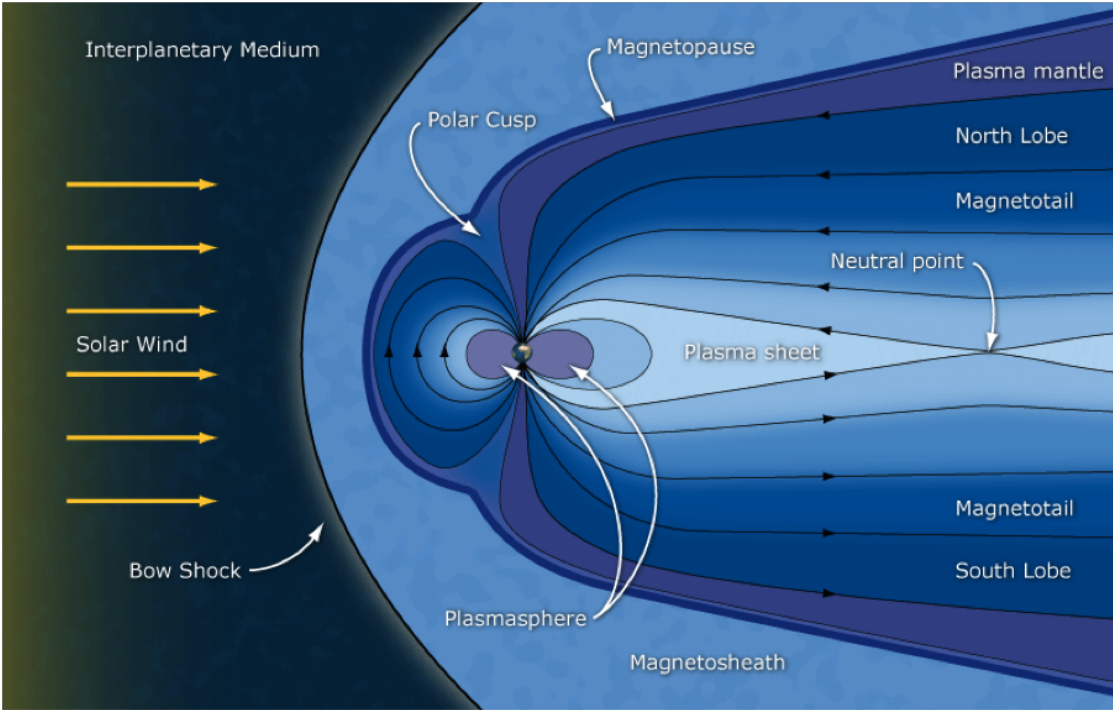
Figure 1.3: Schematic illustration showing different regions of the magnetosphere. Image courtesy of ESA (taken from http://sci.esa.int/science-e-media/img/be/Earth-Magnetosphere.gif).

the solar wind, respectively, B is the Earth's magnetic field strength and μ_0 is the magnetic permittivity of vacuum. The surface where the solar wind dynamic pressure equals the geomagnetic field pressure is named the *magnetopause*. The standoff distance of the Earth's magnetopause in the subsolar direction depends mostly on P_{dyn} and is approximately 10 Earth's radii (R_e).

1.2.1 Magnetospheric Convection

The magnetosphere constantly undergoes dynamic interaction with the solar wind plasma producing the Dungey convection cycle (*Dungey*, 1961). *Dungey* (1961) showed that magnetic merging (reconnection) of antiparallel magnetic field lines where those in the solar wind meet those for the Earth, drives the concurrent drift of plasma and magnetic field lines around the Earth. The Dungey cycle is illustrated in Figure 1.4 (a - i). When a southward directed IMF (negative IMF B_z) encounters the magnetopause (a) it will reconnect with the closed northward magnetic field line (b) and will split it into two open field lines (c). Further, the solar wind will transport these field lines across the polar cap towards the nightside magnetosphere (d - e). At distances $\sim 100\,R_e$ in the nightside the two open field lines will meet and merge again (f). Further, these newly reconnected nightside field lines will move in the earthward direction bringing along the plasma "frozen into" the magnetic field lines (g). The field line will finally drift around the Earth and toward the frontside magnetosphere (h - i). During the sunward transport of plasma from the magnetotail the associated dawn-to-dusk convection electric field (E $\sim 0.2-0.5\,\mathrm{mV/m}$) will be created. The amplitude of the convection electric field depends on the strength of magnetospheric convection and is defined by the solar wind speed, and the magnitude

and the sign of IMF B_z (see, e.g., *Hori et al.*, 2005).
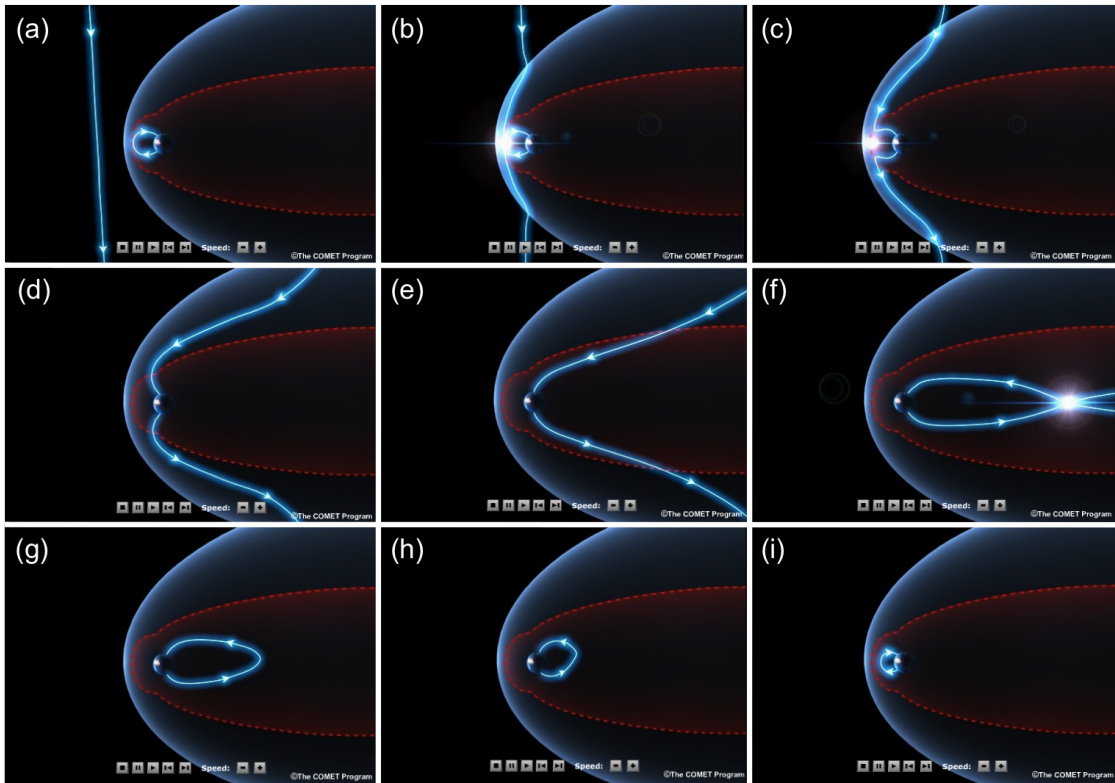
Figure 1.4: Magnetospheric Dungey convection cycle. Image adapted from the animation taken from http://www2.ucar.edu. Courtesy of UCAR.

1.2.2 Magnetospheric Regions

When dayside reconnection opens geomagnetic field lines at the magnetopause, hot solar wind plasma from the magnetosheath accesses the magnetosphere producing the dayside cusp and plasma mantle. As the open field lines continue their motion across the polar cap towards the magnetotail they fill with cold ionospheric plasma producing mixed plasma of both ionospheric and solar wind in the *magnetotail lobes*. After magnetic field line reconnection in the magnetotail, the closed field lines moving inward compress the plasma form-

ing the *plasmasheet*. While the field line approaches the Earth, the particle energy increases. In addition, due to the inhomogeneous magnetic field the energetic particles start drifting around the Earth (electrons – eastwards and protons – westwards), producing the *ring current*. The ring current creates a magnetic field directed opposite to the geomagnetic field. The strength of the magnetic field induced by the ring current depends on the ring current density and during magnetic storms may cause substantial depressions of the Earth magnetic field. The ring current is created mainly by $10 - 200$ keV plasmasheet protons
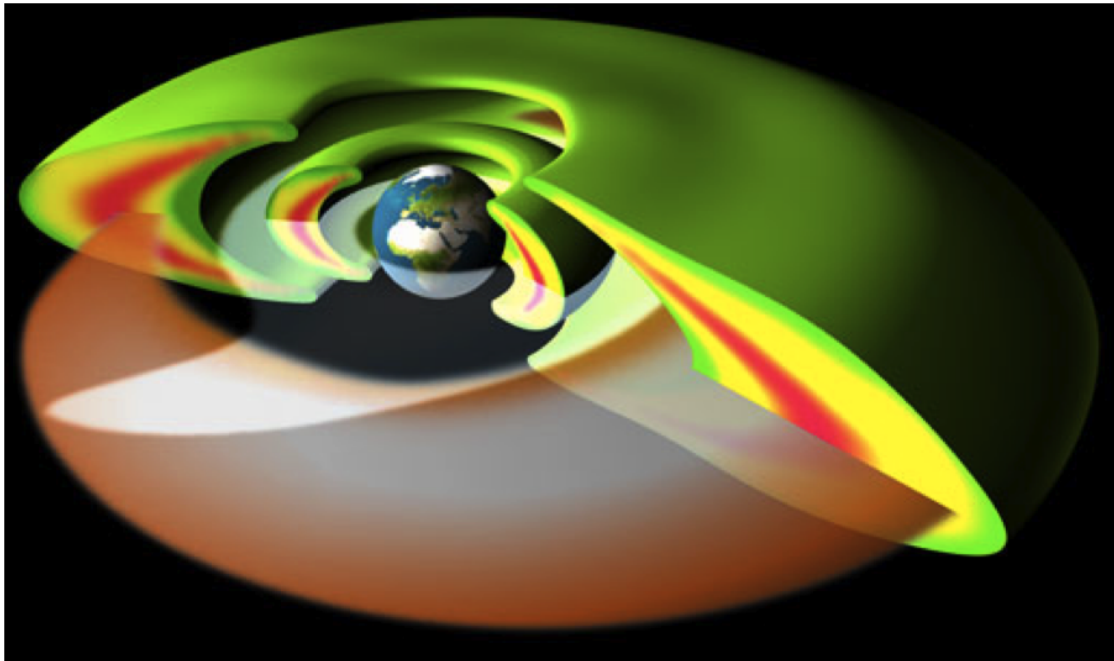
Figure 1.5: Schematic illustration of the Earth's inner and outer radiation belts and the ring current. The intensity of particle fluxes in the inner and the outer radiation belt is denoted by the green (minimum intensity) to red (maximum intensity) colour. The equatorial ring current is shown by the orange shaded area. Courtesy of NASA.

and also by He^+ and O^+ ions of ionospheric origin. *Daglis et al.* (1999) estimated the composition of the ring current heavy ions and found that O^+ constitutes

5% of the ring current population during undisturbed geomagnetic conditions, significantly increasing in intense storms up to $\sim 21\%$, $\sim 3\%$ of the ring current consists of α-particles (He^{++}) and $\sim 1\%$ of He^+.

The region between $3 - 6$ R_e is also populated by MeV electrons forming the *outer radiation belt*. This population can pose danger to astronauts working in orbit and damage space-borne instrumentation and satellites. Another energetic population called the *inner radiation belt* lies at distances between $1.5 - 2$ R_e. It contains protons with energies around tens of MeV produced as a result of nuclear reactions of atmospheric atoms with cosmic rays and lower energy protons diffused towards the Earth during geomagnetic storms. A schematic illustration of the ring current and the radiation belts is shown in Figure 1.5.

The region of space below ~ 5 R_e is called the *plasmasphere* and contains a cold ($\sim$ eV) but dense plasma of ionospheric origin that corotates with the Earth (see Figure 1.6). It partially overlaps the ring current and the outer radiation belt. In the plasmasphere, the typical ion number density ratios are $H^+ : He^+ : O^+ = 1 : 0.1 : 0.01$. However, sometimes $He^+ : H^+$ can increase up to 0.5. The boundary of the plasmasphere is called the *plasmapause*. At the plasmapause electron density experiences a gradient, dropping from ~ 1000 to 1 e/cm^3. The region adjacent to the plasmasphere, extended outward by $1 - 2$ R_e is called the exo-plasmasphere (*Young*, 1985) and is hotter than the plasmasphere. It also characterized by larger He^+/H^+ ratios.

As a summary of magnetospheric populations, *Young* (1985) suggested the following classification:

- plasmashere (~ 1 eV)

- exo-plasmashere (1 eV – 1 keV)

- plasma sheet (1 – 10 keV)

- ring current (10 – 300 keV)

- radiation belts ($\geqslant$ 300 keV)

However, the distinctions among these populations are vague since they overlap both in energy and space.
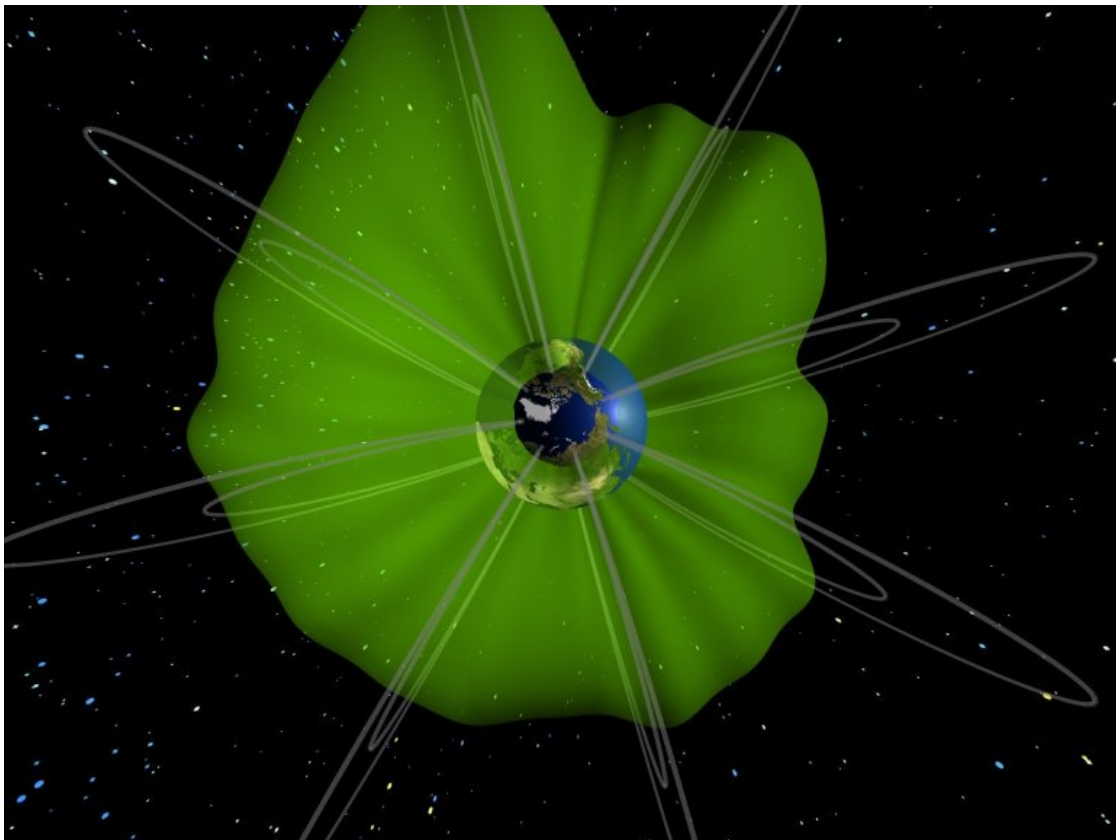
Figure 1.6: A 3D reconstruction of the equatorial profile of the cold plasma density (measured by the IMAGE satellite) by extending the region along field lines of a simple dipole field. Courtesy of NASA.

1.3 Motion of Charged Particles in the Inner Magnetosphere

Traditionally, the region of the magnetosphere located below the geosynchronous orbit (6.6 R_e) is called the inner magnetosphere. In this region, the Earth's magnetic field can be approximated by a dipole field, given in Cartesian coordinates by

$$\mathbf{B}(\mathbf{r}) = -\frac{3Mxz}{r^5}\hat{\mathbf{x}} - \frac{3Myz}{r^5}\hat{\mathbf{y}} - \frac{M(3z^2 - r^2)}{r^5}\hat{\mathbf{z}}, \tag{1.1}$$

where $M = 8.02 \cdot 10^{22}$ Am^2 is the Earth's magnetic dipole moment.

A typical magnetic field line (a tangent line to the magnetic vector field) is shown in Figure 1.7 by the blue color. In space physics, the radius of the Earth is often used as a unit of distance, and a particular field line is labeled by assigning an L-value – a distance between the center of the Earth and the field line in the equatorial plane measured in units of R_e (*McIlwain*, 1961).

Particles trapped in the Earth's magnetic field move under the action of the Lorentz force:

$$m\frac{d\mathbf{v}}{dt} = q(\mathbf{E} + \mathbf{v} \times \mathbf{B}). \tag{1.2}$$

In the presence of a uniform magnetic field, the charged particle with a velocity component perpendicular to the field will gyrate around a field line in a generally circular or helical orbit with gyrofrequency $\Omega = qB/m$. In a magnetic field configuration where the field strength changes along a field line, it will sample some of the field lines that are converging to create the field gradient. The radial component of these field lines, coupled with the azimuthal motion of the particle, will result in a *mirror force* parallel to the field and directed to-
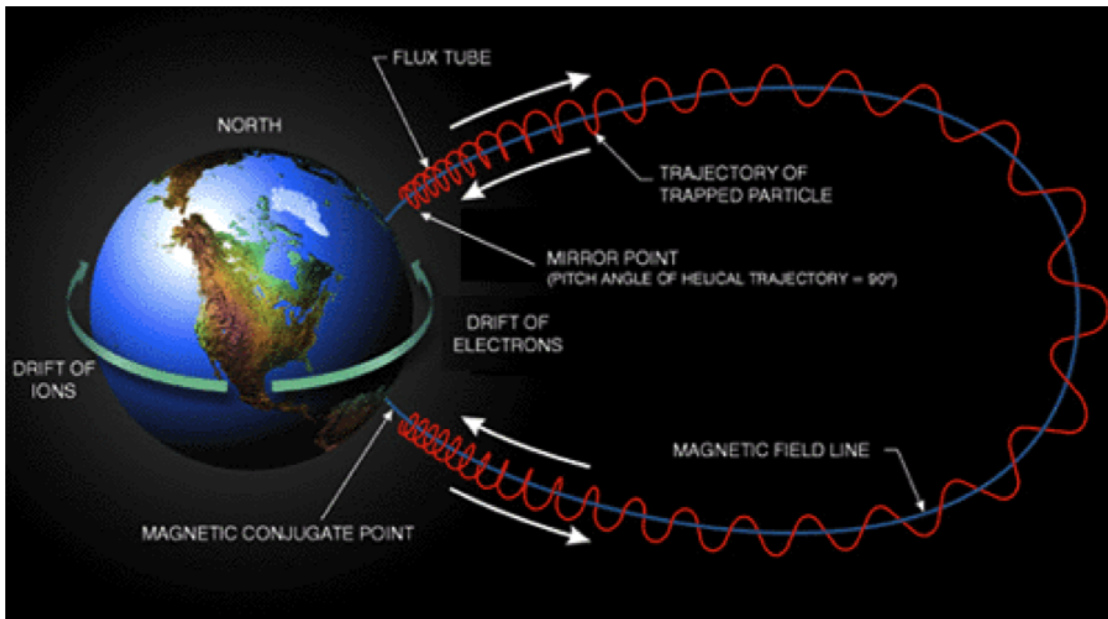
Figure 1.7: Schematic showing the dipole magnetic field line and the trajectory of a charged particle trapped by the Earth's magnetic field. Adapted from Figure 5.10 in (*Jursa, A.S.*, 1985). Image courtesy of SWRI.

ward the region of smaller field strength. The mirror force will cause the particle to change its direction of motion and bounce back and forth along between its mirror points (*Baumjohann and Treumann*, 1996). Locations of the particle's mirror points are defined by the ratio $(v_\perp/v_\parallel)$ or more precisely, the pitch angle $\alpha = \arctan(v_\perp/v_\parallel)$ in the equatorial plane. Particles whose mirror points lie in the atmosphere, will be lost from the magnetosphere due to collisions with atmospheric atoms. The critical value for the particle equatorial pitch angle varies for different L-values. For example, at $L = 6.6$ all particles with equatorial pitch angles less than $3°$ will be lost in the atmosphere, while at $L = 2$ the critical equatorial pitch angle value equals $16°$. If the magnetic field is inhomogeneous the particle will also experience the gradient and curvature drift perpendicular

to both the magnetic field and its gradient with velocity

$$\mathbf{v}_B = (v_{\parallel}^2 + \frac{1}{2}v_{\perp}^2)\frac{\mathbf{B} \times \nabla B}{\Omega B^2},$$ (1.3)

where $v_{\perp}$ and $v_{\parallel}$ are components of the particle's velocity perpendicular and parallel to $\mathbf{B}$, respectively.

Therefore, particles trapped in the Earth's magnetic field experience three kinds of motion: gyration around the magnetic field line, bounce motion along the field line and azimuthal drift across the field lines due to the field inhomogeneity (shown in Figure 1.7). One can show that in relatively slowly varying magnetic field particles will drift conserving the three adiabatic invariants associated with each type of motion: the magnetic moment (1st adiabatic invariant) $\mu = mv_{\perp}^2/2B$, the longitudinal (or 2nd adiabatic) invariant $J = \oint mv_{\parallel}ds$, and the drift (or 3rd adiabatic) invariant $\Phi = 2\pi Mm/q^2$, where M is the Earth's magnetic dipole moment and m and q are the mass and charge of the particle.

In the presence of an electric field, charged particles will also undergo a large-scale $\mathbf{E} \times \mathbf{B}$ drift

$$\mathbf{v}_E = \frac{\mathbf{E} \times \mathbf{B}}{B^2},$$ (1.4)

which plays an important role in the magnetospheric convection. It is independent of the sign of the particle's charge and therefore, electrons and ions will drift in the same direction. It is responsible for a *partial ring current*, caused by the combination of sunward $\mathbf{E} \times \mathbf{B}$ drift and gradient and curvature drifts causing some particles drifting around the Earth to be deflected to the magnetopause and lead to their escape from the magnetosphere.

1.3.1 Characteristic Drift Timescales in the Magnetosphere

Charged particles drift around the Earth on a different timescale depending on particle's energy and pitch angle. The three main drift periods are the magnetic gradient-curvature, the electric convection and the corotation period (*Baumjohann and Treumann*, 1996). The average magnetic gradient-curvature drift speed in a dipole magnetic field is defined by

$$v_d \approx \frac{6L^2 E}{qB_e R_e}(0.35 + 0.15 \sin \alpha_{eq}), \tag{1.5}$$

where $B_e = 3.11 \times 10^{-5}$ T is the equatorial magnetic field strength at the Earth's surface, E is particle energy and α_{eq} is the particle's equatorial pitch angle. The corresponding magnetic gradient-curvature drift period around the Earth is then given by

$$\tau_d \approx \frac{\pi q B_e R_e^2}{3LE}(0.35 + 0.15 \sin \alpha_{eq})^{-1}. \tag{1.6}$$

The sunward convection $\mathbf{E} \times \mathbf{B}$ drift speed mentioned above, can be expressed in the equatorial plane as

$$v_E = \frac{E_{eq} L^3}{B_e}. \tag{1.7}$$

Another electric field drift that affects dynamics of charged particles is the corotation electric field drift due to the Earth's rotation. The corotation drift period is the same as the period of the Earth's rotation about its axis (24 hours).

Figures 1.8 and 1.9 show the corotation period (black curve) and the magnetic gradient-curvature drift periods (blue curves) for equatorially mirroring particles with energies 1 keV, 10 keV, 20 keV, 50 keV, 100 keV, and 200 keV.
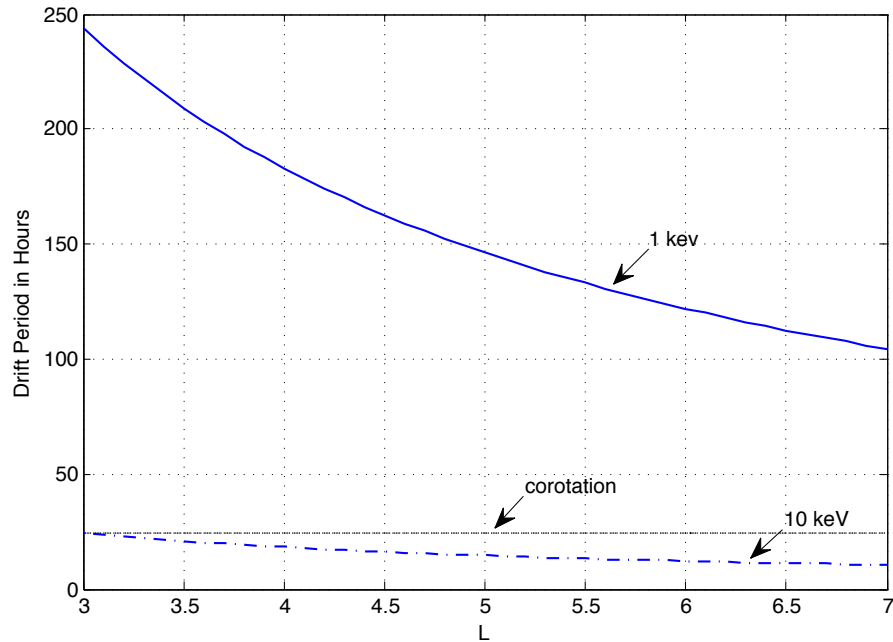
Figure 1.8: Corotation period (black curve) and magnetic gradient-curvature drift periods (blue curves) for 1 keV and 10 keV equatorially mirroring particles.

These figures illustrate that the corotation drift is dominant for particles with relatively low energy (less than ≈ 1 keV), while for higher energy particles the magnetic drift is more important.

A comparison of the magnetic gradient-curvature drift speed for particles with energies 10 keV, 20 keV, 50 keV, 100 keV, and 200 keV and the convection electric field drift speed for electric fields of 0.5 mV/m and 1 mV/m in the equatorial plane as a function of L is shown in Figure 1.10. The convection electric field is assumed to be constant with radial distance. The magnetic gradient-curvature drift speed is larger for more energetic particles, and for less energetic particles the convection electric drift speed becomes more prominent, depending on the electric field strength.
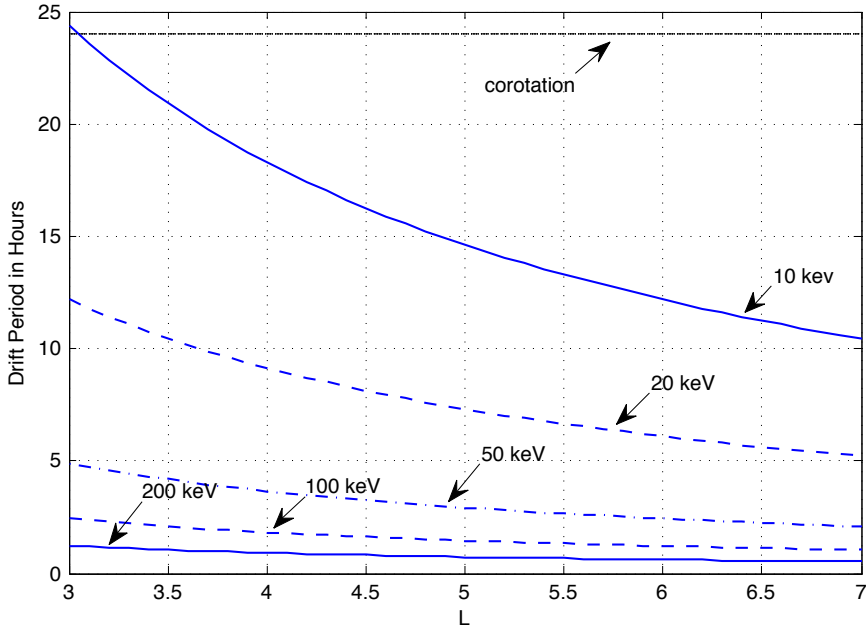
Figure 1.9: Corotation period (black curve) and magnetic gradient-curvature drift periods (blue curves) for equatorially mirroring particles with energies 10 keV, 20 keV, 50 keV, 100 keV, and 200 keV.
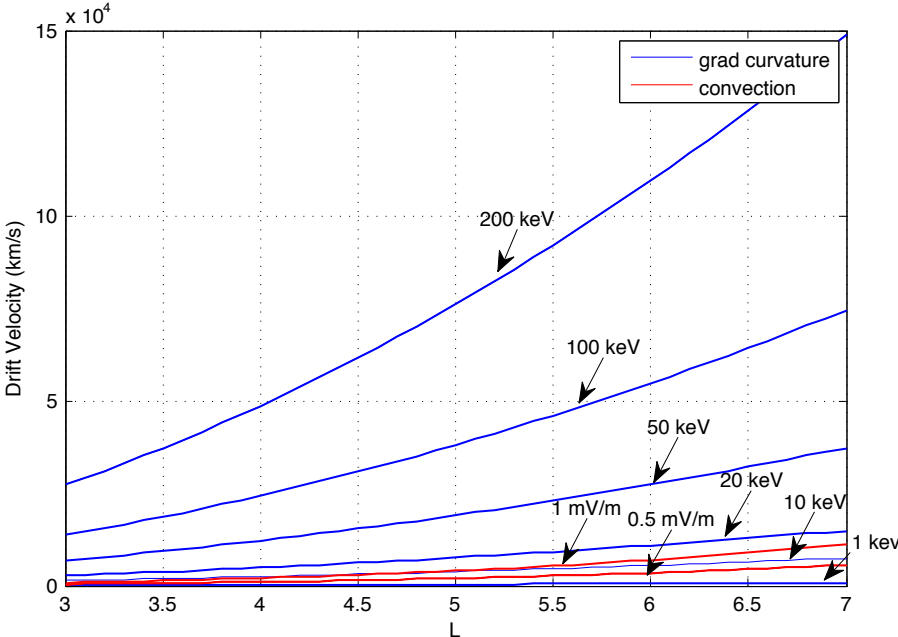
Figure 1.10: Convection electric drift speed (red curves) for $E_{eq} = 0.5$ and 1 mV/m and magnetic gradient-curvature drift speed (blue curves) for equatorially mirroring particles with energies 10 keV, 20 keV, 50 keV, 100 keV, and 200 keV.

1.4   Loss Processes in the Inner Magnetosphere

The ring current is carried almost entirely by ions which transport most of the energy (*Stern*, 2005). Assuming that ring current ions are stably trapped in the inner magnetosphere, their lifetime (on a time scale from several hours to several days) is determined by loss processes due to:

- charge exchange with neutral hydrogen,

- Coulomb collisions,

- wave-particle interactions.

The charge exchange of ring current ions with cold atmospheric hydrogen atoms is the most important loss process (*Jordanova*, 2005). Due to the charge exchange, energetic neutral atoms which are no longer trapped by the magnetic field, are produced and then either precipitate further down into the atmosphere or escape into space. The charge exchange is most efficient for ions with energies $10 - 100$ keV (*Koskinen*, 2005).

Energetic ring current ions can also experience Coulomb collisions with the low-energy plasmaspheric population, which results in energy transfer between the cold and the hot populations as well as in pitch-angle scattering of charged particles. This process is important for protons with energies below 10 keV and heavy ions below ~ 40 keV.

The worldwide magnetic storm time disturbance index (Dst) measured by equatorial ground magnetometer stations serves as a gauge of the ring current strength. Dst reaches its minimum in storm main phase (meaning the ring current build-up) and continuously decays during multiple days following a mod-

erate geomagnetic storm. This slow decay is caused by the loss of energetic protons due to charge exchange and Coulomb collisions. However, during strong geomagnetic storms the Dst relaxation can happen on a timescale of a few hours and is attributed to wave-particle interaction. Loss of energetic protons during magnetic storm was simulated by *Jordanova* (2005), who found that ring current energy losses due to wave-particle interaction are comparable to charge exchange losses near Dst minima.

1.5 Electromagnetic Ion Cyclotron (EMIC) Waves

The waves believed to be responsible for the fast decay of the ring current are the electromagnetic ion cyclotron (EMIC) waves. EMIC waves are left-hand polarized waves with the frequency below the ion cyclotron frequency. The dispersion relation (normalized frequency as a function of the wave number) for an EMIC wave propagating parallel to the magnetic field in a plasma consisting of H^+, He^+, and O^+ species is shown in Figure 1.11. The free energy for EMIC waves is provided by equatorial hot ions with temperature anisotropy ($T_\perp > T_\parallel$) (*Cornwall*, 1965). The excess of perpendicular ion thermal energy is released in the form of EMIC waves.

Energetic particles can resonate with EMIC waves if the Doppler-shifted wave frequency (in the frame of reference of the particle) is equal to a multiple $n = 0, \pm 1, \pm 2, ...$ of the particle cyclotron frequency:

$$\omega - k_{||}v_{||} = n\Omega/\gamma, \tag{1.8}$$
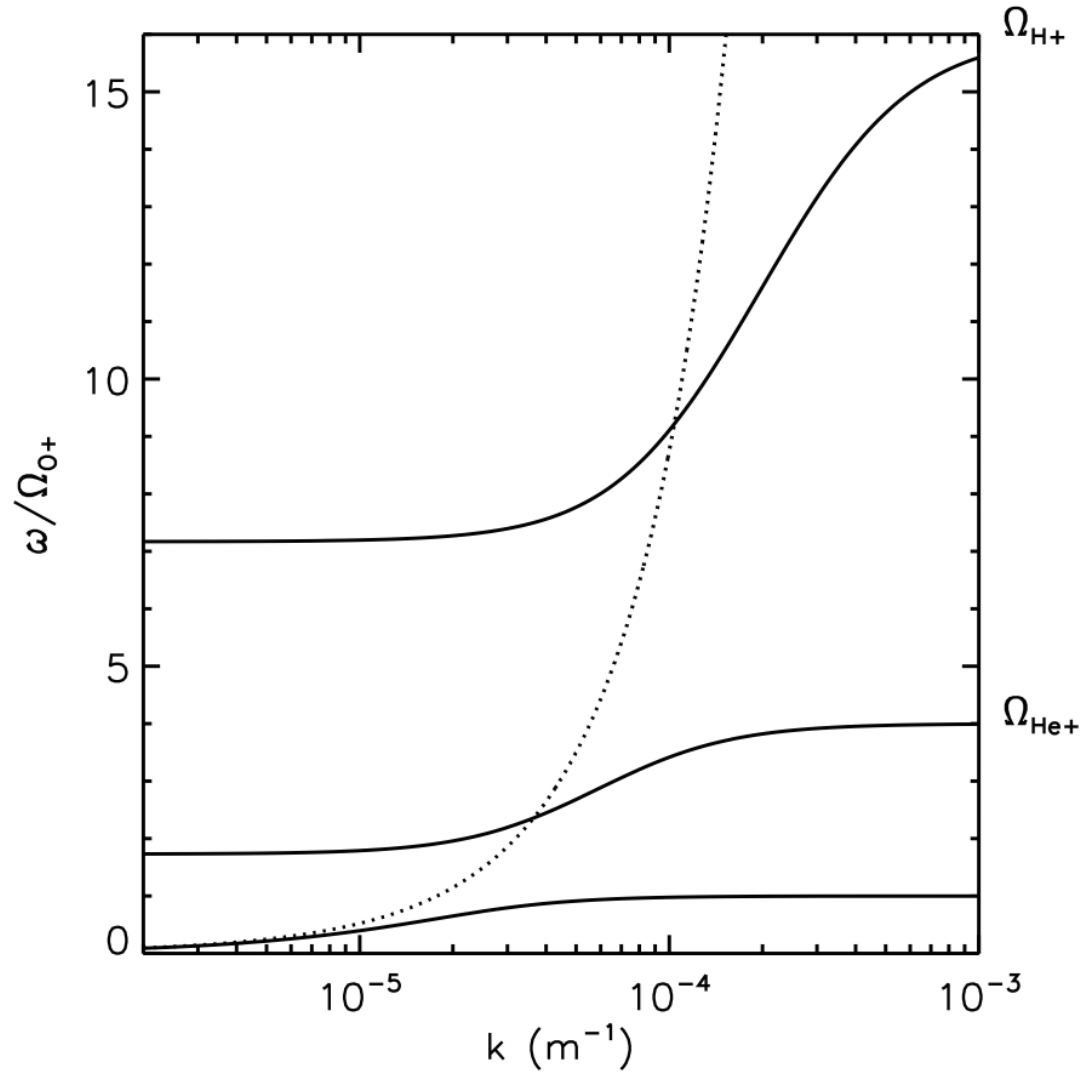
Figure 1.11: EMIC wave dispersion relation for parallel propagation in a plasma composed of $70\%\ H^+$, $20\%\ He^+$, and $10\%\ O^+$ species. The solid curves show the three left-hand polarized modes below the H^+, He^+, and O^+ cyclotron frequencies, respectively. The dashed curve denotes the right-hand polarized mode which becomes important for oblique propagation (not considered in this thesis). Adapted from (*Thorne et al.*, 2006).

where $\gamma = (1 - (v/c)^2)^{-1/2}$ is the relativistic Lorentz factor and $k_{\parallel}$ and $v_{\parallel}$ are components of the wave vector and particle velocity parallel to the background magnetic field. During wave-particle interactions, the waves can exchange energy and momentum with the particles resulting in particle scattering and wave growth or damping. The EMIC wave growth will finally lead to isotropization of the unstable distribution and precipitation of ions into the atmosphere (see Chapter 2 for more details).

As follows from Equation 1.8, EMIC waves can also resonantly interact with electrons. However, electrons must overtake the wave with velocity sufficient to Doppler shift the wave frequency to the relativistic electron cyclotron frequency. It has been shown that in regions of high plasma density the resonance condition may be satisfied for less energetic particles implying that the resonance can take place even for relativistic ($E > 0.5$ MeV) electrons in regions of high background plasma density (*Summers et al.*, 1998).

Summers et al. (1998) suggested that the EMIC wave activity is strongly enhanced in the vicinity of the duskside plasmapause during the main storm phase. Energetic anisotropic ions convected from the plasmasheet continue drifting around the Earth in a clockwise direction, while energetic electrons drift in a counterclockwise direction, as shown in Figure 1.12. EMIC waves are generated along the plasmapause when the energetic ion population overlaps the high density plasmasphere (see discussion in Chapter 2). Due to interaction with the EMIC waves, energetic protons will be eventually lost from the magnetosphere. When electrons reach this region, they also undergo interaction with the EMIC waves and precipitate into the atmosphere.

This scenario of EMIC wave generation and consequent loss of energetic
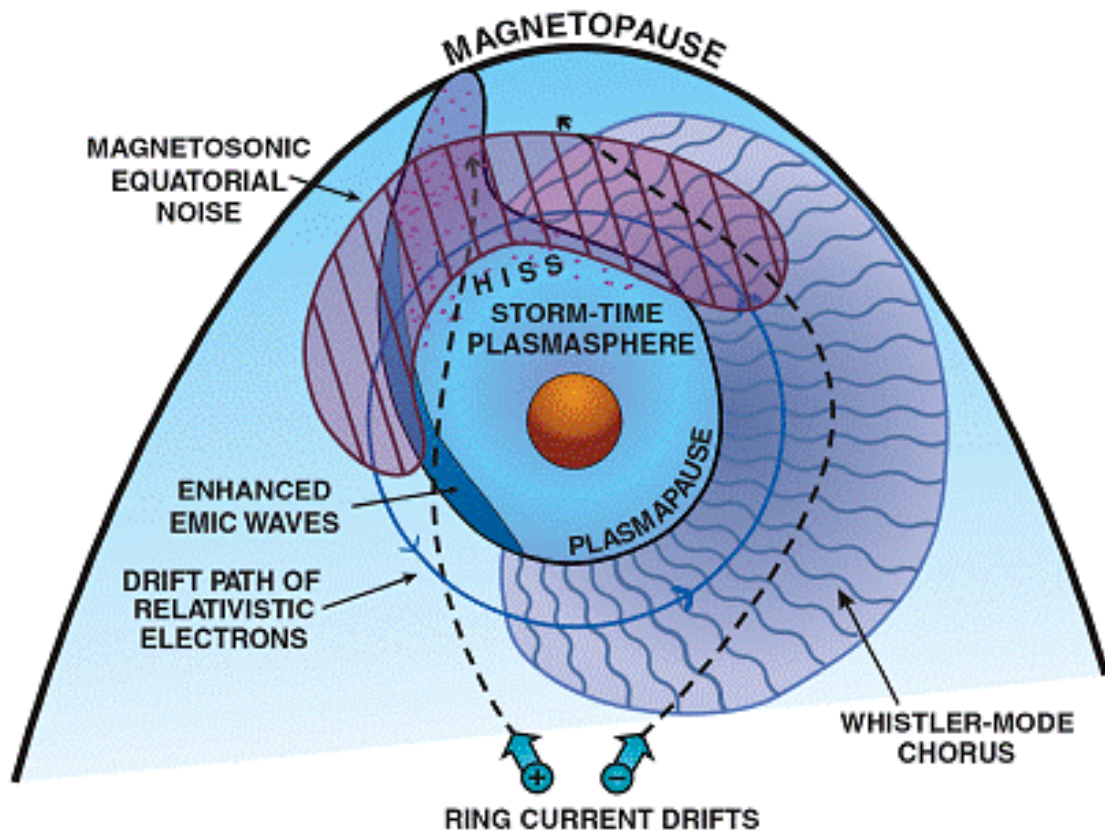
Figure 1.12: Drift paths of radiation belt electrons and energetic ions intersecting the plasmasphere. Image adapted from (*Summers et al.*, 1998), taken from http://www.atmos.ucla.edu/rmt/page5.html.

population has been commonly accepted. However, there are other mechanisms for EMIC wave generation and associated energetic particle loss. Since EMIC waves are believed to play a key role in the dynamics of energetic particles, investigation of all possible conditions leading to EMIC wave generation is of great importance.

1.6 Thesis Outline

In this thesis, we will examine the generation of dayside EMIC waves during magnetospheric compression. In Chapter 2 we will discuss the magnetospheric processes responsible for EMIC wave generation. We will also present observations of dayside EMIC wave activity during magnetospheric compressions and associated loss of energetic particles (ring current protons and MeV electrons). Chapter 3 will examine the physical mechanisms leading to the formation of anisotropic hot proton distributions in the dayside magnetosphere during magnetospheric compressions, providing the source of energy for EMIC instability, through test particle simulations. Chapter 4 will consider the generation of EMIC waves self-consistently by means of kinetic modelling. Finally, in Chapter 5 the conclusions to this study and suggestions for future work will be discussed.

Bibliography

Baumjohann, W., and R. Treumann (1996), *Basic space plasma physics*, Imperial College Press, London.

Cornwall, J. M. (1965), Cyclotron instabilities and electromagnetic emissions in the ultra low frequency and very low frequency ranges, *J. Geophys. Res.*, *70*, 61–69.

Daglis, I., R. Thorne, W. Baumjohann, and S. Orsini (1999), The terrestrial ring current: Origin, formation, and decay, *Rev. Geophys.*, *37*, 407–438.

Dungey, J. (1961), Interplanetary magnetic field and the auroral zones, *Phys. Rev. Letters*, *6*, 47–48.

Hori, T., et al. (2005), Storm-time convection electric field in the near-Earth plasma sheet, *Journal of Geophysical Research (Space Physics)*, *110*, 4213, doi: 10.1029/2004JA010449.

Jordanova, V. (2005), A historical introduction to the ring current, the inner magnetosphere: Physics and modelling, in *The Inner Magnetosphere: Physics and Modeling*, vol. 155, edited by T. Pulkkinen, N. Tsyganenko, and R. Friedel, pp. 9–21, Washington, D.C.

Jursa, A.S. (1985), *Handbook of Geophysics and the Space Environment*, United States Air Force.

Koskinen, H. (2005), A historical introduction to the ring current, the inner magnetosphere: Physics and modelling, in *The Inner Magnetosphere: Physics and Modeling*, vol. 155, edited by T. Pulkkinen, N. Tsyganenko, and R. Friedel, pp. 23–31, Washington, D.C.

McIlwain, C. (1961), Coordinates for mapping the distribution of magnetically trapped particles, *J. Geophys. Res.*, *66*(11), 3681–3691.

Parks, G. (2004), *Physics of space plasmas: an introduction*, Westview Press.

Stern, D. (2005), A historical introduction to the ring current, the inner magnetosphere: Physics and modelling, in *The Inner Magnetosphere: Physics and Modeling*, vol. 155, edited by T. Pulkkinen, N. Tsyganenko, and R. Friedel, pp. 1–8, Washington, D.C.

Summers, D., R. Thorne, and F. Xiao (1998), Relativistic theory of wave-particle resonant diffusion with application to electron acceleration in the magnetosphere, *J. Geophys. Res.*, *103*(A9), 20,487.

Thorne, R., R. Horne, V. Jordanova, J. Bortnik, and S. Glauert (2006), Interaction of emic waves with thermal plasma and radiation belt particles, in *Magnetospheric ULF Waves: Synthesis and New Directions*, vol. 169, edited by K. Takahashi, P. Chi, R. Denton, and R. Lysak, Washington, D.C.

Young, D. (1985), Experimental aspects of ion acceleration in the earth's magnetosphere, in *Ion Acceleration in the Magnetosphere and Ionosphere*, vol. 38, edited by T. Chang, pp. 17–36, Washington, D.C.

Chapter 2

Observation of EMIC Waves: Case Studies

This chapter is based in part on results reported by *Usanova et al.* (2008) (Section 2.1) and *Usanova et al.* (2010) (Section 2.2).

2.1 Multipoint Observations of Magnetospheric Compression-related EMIC Pc1 Waves by THEMIS and CARISMA

2.1.1 Introduction

Pc1 (0.2 to 5 Hz) pulsations are continuous geomagnetic field fluctuations believed to be generated by the electromagnetic ion cyclotron (EMIC) instability, free energy often being provided by equatorial hot ions with temperature anisotropy ($T_\perp > T_{||}$) (*Cornwall*, 1965). EMIC wave occurrence has been linked to

variations in the solar wind flow and interplanetary magnetic field (IMF). In particular, there is a class of dayside Pc1 events that show a strong correlation between EMIC power and increases in solar wind pressure (e.g., *Anderson and Hamilton*, 1993; *Arnoldy et al.*, 2005). *Olson and Lee* (1983) suggested that magnetospheric compressions cause an increase in hot proton temperature anisotropy. *Anderson and Hamilton* (1993) confirmed that the probability of observing EMIC waves in space increases during magnetospheric compressions, concluding that plasma in the outer dayside magnetosphere is often close to marginal stability such that EMIC waves can be stimulated by even modest compressions. *Anderson et al.* (1992) suggested that the EMIC growth rate, which is inversely proportional to the Alfvèn velocity ($V_A = B_0/\sqrt{\mu_0 \rho_0}$), peaks at two locations: at high L-shells where the geomagnetic field is relatively weak, and just inside the plasmapause where the ambient plasma density is high. Steep plasmapause density gradients may also provide special propagation conditions that cause local enhancements in growth rates, so that waves can grow significantly even outside the plasmapause, despite the density drop (*Horne and Thorne*, 1993).

Engebretson et al. (2002) observed spatially localized EMIC waves, where continuous wave emissions were seen on the ground for extended periods of time. In space, the waves were observed on the Polar satellite for only a few minutes occurring only in radially narrow regions outside the plasmapause from $L = 5 - 11$. *Engebretson et al.* (2002) suggested that plasma sheet protons convecting sunward from the nightside magnetosphere were responsible for the EMIC wave generation. Inside the plasmapause, Pc1 activity associated with high solar wind density is more unusual. *Zolotukhina et al.* (2007) reported observations of Pc1-2 waves at low- and high-latitude ground stations during storm recovery

phase, suggesting that EMIC activity can be modulated by fast magnetosonic waves launched by the solar wind impacting the magnetopause. We present co-ordinated ground-satellite observations of compression-related, dayside, structured (*Mursula et al.*, 1997) EMIC Pc1 waves from 29th June 2007. The EMIC waves occur coincidentally with a strong solar wind density enhancement following several days of sustained quiet geomagnetic conditions ($Kp < 3$, $Dst > -10$ nT). On the ground, structured EMIC wave activity with a wavepacket repetition period of ~ 3 minutes was observed for several hours simultaneously with the enhancement in solar wind density. In space, the EMIC waves were observed coherently by three THEMIS spacecraft (D, then C, and then E) for a period of 35 minutes as they consecutively crossed the same region of space in a string-of-pearls configuration. Multipoint space-ground observations enabled us to determine the location of the waves in the magnetosphere and conclude that the EMIC wave activity was spatially localized, and confined to a region of low spacecraft potential interpreted here as just inside the plasmapause.

2.1.2 Observations and Data

The orbits of the five Time History of Events and Macroscale Interactions during Substorms (THEMIS, see *Sibeck and Angelopoulos*, 2008) spacecraft lined up in a string-of-pearls with apogee at 15.4 R$_e$ and an orbital period of 36 hours during the initial phase of the mission from launch on February 17 until September 2007. We use data from the THEMIS fluxgate magnetometer (FGM, see *Auster et al.*, 2008) and electric field investigation (EFI, see *Bonnell et al.*, 2008) instruments. The Canadian Array for Real-time Investigations of Magnetic Activity (CARISMA; www.carisma.ca) is the continuation and expansion of the CANO-

PUS magnetometer array. CARISMA has an upgraded cadence (8 samples/s), is expanded through the deployment of new stations, and uses new GPS-timed data loggers and a new data transmission system. The sites used for this study and details of the orbits of THEMIS C, D, and E from 14:00 UT to 16:00 UT are shown in Figure 2.1.

At around 14:00 UT the onset of a significant solar wind density enhancement ($n = 35\,\mathrm{cm}^{-3}$), embedded in a slow solar wind ($V = 350\,\mathrm{km/s}$), arrived at the subsolar magnetopause. This triggered a strong magnetospheric compression that lasted ~ 4.5 hours. At around 18:00 UT the density dropped back to 10 cm^{-3}, and the solar wind speed increased to around 500 km/s. The amplitude of IMF Bz during the event was $0 - 4\,\mathrm{nT}$, and the direction remained positive. IMF By was negative (with minimum amplitude being $-2\,\mathrm{nT}$) from 14:00 to 15:30 UT. Between 15:30 – 18:00 UT, By exhibited two short-term negative excursions, remaining predominately positive ($< 5\,\mathrm{nT}$). The top panel of Figure 2.2 shows the OMNI (*King and Papitashvili*, 2004) solar wind dynamic pressure time-shifted to the subsolar magnetopause, as well as the magnetic field magnitude observed by the geosynchronous GOES 12 satellite ($10.24°$ magnetic latitude, $356.90°$ magnetic longitude). During the solar wind density enhancement GOES 12 was on the dayside between 08:43 – 13:50 MLT, the magnetic field strength increased by ~ 35 nT. Coincidently with the compression, and lasting throughout its duration, the ground magnetometers saw clear and long lasting structured EMIC emissions below 0.7 Hz.

In the course of the day, several CARISMA magnetometers registered structured Pc1 activity in the frequency range from 0.3 to 0.7 Hz. Figure 2.2 (b - g) shows the Fourier spectrograms of the Y-component (geographic east-west) of
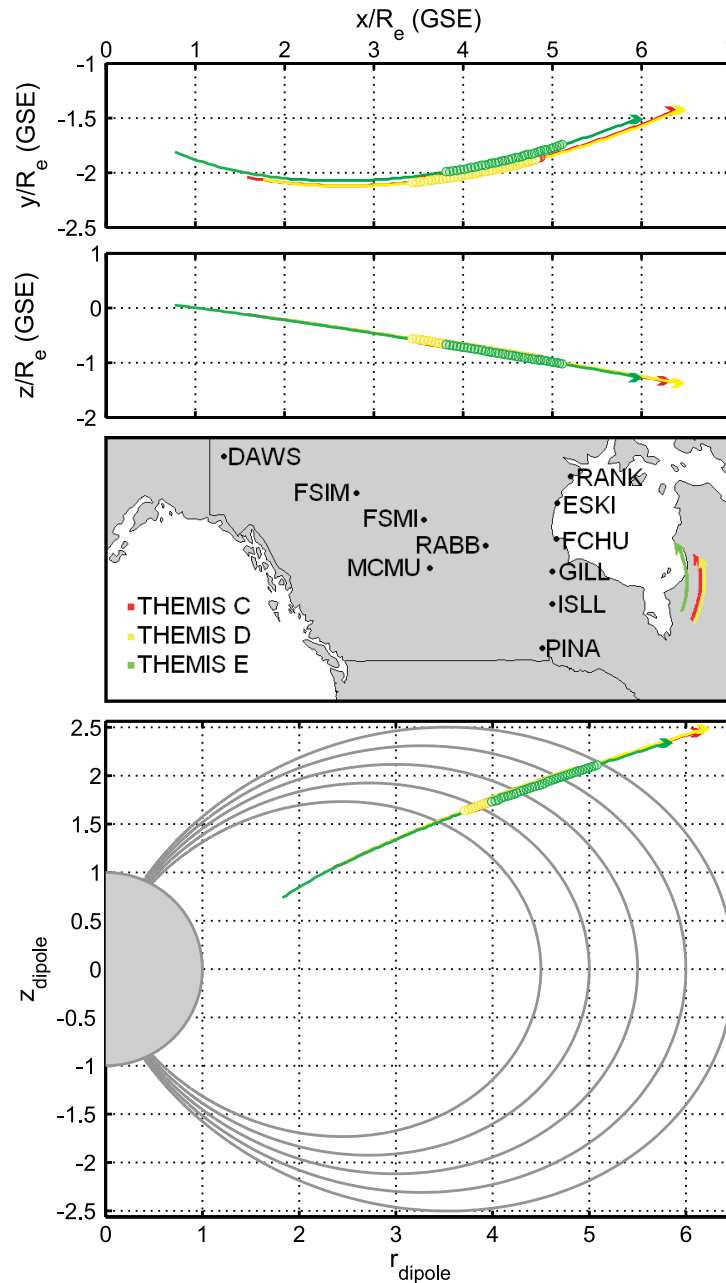
Figure 2.1: GSE orbit plot of the trajectories of THEMIS C, D, E (top two panels) between 14:00 – 16:00 UT; map showing the locations of CARISMA sites and magnetic footprints of THEMIS satellites during the EMIC wave event, starting at 14:35 UT, 14:40 UT and 15:00 UT, respectively (third panel); and GM outbound orbit plot of THEMIS C, D, E superposed over dipole field lines between 14:00 – 16:00 UT. The EMIC wave event was observed by THEMIS at $\sim 23°$ magnetic latitude. Thick lines show the locations where each spacecraft observed EMIC waves (THEMIS C and D were so close that their trajectories practically coincide in the figure).
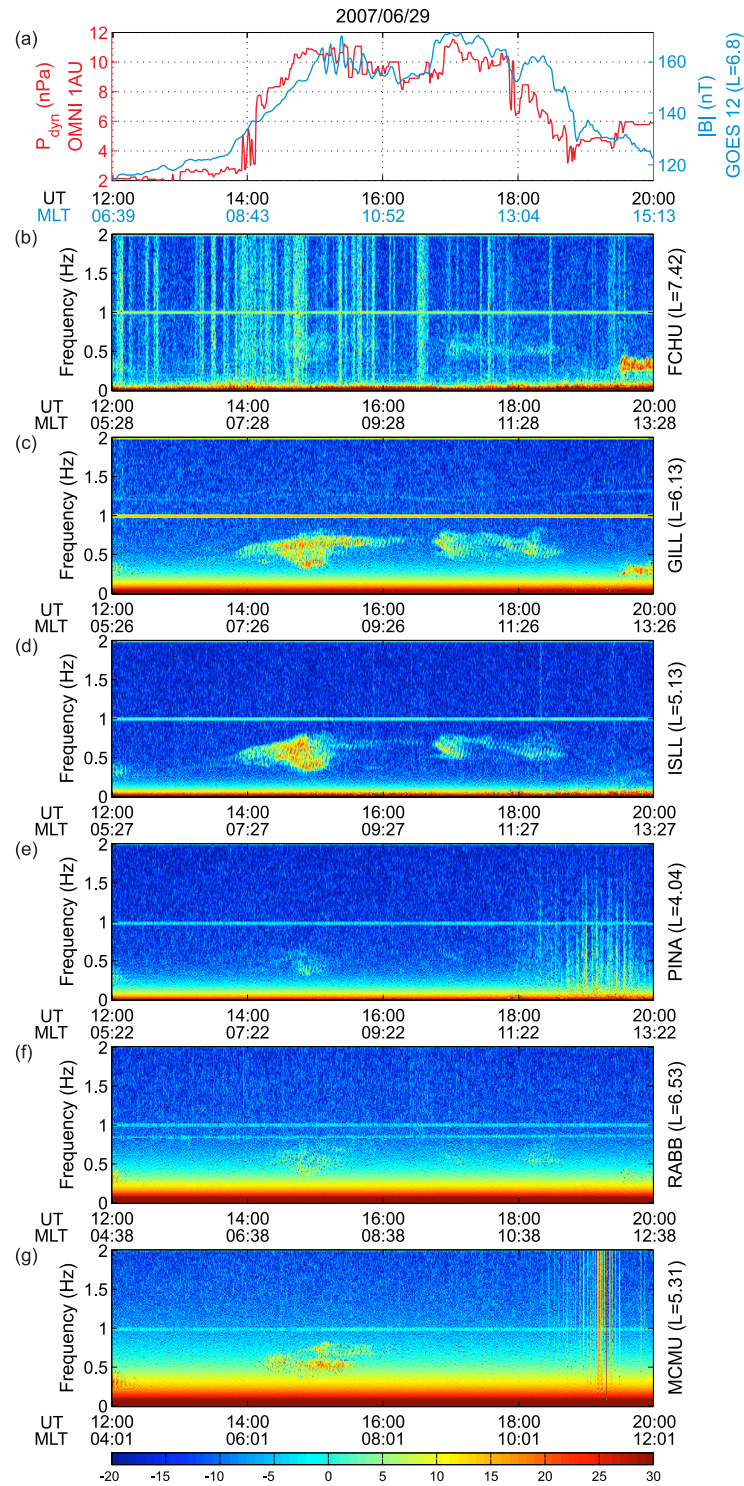
Figure 2.2: (a) Dynamic solar pressure at 1AU (red line) and the magnitude of the magnetic field observed at GOES 12 (blue line), from 12:00 – 20:00 UT; (b) – (g) Fourier spectrograms of the Y-component (geographic east-west) of magnetic field from selected CARISMA stations (see text).

magnetic field at Fort Churchill (FCHU; $L = 7.42$), Gillam (GILL; $L = 6.13$), Island Lake (ISLL; $L = 5.13$), Pinawa (PINA; $L = 4.04$), Rabbit Lake (RABB; $L = 6.53$), and Fort McMurray (MCMU; $L = 5.31$) from 12:00 to 20:00 UT. Similar waves are also seen in the X-component (geographic north-south). The appearance of structured EMIC emissions by the magnetometers along the $\sim 330°$ magnetic meridian (also known as the Churchill line; PINA, ISLL, GILL, and FCHU) matches perfectly the beginning of the period of enhanced solar wind density and the associated magnetospheric compression. The most intense structured Pc1 pulsations appear to coincide with peak solar wind densities.

The EMIC wave event discussed here also shows a longitudinal dependence in Pc1 power. The EMIC intensity associated with the early density enhancement ($\sim$14:00 − 16:00 UT) was seen across both the western and Churchill meridian CARISMA sites, while the wave activity from $\sim$17:00 − 18:00 UT was observed only at the Churchill meridian. The strongest enhancement in EMIC wave power between 14:00 − 16:00 UT was observed at ISLL ($L = 5.13$), MCMU ($L = 5.31$) and GILL ($L = 6.13$), implying that the waves originated from the vicinity of $L = 5 − 6$, before being ducted in the Earth-ionosphere waveguide (*Fraser*, 1976). After 19:00 UT, another structured EMIC emission appears (Figure 2.2 (b - c)), power being confined to higher L and at lower frequencies. These lower frequencies are consistent with lower expected ion gyrofrequencies for a higher L equatorial source. A similar effect was observed by *Zolotukhina et al.* (2007) during a storm recovery phase, and was attributed in their case to a magnetospheric relaxation.

Figure 2.3a shows the spectrogram and time-series of the Y-component (geographic east-west) of magnetic field observed at Gillam. Fourier spectrograms
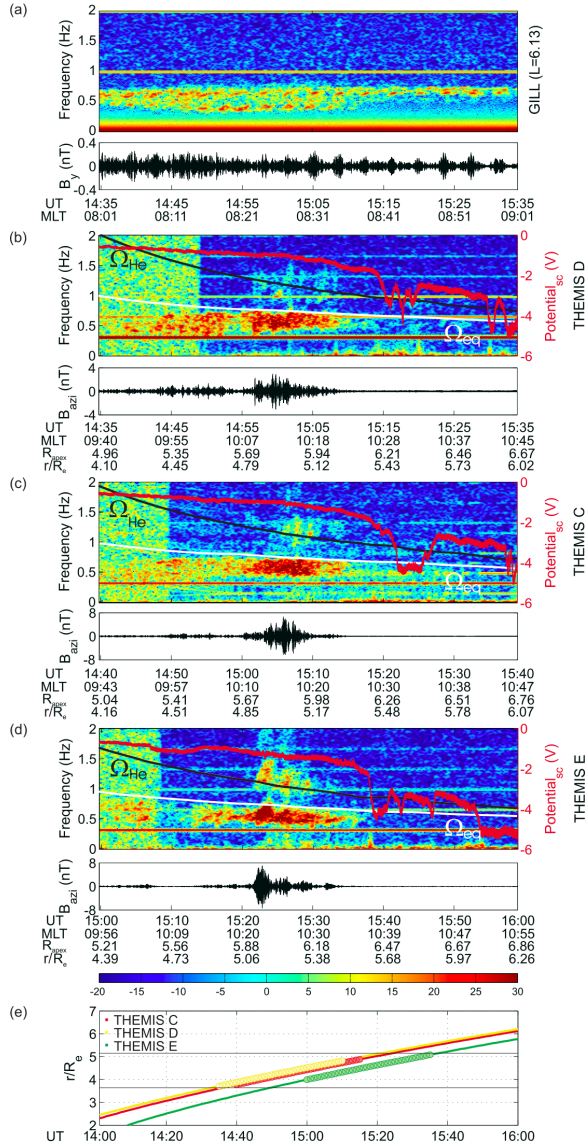
Figure 2.3: (a) Fourier spectrogram and time-series of the Y-component of magnetic field at Gillam; (b) - (d) Fourier spectrograms and waveforms of the azimuthal magnetic field component in FAC at THEMIS D, C, and E, respectively (the change in background color from green to blue is due to the range change of the FGM); over-plotted are the spin-plane spacecraft potential (red line), the local (black line) and the equatorial (white line) helium gyrofrequency. The apexes of the geomagnetic field lines were obtained by tracing field lines from THEMIS to the minimum $|B|$ using the T96 model. (e) geocentric radial distance of THEMIS C, D and E as a function of UT. Thick lines show the intervals where each spacecraft sees EMIC waves.

of the perpendicular (azimuthal) FGM field in field-aligned coordinates from THEMIS D, C and E are shown in Figure 2.3 (b - d), each THEMIS spectrogram starting at a later time at 14:35 UT, 14:40 UT, and then 15:00 UT, respectively. The EMIC spectrograms show significant similarity from spacecraft to space-craft, even though these three satellites traverse the same L-shells at progres-sively later times. Since the EMIC instability is thought to be generated in the equatorial region, it is important to consider how the wave frequency compares to the equatorial ion gyrofrequencies. In order to obtain an equatorial gyrofre-quency estimate, the local gyrofrequency was mapped along the field line to the region of minimum B-field with the T96 model and increased by 27.5 nT, this being the difference between the T96 model and the magnetic field magnitude measured on GOES 12. Each spectrum in Figure 2.3 (b - d) shows EMIC power in two distinct frequency bands, separated by a slot region above the estimated equatorial (white line) and below the observed local (black line) helium gyrofre-quency. This is believed to indicate the presence of thermal helium in the region of wave excitation (*Fraser*, 1985).

The red lines in Figure 2.3 (b - d) show the EFI spacecraft potential, which can represent a proxy for the ambient electron density, at least in low-density re-gions (*Pedersen et al.*, 2001). More negative values (more positive values) of float-ing potentials correspond to the lower (higher) density of surrounding plasma. The spacecraft potential values range between -0.5 to -5 V. These variations in spacecraft potential indicate variations in plasma density and/or temperature and they are interpreted here as due primarily to density changes. The EMIC waves below the equatorial helium gyrofrequency are seen at slightly higher radial distances by each subsequent THEMIS satellite (D, then C, then E), but

in each case the EMIC waves appear to be bounded on the high-L side by a similar sharp decrease in potential. The EMIC waves appear to be confined within the high-density (more positive floating potential) side of this potential decrease. Waves above the local helium gyrofrequency appear to be less intense and do not show much correlation with the spacecraft potential. *Horne and Thorne* (1994) found that high plasma densities enable significant wave growth in the bandwidth below the helium gyrofrequency and at the same time reduce the wave gain above the helium gyrofrequency.

In comparison with Figure 2.3a, we see that only the lower-frequency band is observed simultaneously on the ground. The lack of higher frequency waves on the ground could be due to reflection at the bi-ion frequency, absorption (*Johnson and Cheng*, 1999), or due to its lower power. Further analysis of the satellite EMIC wave polarization characteristics and Poynting vector is warranted. Figure 2.3 also shows the EMIC waveforms filtered between $0.4 - 0.7$ Hz. The EMIC waves observed on the ground from 14:35 to 15:00 UT (see Figure 2.3a) and on THEMIS C, D represent wave packets which do not show clear structure. The later (between 15:00 – 15:35 UT) Pc1 waves appear to be structured both on the ground and on THEMIS E, both having repetition period of about 3 minutes. The amplitude of the waves differs from spacecraft to spacecraft, being ~ 7 nT on C and E, and ~ 3 nT on D. The observed amplitude of the waves on the ground is much smaller, about 0.3 nT.

In order to relate the observed structured pulsations to a potential plasmapause location, we used the ground-based magnetometers to determine the local field-line resonance frequencies by applying the cross-phase analysis technique (*Waters et al.*, 1996) to the data from pairs of CARISMA magnetometers

along the $\sim 330°$ magnetic meridian. Cross-phase FFT windows were $30 - 50$ minutes long, taken between 15:00 – 16:00 UT. Plasma mass densities were derived from the field-line resonance frequencies assuming a dipole field geometry and radial density distribution along field lines $\sim r^{-3}$ (*Dent et al.*, 2003). The resonance frequency and plasma mass density profiles show that a steep plasmapause was located between $L = 4.53 - 5.60$, identified by the region of positive frequency gradient and steepening density gradient (*Kale et al.*, 2007). Corresponding T96 field lines map to a geocentric apex location between $4.84 - 5.94$ R_e, while the density gradient was encountered by the spacecraft between $6.21 - 6.42$ R_e. The discrepancy between the field line apex plasmapause location estimated from the ground and satellite observations could be caused by quiet time structure of the plasmapause (*Carpenter and Anderson*, 1992) or be due to uncertainties in magnetic field line mapping. The regions where each of the THEMIS satellites saw EMIC waves below the equatorial helium gyrofrequency are shown in Figure 2.3 (e). The separation between the spacecraft remained ~ 0.1 R_e between THEMIS D and C, and ~ 0.5 R_e between C and E. EMIC waves were coherently recorded by the THEMIS D, C and E in localized emissions with a width of ~ 1.3 R_e. The region supporting the Pc1 pulsations moved outwards slightly from the time of the crossing of THEMIS C and E, however the waves spanned the range of T96 geocentric apex location of 4.96 to 6.21 R_e which is consistent with the ground-based observations.

2.1.3 Conclusions

We have presented simultaneous ground-satellite observations of structured dayside Pc1 emissions related to magnetospheric compressions arising from en-

hanced densities in the solar wind. In space, the EMIC emissions appeared in two frequency bands both below and above the local helium gyrofrequency, with a clear slot region in emissions. Using three THEMIS satellites, we were able to clearly resolve the spatio-temporal ambiguity to show that the EMIC emissions below the equatorial helium gyrofrequency were radially localized to a region $\sim 1.3\,R_e$ wide.

The waves below the equatorial helium gyrofrequency were confined at higher L-shell by a sharp decrease in spacecraft potential indicating their apparent confinement within a region of higher plasma density. The most intense waves on the ground were observed at the same L and the same frequency as those in space; however, only waves in the lower frequency band below the equatorial helium gyrofrequency were observed on the ground. The repetition period of structured Pc waves on the ground and on THEMIS E was also found to be almost the same, which cannot be explained by the bouncing wave packet model (*Jacobs and Watanabe*, 1964). Ground-based cross-phase estimates of the plasmapause location also place the EMIC waves close to the plasmapause region in space which is thought to provide a preferential region for wave growth through convective amplification and gain (*Horne and Thorne*, 1993) and where the structured Pc1 pulsations are typically observed (*Mursula et al.*, 1997). Structure in the boundary layer of the quiet time plasmapause (*Carpenter and Anderson*, 1992) could also explain different wave excitation conditions and hence the different wave amplitudes seen during the sequential pass of each THEMIS satellite.

Usually, compression-related EMIC waves are thought to be preferentially confined to higher-L regions closer to the magnetopause during compressions at quiet times (*Engebretson et al.*, 2002) and only inside or close to the plasma-

pause during the recovery phase of storms, following ion injections. Our observations suggest solar wind density enhancements and magnetospheric compressions may also be an important source for lower-L radially confined EMIC emissions close to the plasmapause, perhaps due to enhanced temperature anisotropy which develops along dayside ion drift trajectories in a compressed magnetosphere. Given the potential role for EMIC waves in MeV electron loss in the radiation belts (*Summers and Thorne*, 2003), and the correlation between the plasmapause and the inner edge of the outer zone electron radiation belt (*Li et al.*, 2006), these observations may have wider importance for inner magnetosphere energetic particle dynamics.

2.2 Conjugate Ground and Multi-satellite Observations of Compression-related EMIC Pc 1 Waves and Associated Proton Precipitation

2.2.1 Introduction

Electromagnetic ion cyclotron (EMIC) waves are transverse plasma waves generated in the equatorial magnetosphere by energetic protons with temperature anisotropy ($T_\perp > T_\parallel$) and registered on the ground as Pc1-2 or IPDP (Intervals of Pulsations with Diminishing Periods) magnetic pulsations (*Hayakawa et al.*, 1992) in the frequency range between $0.1 - 5$ Hz. In the source region the waves are expected to be left-hand polarized, corresponding to the sense of ion rotation around the magnetic field. Early theoretical studies have shown that the

EMIC wave growth leads to the isotropization of the initially unstable proton distribution and consequent pitch-angle scattering and loss of particles into the ionosphere (*Cornwall*, 1965). This theory was supported by conjugate observations of localized precipitation of energetic protons (LPEP) at the ESRO satellite and IPDP pulsations conjugate to the satellite on the ground for the first time reported by *Soraas et al.* (1980). Further connection between LPEP and EMIC waves has been studied using low-Earth orbit polar NOAA satellites (*Yahnin and Yahnina*, 2007). Today, EMIC waves are considered as one of the important mechanisms affecting ring current dynamics and their effects are included in global ring current numerical simulation models (*Jordanova et al.*, 1997).

Recent theoretical studies (*Summers and Thorne*, 2003) have shown that in the inner magnetosphere a resonant interaction with EMIC waves may also be important for MeV electron loss from the radiation belts, especially in regions of high plasma density and low magnetic field, e.g., outer regions of the quiet-time plasmasphere. So far, there has been no direct experimental evidence supporting this hypothesis. However, *Sandanger et al.* (2007) reported simultaneous observations of collocated LPEP and relativistic electron precipitation in space and suggested that the latter might be the result of scattering of the electrons into the loss cone by EMIC waves even though they did not report any direct evidence of the presence of EMIC waves. Hence, EMIC waves are believed to be important not only for ring current, but also for radiation belt dynamics.

In order to incorporate the EMIC-related loss processes into global magnetospheric models, one needs to know the solar wind and magnetospheric conditions favorable for EMIC wave growth as well as the localization of the waves in the magnetosphere. Early studies have identified the plasmapause as a pre-

ferred region for EMIC wave generation, since the increasing number of cold ions leads to the drastic enhancement in the convective EMIC wave growth (which is inversely proportional to the Alfvén speed, V_A) (*Gendrin*, 1975). For example, EMIC waves were found to be preferentially excited along the duskside plasmapause during periods of enhanced magnetospheric convection (*Summers et al.*, 1998). The convection electric field may lead to the overall intensification of the ring current and also to the formation of anisotropic particle distributions which may, furthermore, aid wave growth.

Further studies revealed other processes in the magnetosphere that lead to enhanced energetic ion temperature anisotropies. It was concluded that the waves could be also generated in the subsolar equatorial magnetosphere close to the magnetopause during magnetospheric compressions (*Olson and Lee*, 1983; *Anderson and Hamilton*, 1993; *Denton et al.*, 2002) and in the cusp regions with peak occurrence near local noon and under different levels of geomagnetic activity (*Menk et al.*, 1992). Some observations of Pc1-2 pulsations in the cusp region have also been explained by injections of anisotropic ion populations generated in the equatorial magnetosphere and drifting westward (*Hansen et al.*, 1992). Recently, *Usanova et al.* (2008) reported observations of EMIC waves just inside the plasmapause (at $L \sim 6$) in the morning magnetic local time (MLT) sector during quiet geomagnetic conditions associated with intense magnetospheric compression due to enhanced solar wind dynamic pressure. The authors concluded that magnetospheric compressions might be an important source of radially localized EMIC waves in the dayside plasmasphere and suggested that this mechanism of EMIC wave generation might have wider importance for inner magnetosphere energetic particle dynamics.

One of the mysteries of EMIC waves is their repetitive wave packet structure which is often (but not always) observed on the ground. In spectrograms, they usually appear as distinct wave packets of rising frequency, regularly repeated with period of ten to hundreds of seconds (*Mursula et al.*, 1997) and therefore are classified as structured Pc1 pulsations or pearls. Pearls are the most common type of Pc1 pulsations observed at mid- and low-latitude magnetometer stations. Traditionally, structured Pc1's have been explained by a bouncing wave packet model (*Jacobs and Watanabe*, 1964). In this model, a wave packet excited in the equatorial plane travels along the magnetic field line, is reflected between conjugate hemispheres, and energy loss from incomplete ionospheric reflection is compensated by further wave growth as the wave packet recrosses the equator.

However, there are a number of observations that do not agree with this theory. For example, the wave packet repetition period on the ground was found to be shorter than the realistic travel time of the wave packet between the hemispheres (*Mursula et al.*, 2001), the repetition period was observed to be the same on the ground and at off-equatorial satellites (*Mursula et al.*, 1999; *Usanova et al.*, 2008), and the EMIC wave reflection coefficient from the ionosphere was estimated to be negligible (*Denton et al.*, 1992). EMIC wave Poynting flux measurements (*Fraser et al.*, 1996; *Loto'aniu et al.*, 2005) have also shown that the wave energy appears to be propagating away from the equator. An alternative theory suggested that EMIC repetitive structure might instead be due to modulation of EMIC wave growth and consequently, wave power in the source region by the lower-frequency (Pc3-5) ULF waves (*Fraser et al.*, 1992; *Rasinkangas and Mursula*, 1998; *Loto'aniu et al.*, 2009).

This paper is organized as follows. First, we discuss the ground-based and satellite instrumentation used for this study. Then we present observations of EMIC waves registered by ground-based and Cluster magnetometers during the interval of enhanced solar wind dynamic pressure. Further we discuss the NOAA satellite observations of LPEP, and consider the Cluster observations in the EMIC source region and show that they are inconsistent with the hypothesis of ULF modulation. A conclusion section ends our paper.

2.2.2   Instrumentation

Magnetometer arrays. The Canadian Array for Real-time Investigations of Magnetic Activity (CARISMA; www.carisma.ca) is the continuation and expansion of the former CANOPUS magnetometer array deployed and operated by the University of Alberta (*Mann et al.*, 2008). CARISMA has an upgraded cadence (8 samples/s), is expanded through the deployment of new stations, and uses new GPS-timed data loggers and a new data transmission system. At the moment, the array consists of both fluxgate and searchcoil magnetometers. In 2005, only fluxgate magnetometers operated. For this study we hence use data only from the CARISMA fluxgate magnetometers with measurement resolution of 0.025 nT. The Solar-Terrestrial Environment Program (STEP) Polar Network http://www-space.eps.s.u-tokyo.ac.jp/~hayashi is an array of fluxgate and searchcoil magnetometers. The STEP searchcoil magnetometers provide measurements with cadence of 10 samples/s and resolution of ~ 3 pT. We also use ground magnetic field data from the Scandinavian sector. Kiruna (Sweden) magnetometer station (www.irf.se) has a fluxgate magnetometer recording data at 10 samples/sec. The Sodanskylä Geophysical Observatory in Fin-

land (http://www.sgo.fi/Data/Pulsation/pulData.php) also runs an array of searchcoil magnetometers where data are available at 40 samples/sec time resolution. All magnetometer stations used in this work are listed in L-shell order in Table 2.1.

Station name	Instrument type	Frequency (Hz)	Geo latitude	Geo longitude	MLTMN (UT)	L
UZR	SC	10	53.32	107.74	16:57	2.31
LCL	SC	10	51.00	252.90	7:34	3.94
PINA	FG	8	50.20	263.96	6:39	4.11
PKS	SC	10	52.20	252.80	7:36	4.23
ISLL	FG	8	53.86	265.34	6:33	5.23
ROV	SC	40	66.78	25.94	21:10	5.08
SOD	SC	40	67.42	26.39	21:07	5.31
MCMU	FG	8	56.66	248.79	8:00	5.41
KIR	FG	10	67.50	20.25	21:27	5.45
DAWS	FG	8	64.05	220.89	10:27	6.10
RABB	FG	8	58.22	256.32	7:23	6.68
FSIM	FG	8	61.76	238.77	8:58	6.84

Table 2.1: Details of Magnetometer Stations. Abbreviations: SC (searchcoil), FG (fluxgate), MLTMN (magnetic local time midnight).

Cluster. The four Cluster satellites (*Escoubet et al.*, 2001) were launched into elliptical polar orbit with a period of 57 hours, perigee of 4 R_e and apogee of 19.6 R_e. This makes it possible for Cluster to cross the ring current, the radiation belts and the plasmapause on each perigee pass. All Cluster satellites carry identical instrumentation allowing for 3D observations of active processes in the Earths magnetosphere. For this study, we use data from the Cluster fluxgate magnetometers (FGM, see *Balogh et al.*, 2001), electron drift instruments (EDI, see *Paschmann et al.*, 2001), Electric Field and Wave instruments (EFW, see *Gustafsson et al.*, 2001), and Waves of High frequency and Sounder for Probing

of Electron density for Relaxation instruments (WHISPER, see *Décréau*, 2001).
The Cluster FGM provides measurements of the magnetic field in the frequency
range from DC to 10 Hz (32 Hz in burst mode) and measurement resolution of
at least 0.1 nT. The Cluster EDI instrument allows for the measurements of the
electric field once every 0.128 sec (in normal mode) with accuracy of 0.1 mV/m.
EFW is important in this study as it also measures spacecraft floating potentials
which can represent a proxy for the ambient electron densities. WHISPER can
also detect electron densities below 80 e/cc.

NOAA 17 (The National Oceanic and Atmospheric Administration;
http://www.ngdc.noaa.gov/stp/NOAA/noaa_poes.html) is a polar-orbiting satel-
lite. The NOAA 17 orbits are circular, with an altitude between 830 (morning or-
bit) and 870 (afternoon orbit) km, and are sun synchronous. NOAA crosses the
equator northbound around 22 MLT. NOAA 17 carries onboard a Medium En-
ergy Proton and Electron Detector (MEPED) that monitors intensities of charged
particle radiation (*Evans and Greer*, 2000). There are two identical proton tele-
scopes: the $0°$ detector, at high latitudes, monitoring particles in the atmospheric
loss cone and the $90°$ detector, monitoring particles that are mirroring near the
satellite. The detectors have $\pm 15°$ FWHM (Full With Half Maximum) field of
view. The MEPED detector identifies protons within six energy ranges: $30 - 80$
keV, $80 - 250$ keV, $250 - 800$ keV, $800 - 2500$ keV, $2500 - 6900$ keV, and above
6900 keV. For this work, we use data from the first three channels sampled at 0.5
samples/sec.

GOES 10, 12 (The Geostationary Operational Environmental Satellites;
http://www.ngdc.noaa.gov/stp/GOES/goes.html) are positioned at geostation-
ary orbits over the geographic equator and a few degrees off the geomagnetic

equator. GOES 12 (or GOES-East) is located at 75 W geographic longitude, while GOES 10 (or GOES-West) is at 135 W geographic longitude. Both satellites have fluxgate magnetometers installed onboard that can detect magnetic field variations in the frequency range from DC to the 1 Hz Nyquist frequency (*Singer et al.*, 1996).

2.2.3   Observations

In this section we present observations of EMIC waves and solar wind parameters on September 25, 2005.

Geomagnetic Conditions

The EMIC wave event of September 25, 2005 followed two weeks of geomagnetic quiescence. During the day of September 25, the Dst index (Figure 2.4a) had minor variations ranging from -12 to 7 nT. There is an AE enhancement of up to 500 nT (Figure 2.4b) between approximately $11 - 14$ UT associated with negative excursion in the GSM IMF Bz component (Figure 2.4d). After 14 UT the geomagnetic conditions were relatively undisturbed as indicated by the Kp index which remained less than or equal to 1+ until 22 UT (see top of Figure 2.4). Figure 2.4 (c-g) show the IMF By and Bz in GSM coordinates, and the solar wind velocity, density and dynamic pressure, respectively, measured upstream by the ACE/Wind satellites, time-shifted to the Earth's magnetopause, and provided through the OMNI database (*King and Papitashvili*, 2004). The solar wind density remained relatively high, especially between $\sim 7 - 11$ UT (Figure 2.4f) and the solar wind speed gradually increased from 300 to 400 km/s (Figure 2.4e)
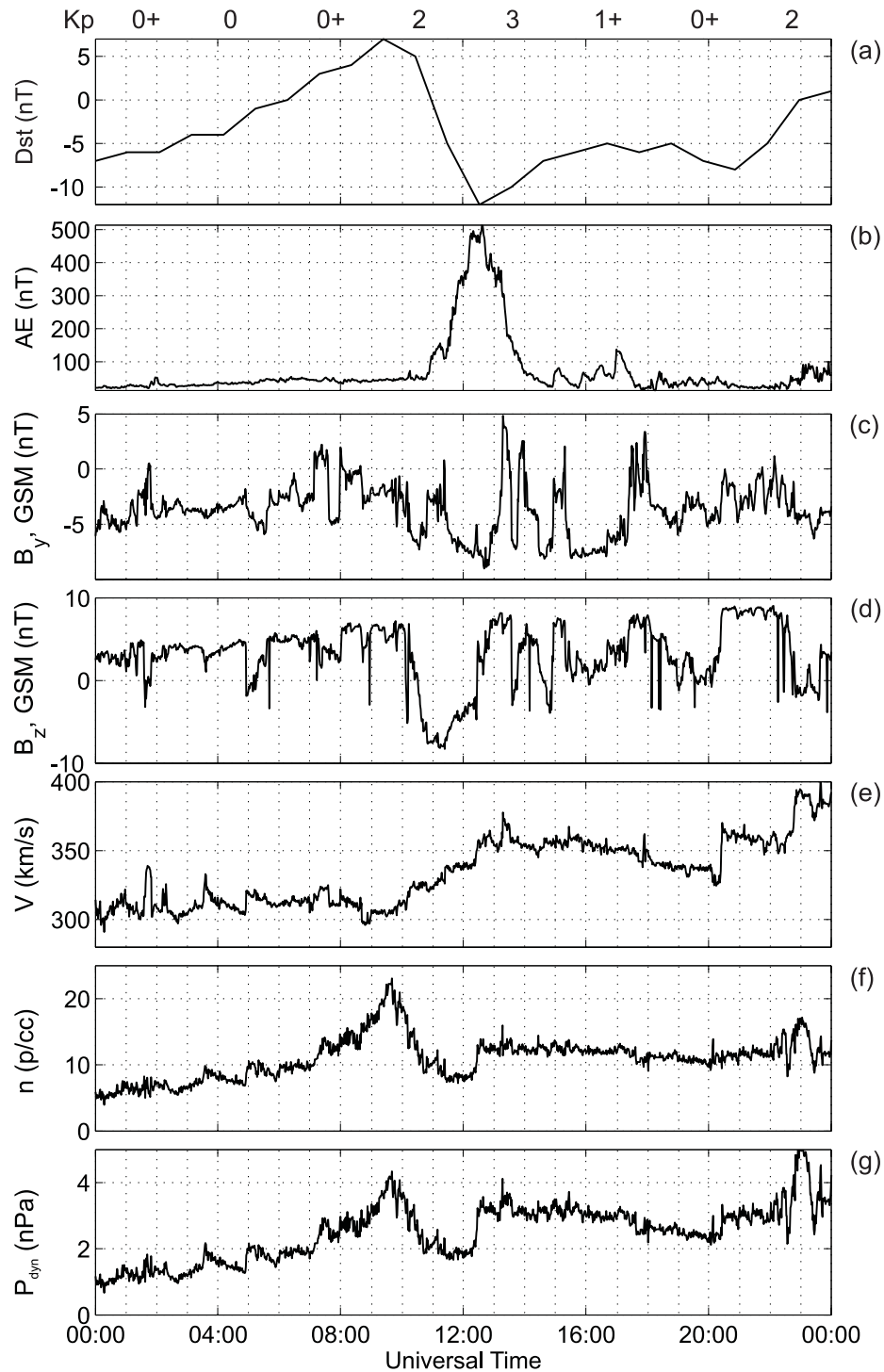
Figure 2.4: Geomagnetic indices and OMNI solar wind parameters on 25 September 2005: (top) Kp index, (a) Dst index, (b) AE index, (c) GSM IMF By, (d) GSM IMF Bz, (e) solar wind velocity, (f) solar wind ion density, (g) solar wind dynamic pressure. All OMNI data are time shifted to the dayside subsolar magnetopause.

so that the resultant dynamic pressure was enhanced between $\sim 7 - 11$ UT as well as after ~ 13 UT.

Conjugate EMIC Wave Observations by Cluster and Ground-based Magnetometers

On September 25, EMIC wave activity was detected throughout the day by multiple ground-based magnetometers in different MLT sectors. In response to the solar wind dynamic pressure enhancement between $7 - 11$ UT (Figure 2.4g replotted in Figure 2.5a), EMIC waves appeared in the Scandinavian sector (morning MLT). Figure 2.5b shows the spectrogram of the X-component (geographic north-south) of the magnetic field measured at the Kiruna magnetometer station (KIR; $L = 5.45$). Consistent with the observations by *Usanova et al.* (2008), the EMIC wave power ceases between $\sim 11{:}00 - 12{:}30$ UT when the solar wind dynamic pressure decreases, and EMIC wave power returns later when the second burst of enhanced solar wind pressure causes EMIC wave power to start growing again. A similar situation where two EMIC wave bursts appear during the strongest solar wind dynamic pressure was also observed by the Sodanskylä observatory magnetometer array (not shown) in the Finnish sector between $\sim 7 - 11$ UT and $\sim 13 - 16$ UT. The most intense EMIC waves were detected by the magnetometers at Rovaniemi (ROV; $L = 5.08$) and Sodanskylä (SOD; $L = 5.31$). The quicklook spectrograms from the Finnish sector are available through the Sodanskylä Geophysical Observatory website (http://www.sgo.fi/Data/Pulsation/pulData.php).

During the second interval of enhanced solar wind dynamic pressure, Canadian magnetometers (shown on map in Figure 2.6) rotated into the morning
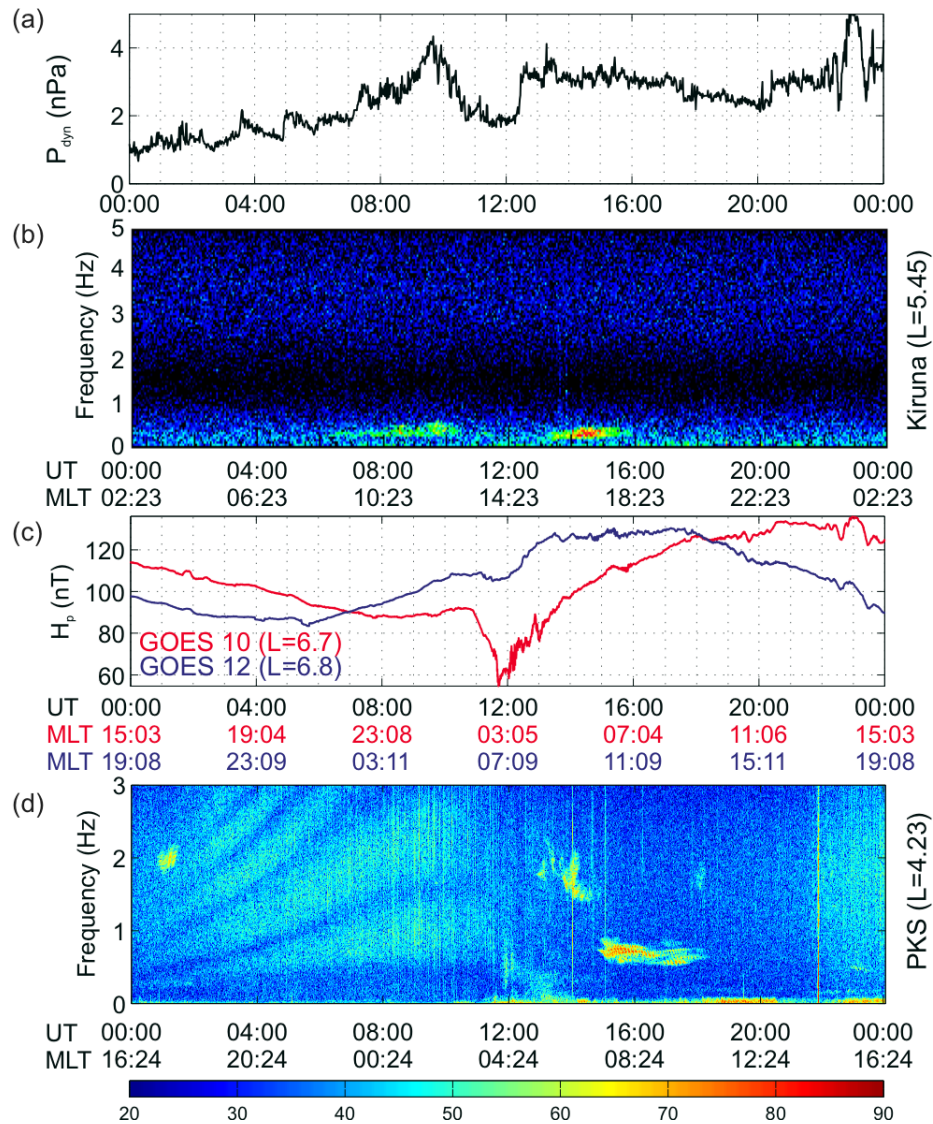
Figure 2.5: (a) Solar wind dynamic pressure, P$_{dyn}$ (also shown in Figure 2.4g); (b) Fourier spectrogram of the X-component of magnetic (geomagnetic North-South) from the Kiruna station; (c) magnitude of the H_p-component of the magnetic field observed at GOES 10 (red line) and GOES 12 (blue line); (d) Fourier spectrogram of the D-component (geomagnetic East-West) of the magnetic field from the Parksite station on September 25, 2005. The spectrogram also shows signatures of the ionospheric Alfvén resonator between $0 - 11$ UT (*Parent et al.*, 2007).
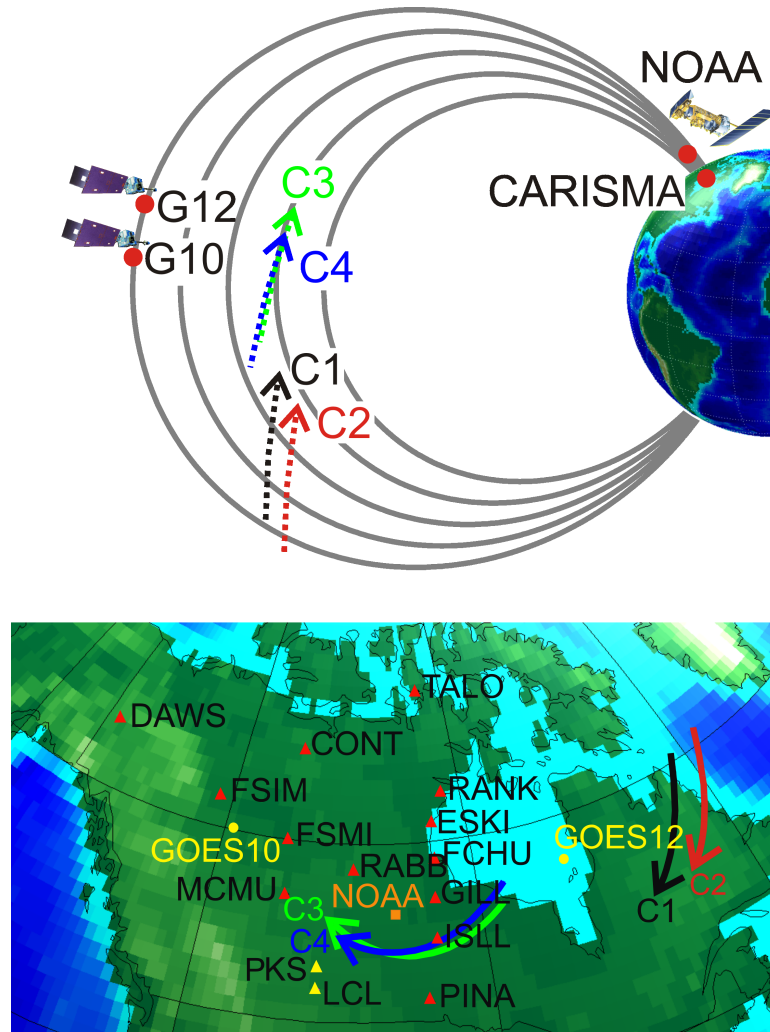
Figure 2.6: (top) Schematic showing the observation points: GOES satellites at the geosynchronous orbit (G10 and G12), Cluster 3, 4 in the equatorial plane at 17:30 – 18:30 UT, Cluster 1, 2 at ~ 20 degrees off the equator between 14:30 – 15:00 UT, NOAA 17 above Canada at 17:51 UT moving northward, CARISMA on the ground. (bottom) Locations of the selected CARISMA and STEP magnetometer stations: Lucky Lake, (LCL), Parksite (PKS), Island Lake (ISLL), Fort McMurray (MCMU), Dawson (DAWS), Rabbit Lake (RABB), Fort Simpson (FSIM), Pinawa (PINA), Gillam (GILL), Fort Churchill (FCHU), Eskimo Point (ESKI), Rankin Inlet (RANK), Taloyoak (TALO), Contwoyto (CONT) and the magnetic footprints of Cluster, GOES and NOAA 17 mapped to the ground with the T96 model (Cluster 1,2 between 14:30 – 15:00 UT; Cluster 3, 4 between 17:30 – 18:30 UT; NOAA 17 at 17:51 UT). The red and yellow triangles indicate sites with fluxgate and searchcoil magnetometers, respectively.
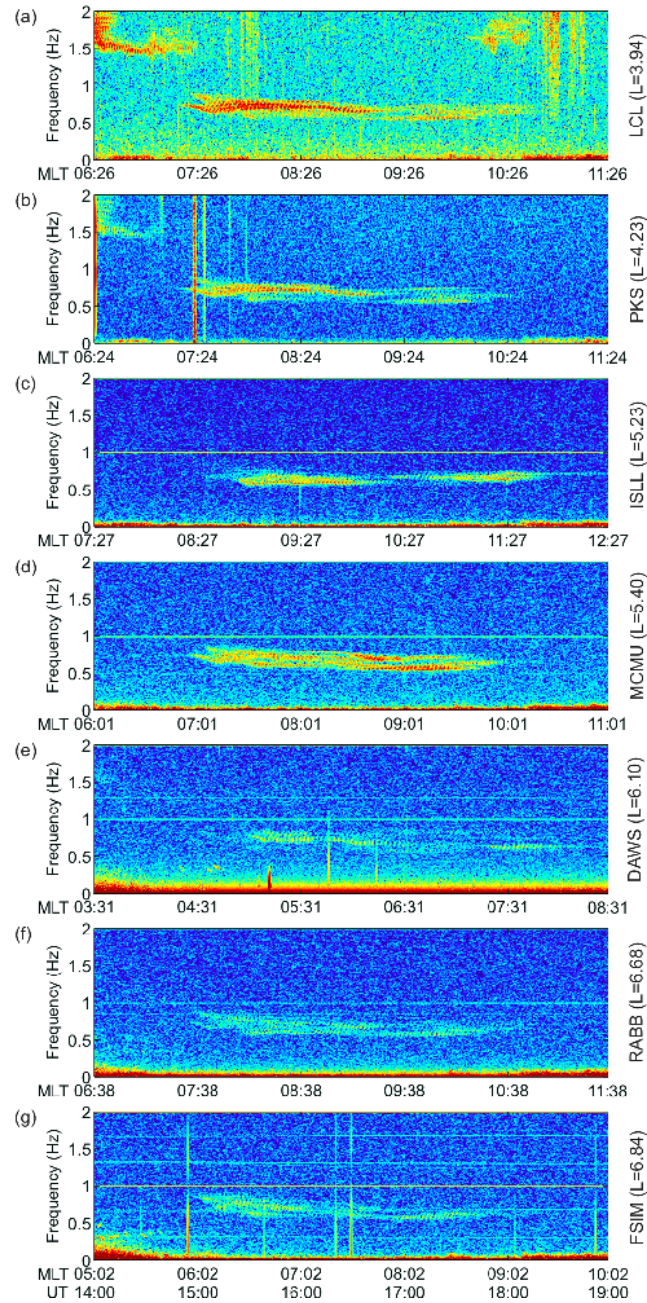
Figure 2.7: Fourier spectrograms of the D-component (geomagnetic East-West) of magnetic field from selected CARISMA and STEP stations (see text) between 14 – 19 UT. Note that the upper two panels show data from search-coil magnetometers. As search coil magnetometers are more sensitive to magnetic field fluctuations in this frequency range, the relative wave spectral magnitude between the sets of data from the two types of instrument should not be compared.

MLT sector. At around 13 UT IPDP pulsations, probably a remnant of the preceding AE enhancement or a response to the enhanced dynamic pressure, appeared. Further, starting at ~ 15 UT and lasting for 3.5 hours, structured Pc1 activity in the frequency range from 0.65 to 0.75 Hz (close to the frequency observed by Scandinavian magnetometers) was detected (Figure 2.5d). For this interval, we also have magnetic field data from the GOES 10 and 12 satellites located over Canada. The structured Pc 1 pulsations appeared on the ground when associated magnetospheric compression, observed as an increase in the magnitude of the magnetic field at GOES 12, reached its maximum as seen in the H_p (parallel to the Earth's spin axis and sensor most closely aligned with the magnetic field) magnetic field component (blue line in Figure 2.5c). Later, an enhanced H_p was also seen at GOES 10 as it entered the morning MLT sector (red line in Figure 2.5c). Overall, the magnitude of the H_p component recorded by the GOES satellites on the dayside was by 24 nT larger than during the days of more usual solar wind dynamic pressure.

Structured Pc 1 pulsations were also registered by other Canadian magnetometer stations at Lucky Lake (LCL; $L = 3.94$), Parksite (PKS; $L = 4.23$), Island Lake (ISLL; $L = 5.23$), Fort McMurray (MCMU; L=5.41), Dawson (DAWS; $L = 6.10$), Rabbit Lake (RABB; $L = 6.68$), and Fort Simpson (FSIM; $L = 6.84$) shown on the map in Figure 2.6. Figure 2.7 (a - g) shows respectively the Fourier spectrograms of the D-component (geomagnetic East-West) of magnetic field at Lucky Lake, Parksite, Island Lake, Fort McMurray, Dawson, Rabbit Lake, and Fort Simpson from 14:00 to 19:00 UT. Similar EMIC wave packet structures are also seen in the H-component (geomagnetic North-South). Due to the propagation effect in the Earth-Ionosphere waveguide, the EMIC waves are likely to

be seen far from the magnetic footprint of the source region. However, EMIC wave power is expected to be attenuated over the propagation path. Comparing the wave intensities at multiple magnetometer stations, it is therefore possible to establish the probable location of the ionospheric projection of the source region as corresponding to the region of maximum EMIC wave power seen on the ground. The most intense waves observed by the fluxgate magnetometers shown in Figure 2.6 (bottom panel) were localized around $L \sim 5$ as indicated by the spectrograms in Figure 2.7c-d. The fluxgate magnetometers located at higher L-shells observed less intense waves (see Figure 2.7e-g) and the one located at Pinawa (PINA; $L = 4.11$) did not register any EMIC activity at all (not shown). However, the two STEP searchcoil magnetometers at Parksite (PKS; $L = 4.23$) and Lucky Lake (LCL; $L = 3.94$) did register Pc 1 pulsations. This can be explained by the fact that the search coil magnetometers are more sensitive to the field variations in this frequency range than the fluxgate magnetometers. It should be also noted that during the period of AE enhancement ($11 - 14$ UT) EMIC waves were registered by the Uzury magnetometer (UZR; $L = 2.31$) between $\sim 19 - 21$ MLT. The intensity of the pulsations at Uzury was relatively low most probably because the footprint of the source region was located at a higher L-shell. These duskside observations point to a different (rather than enhanced P_{dyn}) source mechanism for EMIC wave generation at Uzury consistent with the more traditional hypothesis that EMIC waves are excited in the duskside magnetosphere due to enhanced magnetospheric convection and/or ion injection.

During the September 25, the four Cluster spacecraft were located in the dayside magnetosphere and three of them detected EMIC waves. Figure 2.6
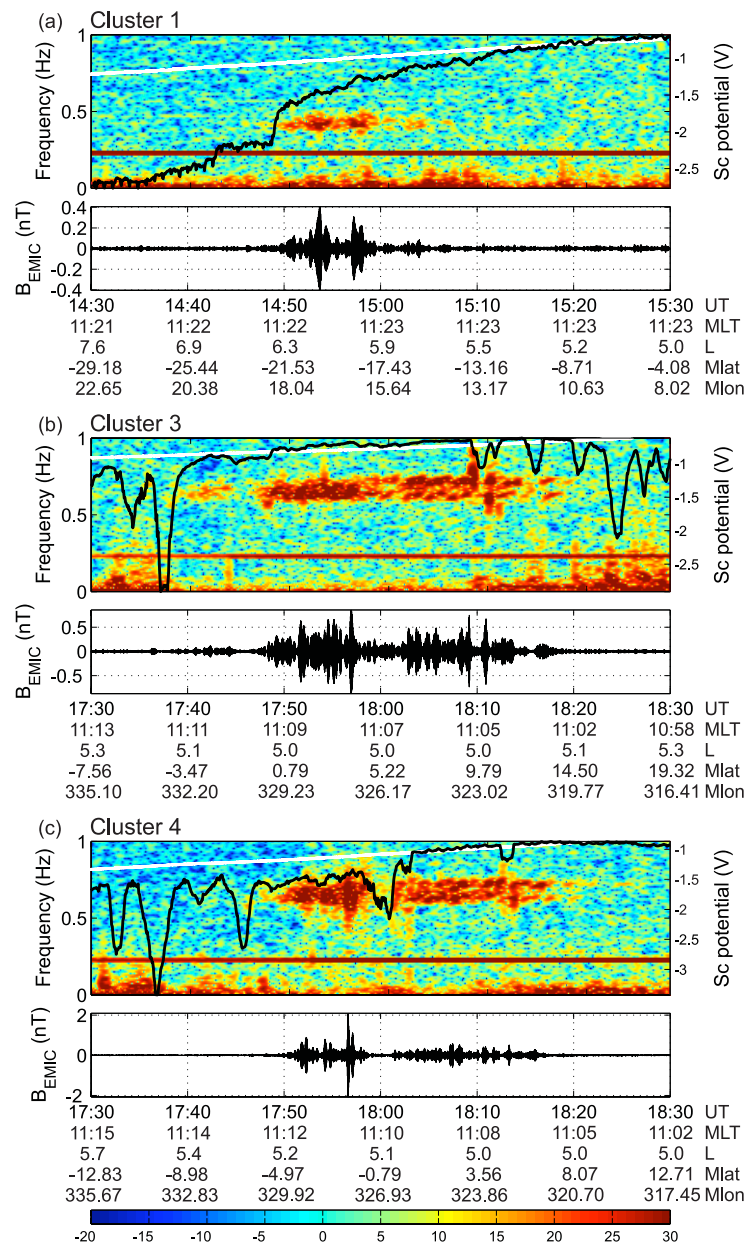
Figure 2.8: Fourier spectrogram (top panel) and waveforms (bottom panel) of the perpendicular (azimuthal) magnetic field component in field-aligned coordinates for one-hour windows at Cluster 1, 3, and 4 in panels (a), (b), and (c), respectively. Over-plotted in each panel are the spacecraft potential (black line) and the local helium gyrofrequency (white line). See text for details. The bright red line in each spectrogram corresponds to the Cluster spin period (4 seconds).

shows the locations of the Cluster satellites (denoted by C1, C2, C3, and C4) in the magnetosphere along with their magnetic footprints mapped to the ground with the T96 model (*Tsyganenko*, 1996). First, between 14:50 – 15:00 UT EMIC activity at $0.3 - 0.5$ Hz appeared at Cluster 1 localized from $L = 5.7$ to $L = 6.4$ at approximately $20°$ below the magnetic equator (Figure 2.8a) in a high density region (based on the spacecraft potential measurements) just inside the plasma-pause, consistent with the observations by *Usanova et al.* (2008). It should be also noted that the magnetic footprints of Cluster 1 were located at more than 3 hours to the east from the ground magnetometer stations in the Canadian sec-tor (black arrow on the map in Figure 2.6), and the waves observed at Cluster 1 between $\sim$ 14:50 – 15:05 UT were not seen on the ground by the magnetometers used in this work. Later, EMIC waves were detected by Cluster 3 and 4 in the equatorial plane during their perigee passes between $\sim$ 17:45 – 18:15 UT. At this time, Cluster 3 and 4 were in a very good magnetic conjunction with the Island Lake magnetometer station (footprints of the trajectories are shown by the blue and green arrows on the map in Figure 2.6) and observed EMIC waves in the frequency band between $0.65 - 0.75$ Hz matching the one on the ground.

Figure 2.8 shows the spectrograms and waveforms of the perpendicular (az-imuthal) magnetic field component. The magnetic field data has been trans-formed from the GSM into local field-aligned coordinates using the procedure described in *Rae et al.* (2005). In this coordinate system, the azimuthal direction is perpendicular to both the direction of the background magnetic field and the radial direction, which lies in the plane containing the vector from the center of the Earth to the satellite.

In a multicomponent magnetospheric plasma, there are forbidden band gaps

for EMIC wave generation and propagation, generally, around heavy ion gy-
rofrequencies that split the wave spectrum into multiple branches. It can be
seen that the observed EMIC wave emissions lie on the helium branch (with
frequency below the local helium gyrofrequency, shown in each spectrogram by
the white line). Typically, there is a gap between a branch cutoff frequency and
the corresponding heavy ion gyrofrequency. The width of this gap depends on
the heavy ion concentration, temperature and anisotropy (*Gendrin et al.*, 1984).
The polarization of the waves at Cluster 1, Cluster 3 and 4 is left-handed (not
shown here), consistent with the direction of ion rotation around the magnetic
field and with expectations from the theory of EMIC wave generation if Cluster
is observing the EMIC waves close to the source region. The black lines show
the EFW spacecraft floating potentials - indicators of the background electron
density, (*Pedersen et al.*, 2001). More negative values (more positive values) of
floating potentials correspond to a lower (higher) electron density of the sur-
rounding plasma. We have estimated the related electron densities using the
WHISPER instrument data. The interesting feature is that the EMIC waves ap-
peared to be confined within the region of high electron density (> 70 e/cc)
and follow nicely the density structures observed by Cluster 3, 4 on their in-
and outbound passes through the plasmapause. Clearly, the cessation of EMIC
wave activity seen on Cluster 3 at 18:10 UT and on Cluster 4 at 18:00 UT is asso-
ciated with the density drops as monitored by spacecraft potential. Appearance
of the EMIC waves in regions of higher plasma densities is consistent with the
EMIC wave theory predictions, as a larger convective wave growth is expected
here (*Kozyra et al.*, 1984).

EMIC-Related LPEP
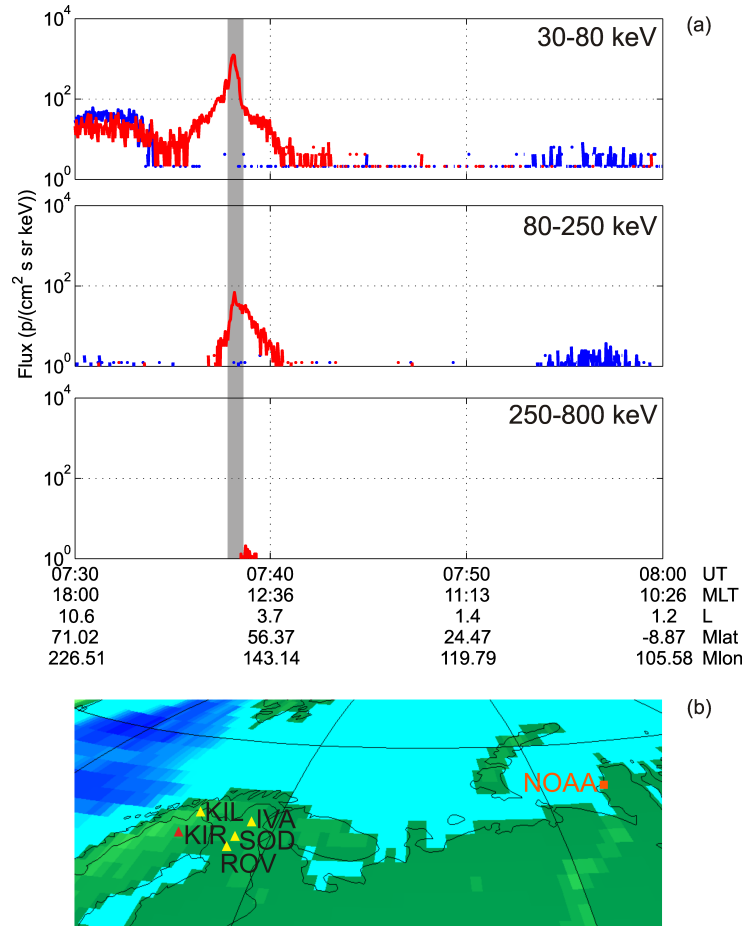
Figure 2.9: (a) Proton differential flux in three energy channels: $30 - 80$ keV (top), $80 - 250$ keV (middle), $250 - 800$ keV (bottom) registered by NOAA 17. Locally mirroring and precipitating particle fluxes are shown in red and blue color, respectively. At 07:38 UT (shadowed bar) the satellite was $\sim 40°$ east of the Scandinavian sector. (b) Location of NOAA 17 magnetically mapped to the ground with T96 with respect to the ground-based magnetometers.

During the day of September 25, the LEO orbit NOAA satellites registered enhanced precipitation of energetic protons at mid-latitudes, collocated in space and time with EMIC activity observed on the ground. We present two examples of such precipitation – at different UT times, but both in the morning MLT sec-

tors. At 07:38 UT, the NOAA 17 spacecraft registered a localized enhancement of precipitating protons with energies > 30 keV (shaded bar in Figure 2.9a) above the North of Russia, at $\sim 40°$ east of the Scandinavian sector. The position of NOAA 17 at 07:38 UT magnetically mapped to the ground is shown by the orange square in Figure 2.9b. The blue trace in Figure 2.9a shows the flux of precipitating protons (observed by the $0°$ detector) and the red trace shows the flux of locally mirroring protons (observed by the $90°$ detector) seen by MEPED. The three panels in Figure 2.9a show data from different energy channels between $30-80$ keV, $80-250$ keV, and $250-800$ keV, respectively. Following the classification of *Yahnin and Yahnina* (2007), we identify this proton event as LPEP of type 1, i.e., characterized by localization in the morning MLT sector during quiet geomagnetic conditions, without the presence of a precipitating energetic electron population, and in conjunction with structured Pc 1 pulsations observed on the ground. These authors note that generally during type 1 events, the precipitating flux is relatively small compared to the trapped flux which points to weak pitch-angle diffusion of particles with pitch-angles close to the loss cone.

Figure 2.9a also shows broader precipitation which comes from the so-called isotropic precipitation zone. This zone is magnetically conjugate to the midtail, where field lines are strongly stretched, and the ion gyroradius becomes comparable to the radius of curvature of the local magnetic field. Precipitation in this zone is non-adiabatic, and is of different origin than the one considered in this work.

At 17:51 UT, simultaneously with the EMIC activity seen on Cluster, the NOAA 17 spacecraft registered a localized enhancement of precipitating protons with energies > 30 keV (shaded bar in Figure 2.10) in LEO orbit over
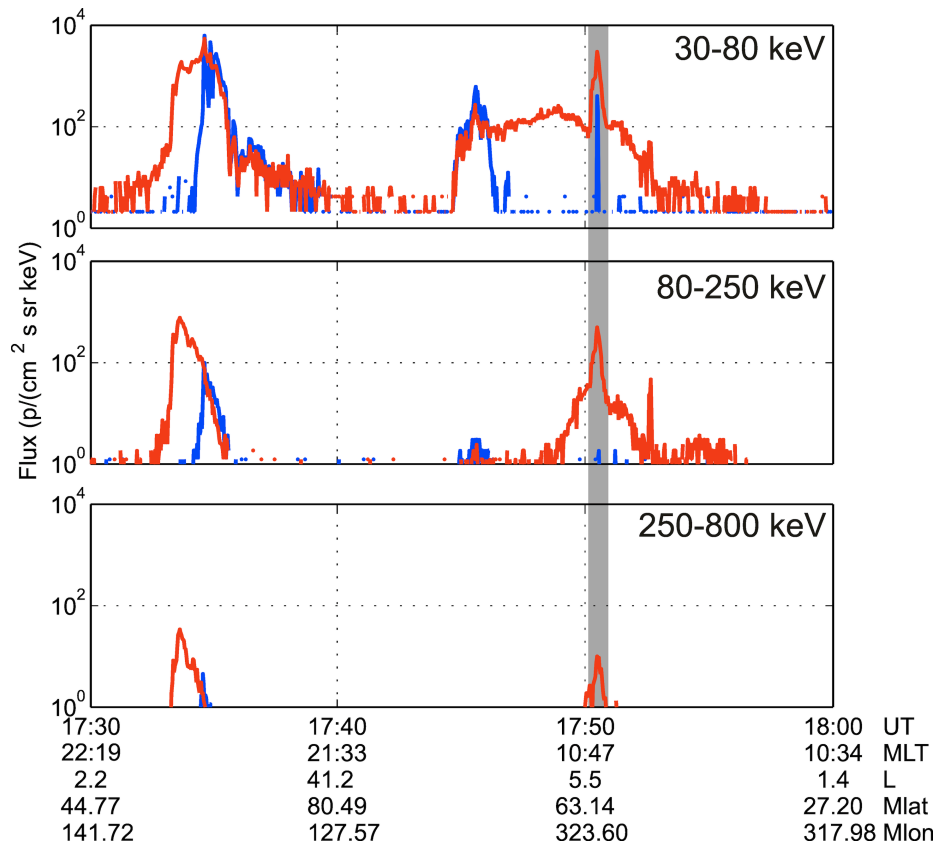
Figure 2.10: Similar to Figure 2.9a: proton differential flux in three energy channels: $30 - 80$ keV (top), $80 - 250$ keV (middle), $250 - 800$ keV (bottom) registered by NOAA 17. Locally mirroring and precipitating particle fluxes are shown in red and blue color, respectively. At 17:51 UT (shadowed bar) the satellite was above Canada, in good conjunction with Cluster 3, 4 and CARISMA (see Figure 2.6).

Canada, closely conjugate to both the Cluster 3, 4 satellites and CARISMA. The position of NOAA 17 at 17:51 UT magnetically mapped to the ground is shown by the orange square in Figure 2.6. Similar to Figure 2.9a, the blue trace denotes the flux of precipitating protons and the red trace shows the flux of locally mirroring protons registered by MEPED. In this case we can see that the precipitating flux in the first channel (Figure 2.10, top) is almost as intense as the mirroring flux, which serves as an indication of strong pitch-angle scattering for ions with energies between $30 - 80$ keV, while for the higher energies pitch-angle diffusion is weaker. The increase in the pitch-angle diffusion rate may be associated with the preceding injection of ions manifested by the enhancement in the AE index. Our observations suggest that strong energy-dependent ion loss may occur during periods of geomagnetic quiescence, but which are characterized by EMIC waves excited at mid-latitudes just inside the plasmapause by strong compression of the magnetosphere due to enhancement in solar wind dynamic pressure.

EMIC Wave Modulation by Lower-Frequency ULF Waves

Simultaneous CARISMA-Cluster observations also provide the opportunity to test the bouncing wave packet model and the theory of EMIC wave growth modulation by the lower frequency ULF waves. At multiple CARISMA and STEP magnetometer stations, the EMIC waves appear to be structured with repetition period of $130 - 140$ seconds (see Figure 2.11) across a relatively wide range of L-shells. Simultaneously with the waves on the ground, Cluster 3 and 4 registered EMIC waves with the same carrier frequency in the equatorial region magnetically conjugate to CARISMA. The equatorial location of the Cluster 3

and 4 observations and the left-handed EMIC wave polarization lead us to conclude that Cluster flew through the EMIC wave source region.
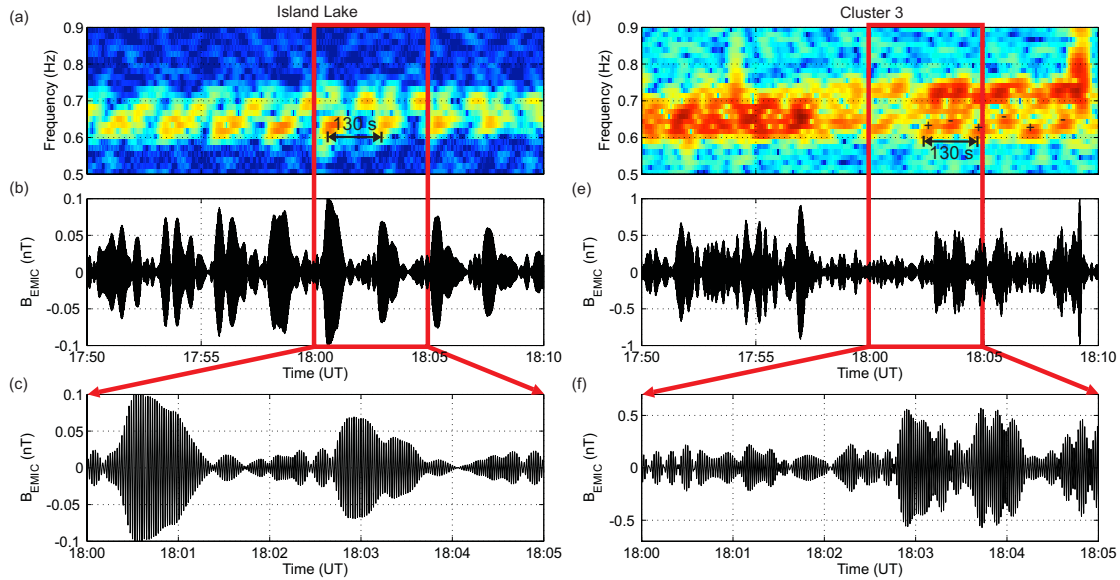
Figure 2.11: Fourier spectrograms and waveforms of the D-component at ISLL (left) and azimuthal magnetic field component at Cluster 3 (right) zoomed in between 17:50 and 18:10 UT and between 18:00 and 18:05 UT to show the EMIC wave packet details.

To illustrate details of the EMIC wave packet structure, we have selected a 20 minute interval that is shown in Figure 2.11. The left and the right panel show Fourier spectrograms and waveforms of the D-component at ISLL and azimuthal magnetic field component in FAC at Cluster 3, respectively, zoomed in between 17:50 and 18:10 UT and between 18:00 and 18:05 UT. On the ground, the EMIC wave packets repeat about every 130 seconds and this repetition period appears in spectrograms as stripes or blobs. The individual wave packets on Cluster 3 are more diffuse and it is harder to distinguish them. However, the wave packet structure is still seen after 18:00 UT in the spectrogram at frequencies below 0.65 Hz, which repeat every 65 seconds on Cluster 3 op-

posed to the 130 seconds on the ground. This observation suggest that the wave packets propagate bi-directionally in the source region, which we marked in the spectrogram in Figure 2.11d by the + and - signs, consistent with observations by *Loto'aniu et al.* (2005), while only every second wave packet is seen on the ground in the northern hemisphere. Following *Loto'aniu et al.* (2005), we computed the EMIC Poynting flux, using the FGM and EFW instruments on Cluster. However, due to the noise in the EFW data, the Poynting flux analysis does not show clear results. Nevertheless, there is some evidence of bi-directional propagation of the EMIC wave packets.

Also note that the EMIC wave spectrum after 18:00 UT bifurcates into two closely spaced bands which happens both in space and on the ground. Such multiple wave bands are often observed on the ground and were previously explained by EMIC wave generation at different source regions in the magnetosphere, each frequency band corresponding to the local ion gyrofrequency and their consequent ionospheric ducted propagation to the ground magnetometer station (*Yahnin et al.*, 2004). Since in our case the spectrum splitting occurs at the spacecraft this cannot be attributed to multiple-sources locations. Analysis of the wave properties in the generation region, potentially via self-consistent simulations, is warranted.

To test the ULF wave modulation hypothesis, we used the EDI electric and the FGM magnetic field measurements from Cluster. Prior to the analysis, Cluster electric and magnetic field data were transformed from GSM to the field-aligned coordinate system (*Rae et al.*, 2005) and FFT-transformed to the frequency domain. The time-series of the EDI electric field are shown in upper panels and the power spectral density in lower panels of Figure 2.12 for Cluster
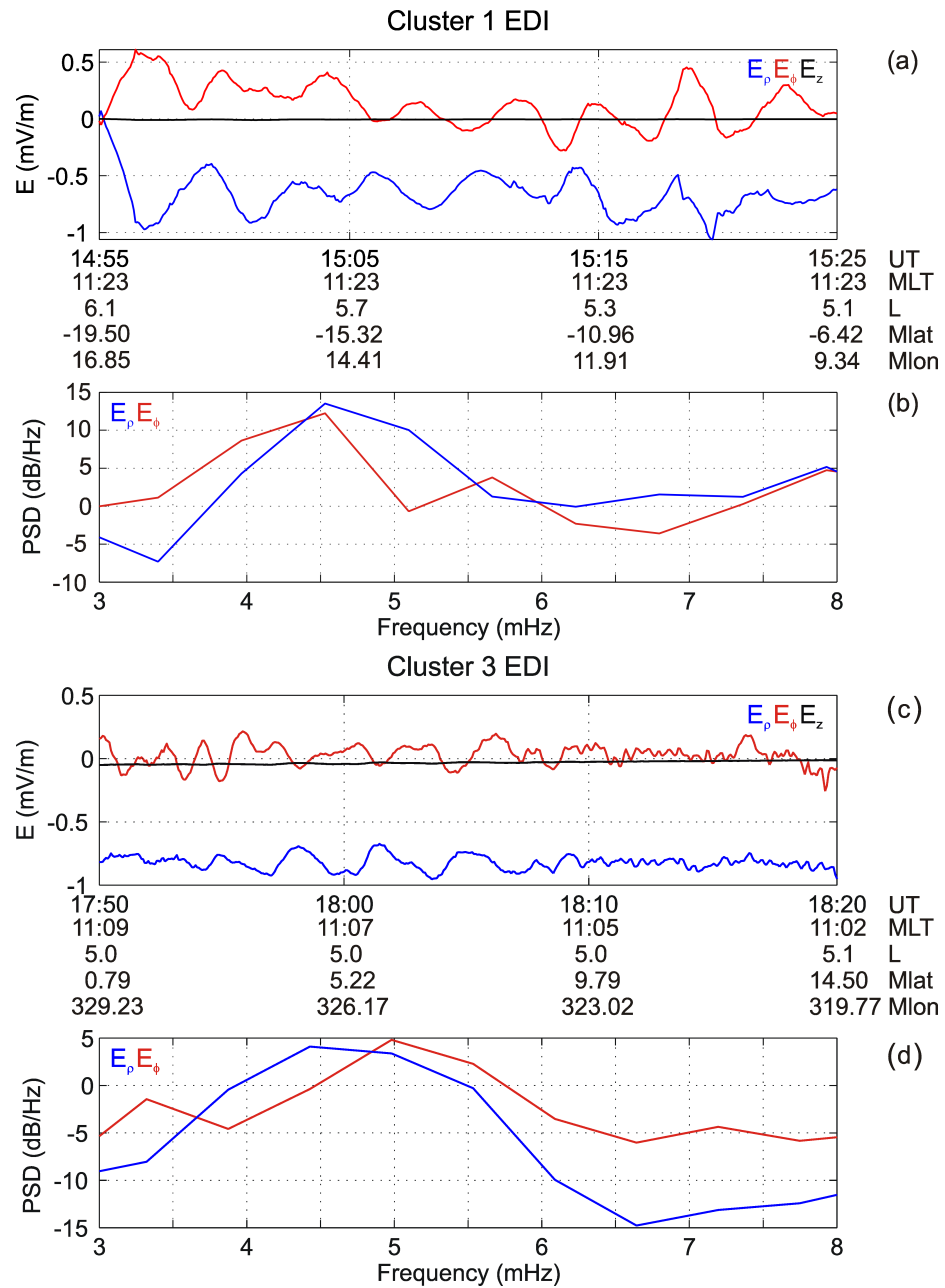
Figure 2.12: (a) EDI electric field time-series and (b) power spectral density between 14:55 – 15:25 UT, registered on Cluster 1; (c) EDI electric field time-series and (d) power spectral density between 17:50 – 18:20 UT, registered on Cluster 3.

1 and 3, respectively.

According to the EMIC wave modulation theory, the lower-frequency ULF waves with average period of $130 - 140$ seconds ($7.1 - 7.7$ mHz) should be observed in situ in the EMIC wave source region at the equator. However, these ultra low frequency waves are not seen in the magnetic field data – neither in the time series, nor in the spectrum (not shown). The Cluster 3 EDI electric field measurements do show the presence of ULF electric field (see Figure 2.12) with period of 192 ± 11 seconds (5.2 ± 0.3 mHz). Similar long-period ULF waves are found earlier in the Cluster 1 EDI data. However, this period is considerably longer than the observed EMIC wave packet repetition period on the ground. Magnetic field data obtained from CARISMA magnetometers do not show any presence of ULF waves with periods around $130 - 140$ seconds, either. To examine the feasibility of having local ULF waves with periods equal to the EMIC modulation period on the ground we applied cross-phase analysis (*Waters et al.*, 1996) to data from pairs of CARISMA magnetometers along the $\sim 330°$ magnetic meridian. This technique assumes that magnetic field-lines sustain standing Alfvén waves with frequencies depending on the field-line length and Alfvén speed along it. In order to extract field line resonance frequency values, amplitude and phase spectra from pairs of latitudinally separated ground-based magnetometers are compared to look for features of resonance. A peak of phase difference (cross-phase) occurs at the field-line resonance frequency of the field-line with its footprint at the mid-point between the two magnetometers. Figure 2.13 a shows the cross-phase spectra from the Island Lake and Gillam magnetometers (the closest pair to the Cluster 3, 4 footprints). Cross-phase FFT windows were 30 minutes long providing a frequency resolution of 0.5 mHz.
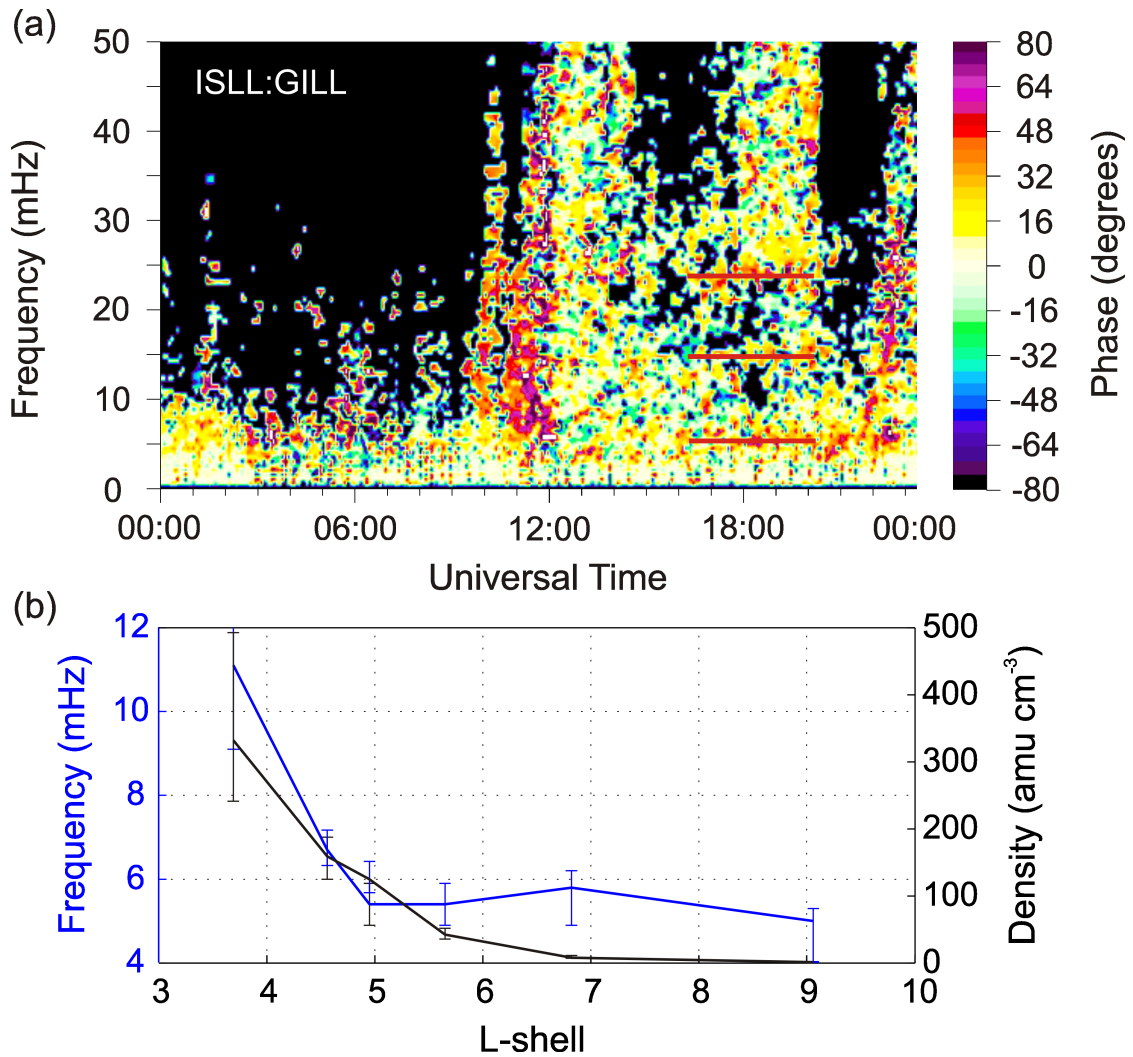
Figure 2.13: (a) Cross-phase spectra of local resonance modes at the mid-point between the Island Lake ($L = 5.23$) and Gillam ($L = 6.10$) stations. (b) The fundamental field-line resonance frequency (blue line) and equatorial mass density (black line) derived from ground-based cross-phase as a function of L.

There are three resonance modes seen in the spectra – the fundamental mode at 5.4 ± 0.5 mHz (185 ± 17 s), and the second and the third harmonics at 14.5 ± 0.5 mHz (69 ± 2 s) and 22.5 ± 0.5 mHz (44 ± 1 s), respectively (indicated in Figure 2.13a by horizontal red lines). The good agreement between the period of field-line fundamental mode and the period of electric field oscillations on Cluster and the absence of magnetic field oscillations on Cluster is consistent with this being an observation of the fundamental field-line standing Alfvén wave having a node at the equator in magnetic field and an antinode in the electric field (*Southwood and Kivelson*, 1981) (the absence of magnetic field oscillations at the resonance frequency on the ground might be due to the fact that this is a small spatial scale wave, strongly attenuated between the ionosphere and the ground (*Wright and Yeoman*, 1999). However, our observations do not agree with the theory that EMIC wave growth modulation by lower-frequency ULF magnetic pulsations can explain the form of structured Pc1 pulsations, since waves with period matching the EMIC repetition period on the ground were not found in the Cluster data.

Generally, high-harmonic ($n \geqslant 2$) field-line resonance eigenperiods, T_n can be used to calculate the Alfvénic travel time there and back along the field line $\tau = nT_n$ (*Schulz*, 1996). Assuming that EMIC waves propagate in the magnetosphere approximately at the Alfvén speed we have estimated the EMIC wave travel time there and back along the source field line to be $\tau = nT_n = 3 \times 44 = 132$ seconds. This is close to the repetition period of the wave packets seen on the ground. This good agreement between the estimated wave travel time along the magnetic field line and the EMIC wave repetition period on the ground, as well as the observation of a double-hop 65 second wave repetition period (although,

for a short interval of time) on Cluster, could be possibly explained by the wave packet bouncing between hemispheres.

The cross-phase analysis was also used to relate the observed electron density structures inferred from the WHISPER and EFW instruments at Cluster to a potential plasmapause location obtained from ground-based magnetometer measurements. Figure 2.13b shows the fundamental field-line resonance frequency (blue line) and equatorial mass density (black line) as functions of L-shell derived from the cross-phase analysis applied along the Churchill line at $330°$ magnetic meridian. Plasma mass densities were derived from the field-line resonance frequencies assuming a dipole field geometry and radial density distribution along field lines $\sim r^{-1}$ (*Dent et al.*, 2003). The plasma mass density profile shows consistency with WHISPER electron densities observed by Cluster 3, 4.

Conclusions

In this paper we have analyzed EMIC waves generated during solar wind driven magnetospheric compressions. Using conjugate observations from the Cluster satellites, and CARISMA and other ground-based magnetometers, we show that EMIC waves were excited in a high density region just inside the plasmapause. Importantly, we were also able to analyze the effect of these EMIC waves on energetic particle precipitation into the ionosphere. Data from an excellent additional conjunction to NOAA 17 indicated that a latitudinally localized band of $30 - 80$ keV proton precipitation was observed at low Earth orbit collocated with the Cluster observations of EMIC waves at higher equatorial altitudes on the same field lines. Using this ground-satellite conjunction, we were also able

to test the hypothesis that EMIC wave packet modulation as observed in Pc1 pearls such as those reported here might be due to EMIC wave growth rate modulation by longer period Pc5 ULF waves on the same field line. In this event, although we were able to clearly identify the local field line resonance mode, both on Cluster and on the ground, the fundamental frequency did not match the observed EMIC wave packet repetition period. Using the third standing field-line mode eigenperiod, we estimated the EMIC wave propagation time (there and back) along the field line and found it to be in good agreement with the EMIC wave packet repetition period on the ground. For a short time during the time of conjunction, EMIC wave packets were observed every 65 seconds on Cluster and every 130 seconds on the ground which suggests bi-directional propagation of EMIC wave packets in space. Together with the above estimate of the EMIC wave packet travel time may be explained within the bouncing wave packet hypothesis or some similar theory (*Demekhov*, 2007). Our observations support the earlier suggestion of *Usanova et al.* (2008) that magnetospheric compressions, during periods of enhanced solar wind dynamic pressure, could play an important role in the generation of EMIC waves in the inner magnetosphere, these waves being excited in a localized region just inside the plasmapause. This is consistent with the conclusion of *Anderson and Hamilton* (1993) that EMIC wave growth at higher L-shells was enhanced by the modest magnetospheric compression. Our observations confirm that EMIC waves can cause the precipitation of energetic protons into the ionosphere. Many previous studies such as those of *Sandanger et al.* (2009) having inferred EMIC waves might have been responsible for proton precipitation spikes inside the plasmapause observed at LEO but without any direct evidence of the hypothesised EMIC

waves themselves. Interestingly, *Sandanger et al.* (2007) also report evidence that these proton precipitation events are often also collocated with regions of MeV energy electron precipitation from the radiation belts. Consequently, we suggest that compression-related EMIC waves such as those we reported here could also be responsible for the loss of particles from the radiation belts, as well as from the ring current. Future studies should continue to examine mechanisms for EMIC wave generation and the role of EMIC waves in the dynamics and loss of energetic ions in the ring current and electrons in the outer radiation belts during periods of magnetospheric compression occurring due to enhanced solar wind dynamic pressure.

2.3 Multiple Ground-based Observations of EMIC Waves During Magnetospheric Compressions

Following the observations of compression-related EMIC waves from June 29, 2007 (Section 2.1) and September 25, 2005 (Section 2.2), in this section we present some additional examples of EMIC waves observed in the inner dayside magnetosphere during periods of enhanced solar wind dynamic pressure and consequent magnetospheric compression. For example, Figures 2.14 and 2.15 illustrate EMIC wave activity on the ground from November 19, 2007 and April 11, 2005 which were observed together with enhanced solar wind dynamic pressure (red curve) and simultaneous enhancement of H_p magnetic field component on GOES 12 (blue curve) after multiple days (five, and more than two weeks, respectively) of quiet geomagnetic conditions. On the ground, the EMIC

waves were observed by the magnetometer station in Gakona, Alaska at the magnetic footprint of $L \sim 5$.
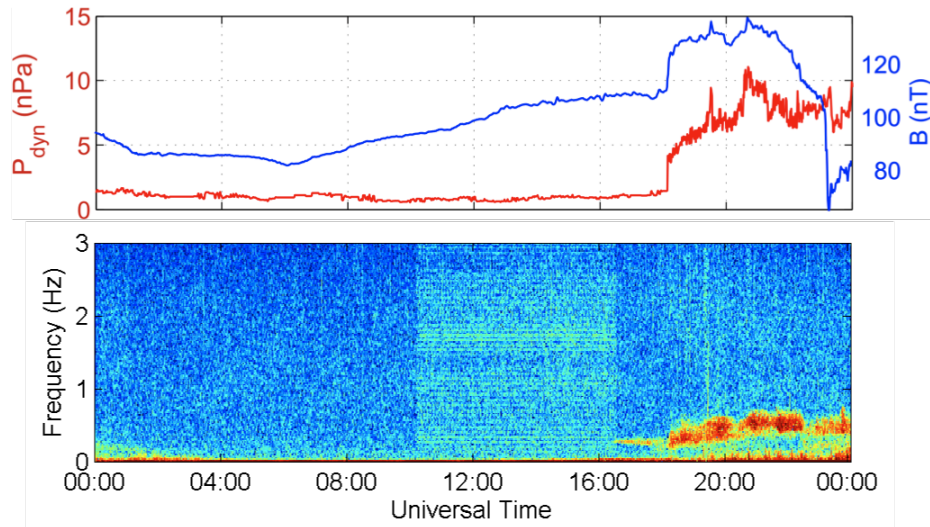
Figure 2.14: Compression-related EMIC wave event from November 19, 2007. The upper panel shows the solar wind dynamic pressure (red line) and the magnetic field magnitude observed at GOES 12 (blue line). The bottom panel shows the spectrogram of the D-component of magnetic field at Gakona.

The EMIC wave activity from December 16, 2006 shown in Figure 2.16 occurred during the storm recovery phase and will be discussed in more detail in the next section. The waves for this event were seen on the ground at magnetic footprints of multiple L-shells between $L = 3.93 - 7.61$, in particular, at Gakona (middle panel in Figure 2.16) as well as in situ at geosynchronous orbit by GOES 12 (bottom panel in Figure 2.16). The waves were seen for many hours before the enhancement in the solar wind dynamic pressure and consequent increase in the magnetic field strength at GOES 12, which implies that there were some processes other than the compression generating EMIC waves. However, at these L-shells it is clear that the wave activity was intensified simultaneously with the enhanced solar wind dynamic and associated compression of the mag-
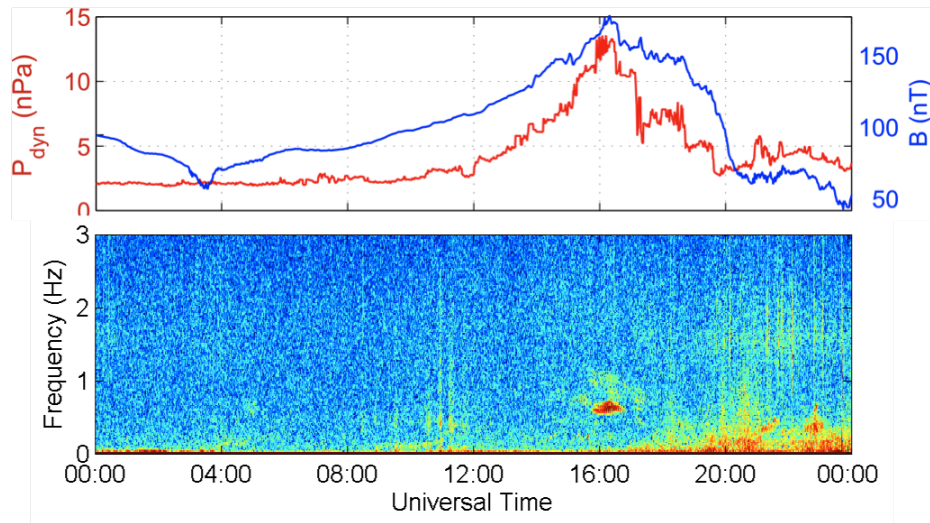
Figure 2.15: Compression-related EMIC wave event from April 11, 2005. The upper panel shows the solar wind dynamic pressure (red line) and the magnetic field magnitude observed at GOES 12 (blue line). The bottom panel shows the spectrogram of the D-component of magnetic field at Gakona.

netic field observed on GOES 12.

We have also performed a multi-event study based on the OMNI solar wind density and dynamic pressure (at the subsolar magnetopause), GOES magnetic field, and STEP ground-based magnetometer data between September 2007 – July 2008. We selected all compression events with the following criteria: an enhancement in the solar wind density of at least 8 p/cm^3 lasting for at least one hour, and the presence of enhanced H_p magnetic field component on GOES 11 and/or GOES 12. This produced 38 events listed in Table 2.2. During the selected compression intervals, we looked for EMIC wave activity using STEP searchcoil magnetometer data located in the vicinity of GOES magnetic foot-prints at Gakona (GKN; $L = 4.95$), Fort St. John (FSJ; $L = 4.59$), Fort Nelson (FTN; $L = 5.36$), Parksite (PKS; $L = 4.22$) and Lucky Lake (LCL; $L = 3.93$). In 70% of the events, EMIC waves were observed on the ground by the STEP mag-
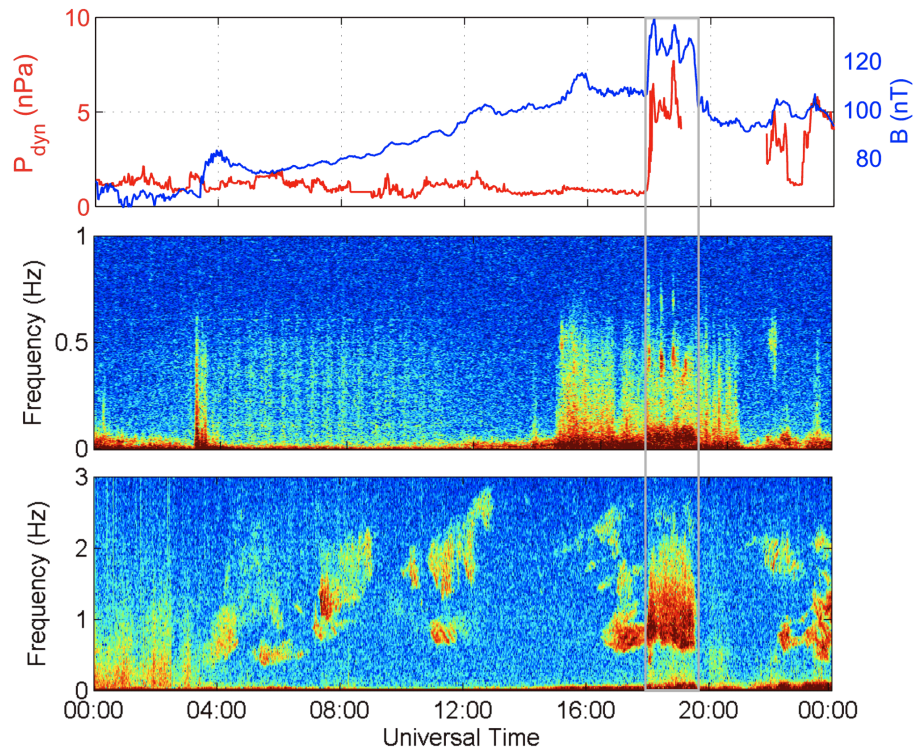
Figure 2.16: Compression-related EMIC wave event from December 16, 2006. The upper panel shows the solar wind dynamic pressure (red line) and the magnetic field magnitude observed at GOES 12 (blue line). The middle panel shows the spectrogram of the D-component of magnetic field at Gakona. The bottom panel shows the spectrogram of the H_n (perpendicular) component of magnetic field on GOES 12. The grey bar highlights the interval of interest.

	Date	Time (UT)	n (p/cm^3)	Satellite name	Station name
1	Sep 6, 2007	16 – 22	10	G11	–
2	Sep 14, 2007	15 – 22	60	G11,12	PKS, GKN
3	Sep 20, 2007	10 – 15	50	G12	PKS, GKN
4	Sep 27, 2007	12 – 19	30	G11,12	PKS, GKN
5	Sep 28, 2007	16 – 18	12	G12	–
6	Oct 22, 2007	14 – 23	9	G11	GKN, LCL
7	Oct 24, 2007	17 – 23	11	G12	GKN, FSJ
8	Oct 25, 2007	11 – 16	30	G12	–
9	Nov 8, 2007	09 – 16	20	G12	–
10	Nov 12 – 13, 2007	22 – 04	25	G11	GKN, PKS
11	Nov 19 – 20, 2007	18 – 02	30	G11,12	FTN, GKN
12	Nov 22, 2007	10 – 23	12	G12	GKN, LCL
13	Nov 30, 2007	18 – 22	20	G11,12	GKN, LCL
14	Dec 4, 2007	13 – 23	16	G12	FTN
15	Dec 9, 2007	00 – 03	20	G11	–
16	Dec 10, 2007	16 – 22	20	G11	GKN, PKS
17	Dec 27 – 28, 2007	22 – 05	25	G11	–
18	Dec 28, 2007	16 – 21	15	G12	–
19	Dec 30, 2007	12 – 16	20	G12	–
20	Dec 31, 2007	12 – 19	20	G11,12	–
21	Jan 4 – 5, 2008	23 – 07	40	G11	GKN, FTN
22	Jan 25, 2008	01 – 02	12	G11	GKN
23	Jan 29, 2008	00 – 07	10	G11	GKN
24	Jan 31, 2008	11 – 23	40	G11,12	GKN, PKS
25	Feb 9 – 10, 2008	19 – 07	25	G11,12	GKN, PKS
26	Feb 27, 2008	15 – 18	30	G11,12	GKN, PKS
27	Mar 8, 2008	07 – 18	35	G12	FSJ, PKS
28	Mar 25, 2008	18 – 23	12	G12	GKN, PKS
29	Apr 4, 2008	15 – 20	15	G11,12	GKN, PKS, LCL
30	Apr 22, 2008	13 – 23	18	G11,12	GKN, PKS
31	Apr 30, 2008	16 – 19	35	G11,12	GKN, LCL
32	May 10 – 11, 2008	22 – 03	17	G11	–
33	Jun 9, 2008	20 – 22	10	G11,12	–
34	Jun 10, 2008	14 – 19	8	G12	FSJ
35	Jun 14, 2008	12 – 17	45	G11,12	GKN, PKS
36	Jun 24, 2008	20 – 00	20	G11,12	GKN
37	Jun 25, 2008	16 – 18	25	G11,12	–
38	Jul 11, 2008	20 – 23	15	G11	PKS, LCL

Table 2.2: Magnetospheric compression events associated with enhanced solar wind dynamic pressure and density between September 2007 – July 2008. The third column shows stations where EMIC waves were detected.

netometers. Overall, our conclusion is that compression-related EMIC waves very often can be excited in the inner magnetosphere over a wide range of levels of geomagnetic activity. Further analysis of in situ Pc1 wave activity on GOES 11 and GOES 12 is warranted, but this will be the subject of future work.

2.4 EMIC-related Pitch-angle Diffusion of Energetic Ions and MeV Electrons Observed on NOAA

2.4.1 MeV Electron Registration on September 25, 2005

The most energetic channel of the NOAA MEPED detector which is supposed to measure fluxes of protons with energies > 6900 keV turned out to be also sensitive to electrons with energies > 800 keV. This artifact allows us to monitor energetic electron fluxes in conjunction with EMIC waves on the ground.

Following *Sandanger et al.* (2007); *Miyoshi et al.* (2008); *Sandanger et al.* (2009) who demonstrated some examples of observed simultaneous (EMIC-related) increases in precipitating $30 - 80$ keV proton fluxes and energetic MeV fluxes near the plasmapause, we looked for similar features in our data. Figure 2.17 (a replotted version of Figure 2.10 with MeV electron flux added) shows an example of MeV electron registration. During the proton precipitation event from September 25, 2005, associated precipitating MeV electron flux was not observed, as shown in Figure 2.17, despite the fact that the EMIC-related precipitation of the energetic protons mapped to high plasma density region inside the plasmapause, similarly to the observations reported by *Sandanger et al.* (2007); *Miyoshi et al.* (2008); *Sandanger et al.* (2009). Locally mirroring electrons are seen

close to EMIC-related proton precipitation, but they do not appear to be related to the spatially narrow ion precipitation feature. Indeed, these broader MeV electron flux enhancement is most likely simply a representation of the outer radiation belt crossing. More examples of concurrent observations of energetic protons and MeV electrons will be presented in the next subsection.

2.4.2 Pitch-angle Diffusion of Energetic Ions and MeV Electrons During the Recovery Phase of December 15, 2006 Storm

Following a minimum Dst of -140 nT on December 15, 2006, EMIC wave activity was detected by ground-based magnetometers in the North-American sector between December 15 – 18 (Figure 2.18) and Scandinavian sectors (not shown here) for multiple days. The Dst index between December 15 – 18 is shown in Figure 2.19.

During the storm recovery phase, the NOAA satellites had multiple conjunctions with the ground magnetometers and registered enhancements of trapped and precipitating ion fluxes at the locations magnetically conjugate to regions of EMIC wave activity on the ground. Examples of energetic particle registration when NOAA was magnetically conjugate to regions of EMIC wave activity on the ground are shown in Figures 2.20 and 2.21. We have found a total of ~ 20 such events; in each case the location of ion precipitation magnetically maps close to the position of the plasmapause determined empirically using $L_{pp} = 5.6 - 0.44\ Kp_{max}$, where Kp_{max} is the maximum Kp index within the preceding 24 hours (*Carpenter and Anderson*, 1992). Sometimes, but not always,
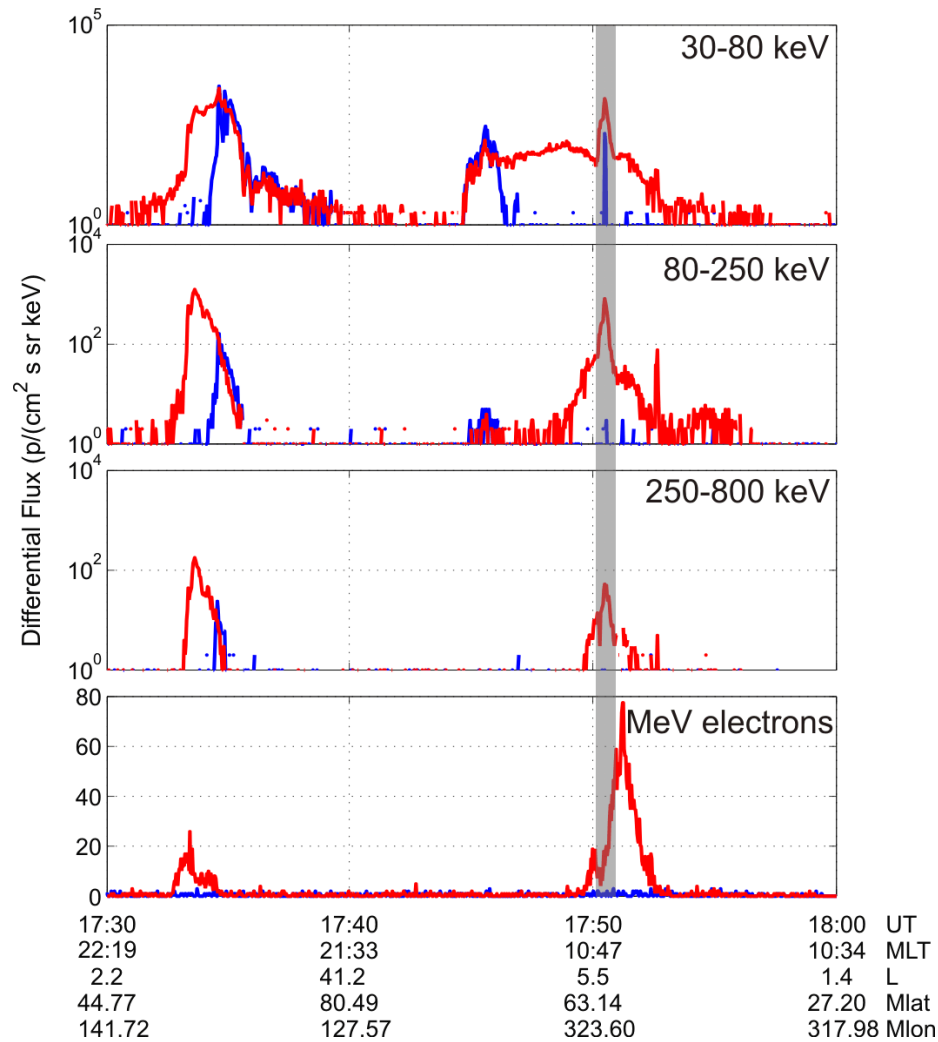
Figure 2.17: Proton differential flux in three energy channels (top three panels) and MeV electron differential flux (bottom panel) registered by NOAA 17 on September 25, 2005. Locally mirroring and precipitating particle fluxes are shown in red and blue color, respectively. At 17:51 UT (shadowed bar) the satellite was above Canada, in good conjunction with Cluster 3, 4 and CARISMA (see Figure 2.6).
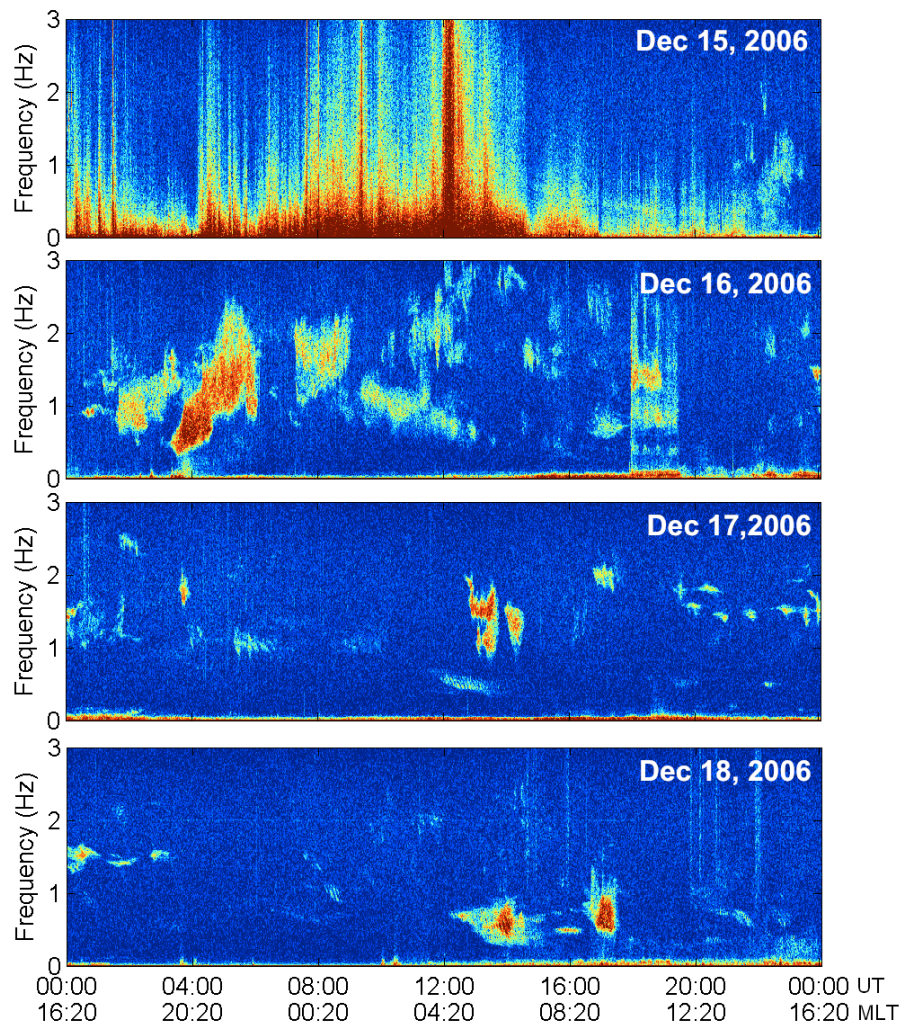
Figure 2.18: Daily EMIC wave activity at Parksite between December 15 – 18, 2006 (top to bottom panels, respectively).
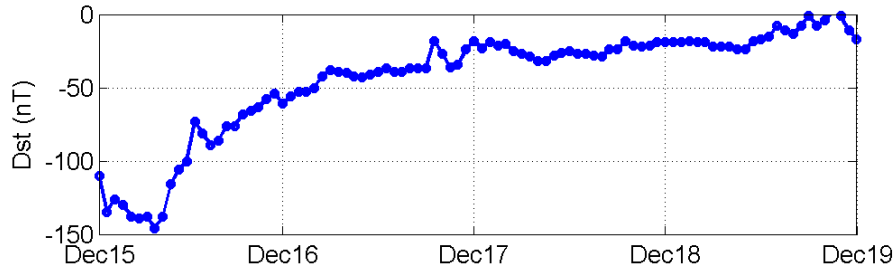
Figure 2.19: Dst index between December $15 - 18$, 2006.

the enhancements in the proton flux were accompanied by enhancements in the flux of MeV electrons mirroring at the spacecraft location. Such enhancements in the mirroring flux indicate weak to moderate pitch-angle diffusion. We have found that there is no unambiguous correlation between the energetic ion and inferred MeV electron pitch angle diffusion intensity. For example, Figure 2.20 shows a signature of strong pitch-angle diffusion of protons with energies $30 - 800$ keV at 04:33 UT (highlighted by the grey bar) seen as an enhancement of both the trapped and the precipitating flux. However, in the higher energy channel which also register MeV electrons, no indication of precipitation or enhanced pitch-angle diffusion is seen. In contrast, Figure 2.21 shows an example of a localized enhancement of locally mirroring MeV electron flux at 21:53 UT (red curve) in the location marked by the grey bar, while enhancement in the energetic proton flux at the same time is relatively small.

Since simultaneous precipitation of energetic protons and MeV electrons was not observed in these examples, we suggest that further analysis of magnetic field and energetic particle data has to be carried out in order to investigate the conditions required for EMIC wave interaction with MeV electrons. Small number of events suggests that EMIC waves may be a necessary but not suffi-
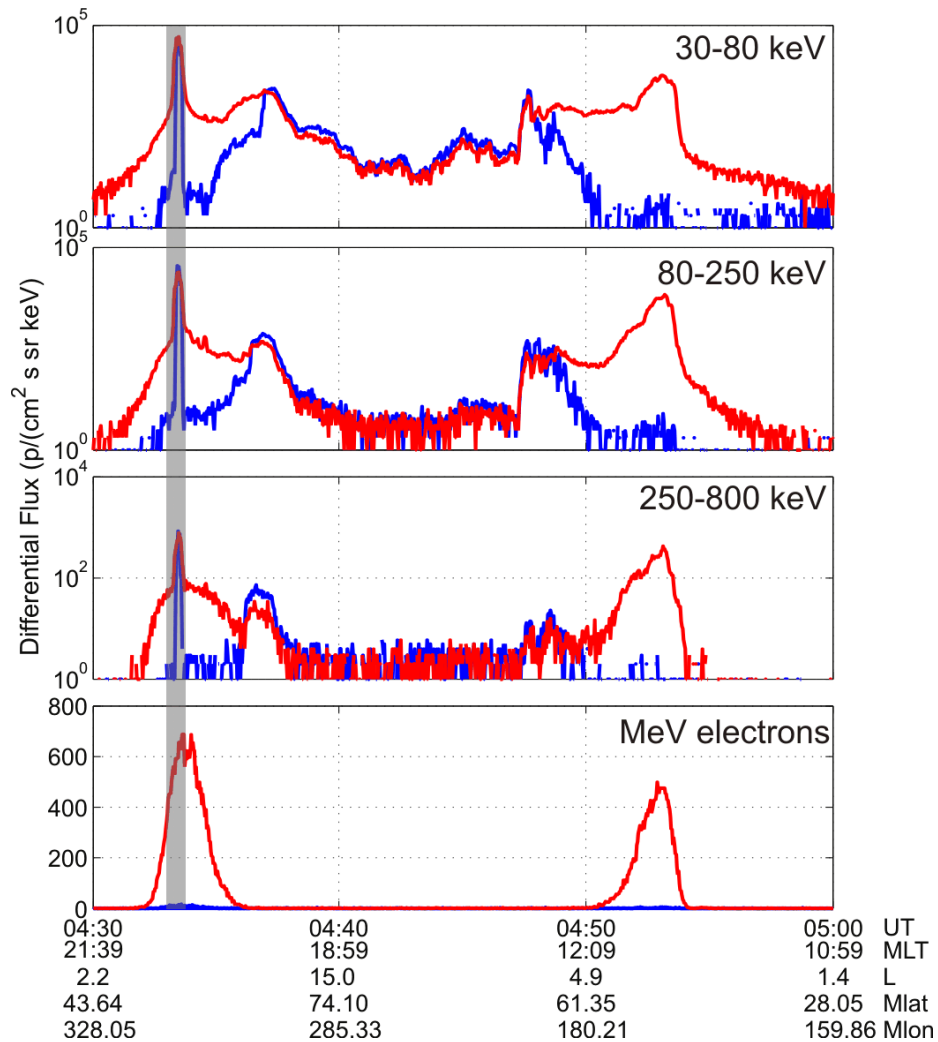
Figure 2.20: NOAA 17 pass between 4:30 – 5:00 UT on December 16, 2006. Protons (top three panels) and electrons (bottom panel) detected by the horizontal (red) and the vertical (blue) MEPED detectors. The shaded bar corresponds to the location magnetically mapped to the Parksite magnetometer.
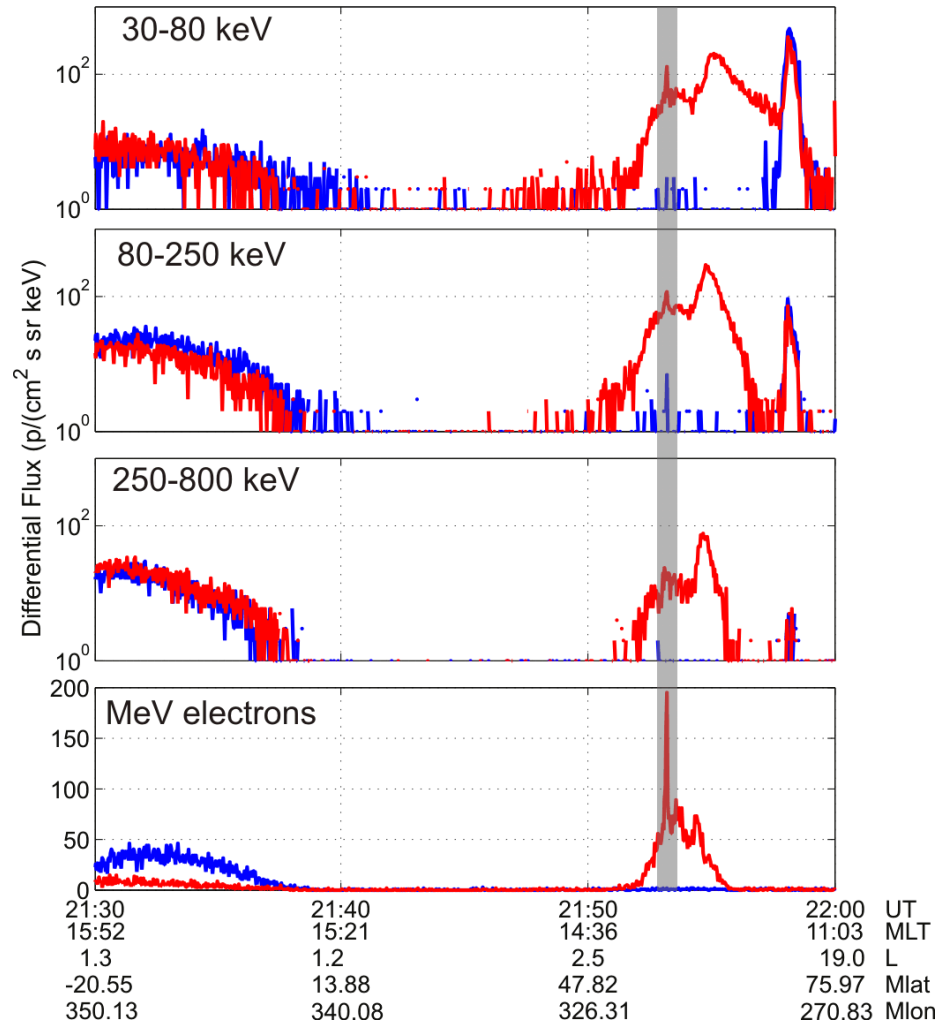
Figure 2.21: NOAA 16 pass between 21:30 – 22:00 UT on December 18, 2006. Protons (top three panels) and electrons (bottom panel) detected by the horizontal (red) and the vertical (blue) MEPED detectors. The shaded bar corresponds to the location magnetically mapped to the Parksite magnetometer.

cient condition for MeV electron precipitation, and future work should examine these relationship in details.

2.5 Conclusions

In this chapter multiple observations of EMIC wave activity both in space and on the ground have been presented. It has been shown that EMIC wave activity can be intensified during magnetospheric compressions associated with enhanced solar wind dynamic pressure. Contrary to earlier studies, it has been demonstrated that magnetospheric compressions are important for EMIC wave generation not only close to the subsolar magnetopause but also in the inner dayside magnetosphere.

Using satellite measurements, it has been shown that the EMIC waves were generated in regions of enhanced plasma density, just inside the plasmapause. It has been also shown that the EMIC wave repetition period in the ground cannot be explained by the ULF wave modulation theory, at least in one case presented here.

Observations presented in this chapter also confirm that EMIC waves can cause precipitation of energetic protons and in some cases appear to cause simultaneous pitch-angle diffusion of MeV energy electrons which may aid their loss from the radiation belts into the ionosphere. Since concurrent spikes in proton and electron flux were not always observed, the role of EMIC waves in the depletion of the radiation belts will be the subject of further studies.

Bibliography

Anderson, B., and D. Hamilton (1993), Electromagnetic ion cyclotron waves stimulated by modest magnetospheric compressions, *J. Geophys. Res.*, *98*, 11,369–11,382.

Anderson, B. J., R. E. Erlandson, and L. J. Zanetti (1992), A statistical study of Pc 1-2 magnetic pulsations in the equatorial magnetosphere. I - Equatorial occurrence distributions. II - Wave properties, *J. Geophys. Res.*, *97*, 3075–3101, doi:10.1029/91JA02706.

Arnoldy, R. L., et al. (2005), Pc 1 waves and associated unstable distributions of magnetospheric protons observed during a solar wind pressure pulse, *J. Geophys. Res.*, *110*, 7229, doi:10.1029/2005JA011041.

Auster, H. U., et al. (2008), The THEMIS Fluxgate Magnetometer, *Space Sci. Rev.*, *141*, 235–264, doi:10.1007/s11214-008-9365-9.

Balogh, A., et al. (2001), The Cluster Magnetic Field Investigation: overview of in-flight performance and initial results, *Ann. Geophys.*, *19*, 1207–1217.

Bonnell, J. W., F. S. Mozer, G. T. Delory, A. J. Hull, R. E. Ergun, C. M. Cully, V. Angelopoulos, and P. R. Harvey (2008), The Electric Field Instrument (EFI) for THEMIS, *Space Sci. Rev.*, *141*, 303–341, doi:10.1007/s11214-008-9469-2.

Carpenter, D. L., and R. R. Anderson (1992), An ISEE/Whistler model of equatorial electron density in the magnetosphere, *J. Geophys. Res.*, *97*, 1097–1108, doi:10.1029/91JA01548.

Cornwall, J. M. (1965), Cyclotron instabilities and electromagnetic emissions in the ultra low frequency and very low frequency ranges, *J. Geophys. Res.*, *70*, 61–69.

Décréau, P. M. E. (2001), Early results from the whisper instrument on cluster: an overview, *Ann. Geophys.*, *69*(14), 1241–1258.

Demekhov, A. (2007), Recent progress in understanding Pc1 pearl formation, *Journal of Atmospheric and Solar-Terrestrial Physics*, *69*, 1609–1622, doi:10.1016/j.jastp.2007.01.014.

Dent, Z. C., I. R. Mann, F. W. Menk, J. Goldstein, C. R. Wilford, M. A. Clilverd, and L. G. Ozeke (2003), A coordinated ground-based and image satellite study of quiet-time plasmaspheric density profiles, *Geophys. Res. Lett.*, *30*(12), 1600.

Denton, R. E., J. LaBelle, and X. Zhu (1992), Viking magnetic and electric field observations of periodic pc 1 waves: Pearl pulsations, *J. Geophys. Res.*, *97*(A10), 14,82314,832.

Denton, R. E., J. LaBelle, and X. Zhu (2002), Location of pc 1-2 waves relative to the magnetopause, *Ann. Geophys.*, *20*, 1763–1767.

Engebretson, M. J., W. K. Peterson, J. L. Posch, M. R. Klatt, B. J. Anderson, C. T. Russell, H. J. Singer, R. L. Arnoldy, and H. Fukunishi (2002), Observations of two types of Pc 1-2 pulsations in the outer dayside magnetosphere, *J. Geophys. Res.*, *107*, 1451, doi:10.1029/2001JA000198.

Escoubet, C., M. Fehringer, and M. Goldstein (2001), The cluster mission, *Ann. Geophys.*, *19*, 1197–1200.

Evans, D., and M. Greer (2000), Polar orbiting environmental satellite space environment monitor 2: Instrument description and archive data documentation, *NOAA Tech.Memo.OAR SEC-93*.

Fraser, B. J. (1976), Pc 1 geomagnetic pulsation source regions and ionospheric waveguide propagation, *Journal of Atmospheric and Terrestrial Physics*, *38*, 1141–1146.

Fraser, B. J. (1985), Observations of ion cyclotron waves near synchronous orbit and on the ground, *Space Sci. Rev.*, *42*, 357–374, doi:10.1007/BF00214993.

Fraser, B. J., J. C. Samson, Y. D. Hu, R. L. McPherron, and C. T. Russell (1992), Electromagnetic ion cyclotron waves observed near the oxygen cyclotron frequency by ISEE 1 and 2, *J. Geophys. Res.*, *97*, 3063–3074, doi: 10.1029/91JA02447.

Fraser, B. J., H. J. Singer, W. J. Hughes, J. R. Wygant, R. R. Anderson, and Y. D. Hu (1996), CRRES Poynting vector observations of electromagnetic ion cyclotron waves near the plasmapause, *J. Geophys. Res.*, *101*, 15,331–15,344, doi: 10.1029/95JA03480.

Gendrin, R. (1975), Is the plasmapause a preferential region for proton precipitation, *Annales de Geophysique*, *31*, 127–135.

Gendrin, R., M. Ashour-Abdalla, Y. Omura, and K. Quest (1984), Linear analysis of ion cyclotron interaction in a multicomponent plasma, *J. Geophys. Res.*, *89*, 9119–9124, doi:10.1029/JA089iA10p09119.

Gustafsson, G., et al. (2001), First results of electric field and density observations by Cluster EFW based on initial months of operation, *Ann. Geophys.*, *19*, 1219–1240.

Hansen, H. J., B. J. Fraser, F. W. Menk, Y. Hu, P. T. Newell, C. Meng, and R. J. Morris (1992), High-latitude Pc 1 bursts arising in the dayside boundary layer region, *J. Geophys. Res.*, *97*, 3993–4008, doi:10.1029/91JA01456.

Hayakawa, M., S. Shimakura, T. Kobayashi, and N. Sato (1992), A study of polarization of irregular pulsations of diminishing period and their generation mechanism, *Planet. Space Sci.*, *40*, 1081–1091, doi:10.1016/0032-0633(92)90037-O.

Horne, R. B., and R. M. Thorne (1993), On the preferred source location for the convective amplification of ion cyclotron waves, *J. Geophys. Res.*, *98*, 9233–9247, doi:10.1029/92JA02972.

Horne, R. B., and R. M. Thorne (1994), Convective instabilities of electromagnetic ion cyclotron waves in the outer magnetosphere, *J. Geophys. Res.*, *99*, 17,259, doi:10.1029/94JA01259.

Jacobs, J. A., and T. Watanabe (1964), Micropulsation whistlers, *Journal of Atmospheric and Terrestrial Physics*, *26*, 825–826, doi:10.1016/0021-9169(64)90180-1.

Johnson, J. R., and C. Z. Cheng (1999), Can ion cyclotron waves propagate to the ground?, *Geophys. Res. Lett.*, *26*, 671–674, doi:10.1029/1999GL900074.

Jordanova, V. K., J. U. Kozyra, A. F. Nagy, and G. V. Khazanov (1997), Kinetic model of the ring current-atmosphere interactions, *J. Geophys. Res.*, *102*, 14,279–14,292, doi:10.1029/96JA03699.

Kale, Z. C., I. R. Mann, C. L. Waters, J. Goldstein, F. W. Menk, and L. G. Ozeke (2007), Ground magnetometer observation of a cross-phase reversal at a steep plasmapause, *J. Geophys. Res.*, *112*, 10,222, doi:10.1029/2007JA012367.

King, J., and N. Papitashvili (2004), Solar wind spatial scales in and comparisons of hourly Wind and ACE plasma and magnetic field data, *J. Geophys. Res.*, *110*, doi:10.1029/2004JA010804.

Kozyra, J. U., T. E. Cravens, A. F. Nagy, E. G. Fontheim, and R. S. B. Ong (1984), Effects of energetic heavy ions on electromagnetic ion cyclotron wave generation in the plasmapause region, *J. Geophys. Res.*, *89*, 2217–2233, doi:10.1029/JA089iA04p02217.

Li, X., D. N. Baker, T. P. O'Brien, L. Xie, and Q. G. Zong (2006), Correlation between the inner edge of outer radiation belt electrons and the innermost plasmapause location, *Geophys. Res. Lett.*, *33*, 14,107, doi:10.1029/2006GL026294.

Loto'aniu, T. M., B. J. Fraser, and C. L. Waters (2005), Propagation of electromagnetic ion cyclotron wave energy in the magnetosphere, *J. Geophys. Res.*, *110*, 7214, doi:10.1029/2004JA010816.

Loto'aniu, T. M., B. J. Fraser, and C. L. Waters (2009), The modulation of electromagnetic ion cyclotron waves by Pc 5 ULF waves, *Ann. Geophys.*, *27*, 121–130.

Mann, I. R., et al. (2008), The Upgraded CARISMA Magnetometer Array in the THEMIS Era, *Space Sci. Rev.*, *141*, 413–451, doi:10.1007/s11214-008-9457-6.

Menk, F. W., B. J. Fraser, H. J. Hansen, P. T. Newell, C. Meng, and R. J. Morris (1992), Identification of the magnetospheric cusp and cleft using Pc1-2 ULF pulsations, *Journal of Atmospheric and Terrestrial Physics*, *54*, 1021–1042.

Miyoshi, Y., K. Sakaguchi, K. Shiokawa, D. Evans, J. Albert, M. Connors, and V. Jordanova (2008), Precipitation of radiation belt electrons by EMIC waves, observed from ground and space, *Geophys. Res. Lett.*, *35*, 23,101, doi:10.1029/2008GL035727.

Mursula, K., R. Rasinkangas, T. Bösinger, R. E. Erlandson, and P. Lindqvist (1997), Nonbouncing Pc 1 wave bursts, *J. Geophys. Res.*, *102*, 17,611–17,624, doi:10.1029/97JA01080.

Mursula, K., T. Bräysy, P. Rasinkangas, R. andTanskanen, and F. Mozer (1999), A modulated multiband Pc1 event observed by POLAR/EFI around the plasmapause, *Advances in Space Research*, *24*, 81–84, doi:10.1016/S0273-1177(99)00429-9.

Mursula, K., T. Bräysy, K. Niskala, and C. T. Russell (2001), Pc1 pearls revisited: Structured electromagnetic ion cyclotron waves on Polar satellite and on ground, *J. Geophys. Res.*, *106*, 29,543–29,554, doi:10.1029/2000JA003044.

Olson, J. V., and L. C. Lee (1983), Pc1 wave generation by sudden impulses, *Planetary and Space Science*, *31*(3), 295 – 302, doi:10.1016/0032-0633(83)90079-X.

Parent, A., I. R. Mann, and K. Shiokawa (2007), Observing the MLT and L-shell dependence of ground magnetic signatures of the ionospheric Alfvén resonator, in *Proceedings of the Eighth Conference on Substorms (ICS-8)*, edited by Syrjäsuo and Donovan, pp. 225–230, University of Calgary, Alberta, Canada.

Paschmann, G., et al. (2001), The Electron Drift Instrument on Cluster: overview of first results, *Ann. Geophys.*, *19*, 1273–1288.

Pedersen, A., et al. (2001), Four-point high time resolution information on electron densities by the electric field experiments (EFW) on Cluster, *Annales Geophysicae*, *19*, 1483–1489.

Rae, I. J., et al. (2005), Evolution and characteristics of global Pc5 ULF waves during a high solar wind speed interval, *J. Geophys. Res.*, *110*, 12,211, doi:10.1029/2005JA011007.

Rasinkangas, R., and K. Mursula (1998), Modulation of magnetospheric EMIC waves by Pc 3 pulsations of upstream origin, *Geophys. Res. Lett.*, *25*, 869–872, doi:10.1029/98GL50415.

Sandanger, M., F. Søraas, K. Aarsnes, K. Oksavik, and D. S. Evans (2007), Loss of relativistic electrons: Evidence for pitch angle scattering by electromagnetic ion cyclotron waves excited by unstable ring current protons, *J. Geophys. Res.*, *112*, 12,213, doi:10.1029/2006JA012138.

Sandanger, M. I., F. Søraas, M. Sørbø, K. Aarsnes, K. Oksavik, and D. S. Evans (2009), Relativistic electron losses related to EMIC waves during CIR and CME storms, *Journal of Atmospheric and Solar-Terrestrial Physics*, *71*, 1126–1144, doi:10.1016/j.jastp.2008.07.006.

Schulz, M. (1996), Eigenfrequencies of geomagnetic field lines and implications for plasma-density modeling, *J. Geophys. Res.*, *101*, 17,385–17,398, doi:10.1029/95JA03727.

Sibeck, D. G., and V. Angelopoulos (2008), THEMIS Science Objectives and Mission Phases, *Space Sci. Rev.*, *141*, 35–59, doi:10.1007/s11214-008-9393-5.

Singer, H., L. Matheson, R. Grubb, A. Newman, and D. Bouwer (1996), Monitoring space weather with the GOES magnetometers, in *Society of Photo-Optical Instrumentation Engineers (SPIE) Conference Series*, *Presented at the Society of Photo-Optical Instrumentation Engineers (SPIE) Conference*, vol. 2812, edited by E. R. Washwell, pp. 299–308.

Soraas, F., J. A. Lundblad, N. F. Maltseva, V. Troitskaia, and V. Selivanov (1980), A comparison between simultaneous I.P.D.P. groundbased observations and observations of energetic protons obtained by satellites, *Planet. Space Sci.*, *28*, 387–405, doi:10.1016/0032-0633(80)90043-4.

Southwood, D. J., and M. G. Kivelson (1981), Charged particle behavior in low-frequency geomagnetic pulsations. I Transverse waves, *J. Geophys. Res.*, *86*, 5643–5655, doi:10.1029/JA086iA07p05643.

Summers, D., and R. M. Thorne (2003), Relativistic electron pitch-angle scattering by electromagnetic ion cyclotron waves during geomagnetic storms, *Journal of Geophysical Research (Space Physics)*, *108*, 1143–+, doi:10.1029/2002JA009489.

Summers, D., R. Thorne, and F. Xiao (1998), Relativistic theory of wave-particle

resonant diffusion with application to electron acceleration in the magneto-sphere, *J. Geophys. Res.*, *103*(A9), 20,487.

Tsyganenko, N. A. (1996), Effects of the solar wind conditions in the global magnetospheric configurations as deduced from data-based field models, in *International Conference on Substorms*, *ESA Special Publication*, vol. 389, edited by E. J. Rolfe & B. Kaldeich, p. 181.

Usanova, M. E., I. R. Mann, I. J. Rae, Z. C. Kale, V. Angelopoulos, J. W. Bonnell, K. Glassmeier, H. U. Auster, and H. J. Singer (2008), Multipoint observations of magnetospheric compression-related EMIC Pc1 waves by THEMIS and CARISMA, *Geophys. Res. Lett.*, *35*, 17, doi:10.1029/2008GL034458.

Usanova, M. E., et al. (2010), Conjugate ground and multisatellite observations of compression-related EMIC Pc1 waves and associated proton precipitation, *J. Geophys. Res.*, *115*, 7208, doi:10.1029/2009JA014935.

Waters, C. L., J. C. Samson, and E. F. Donovan (1996), Variation of plasmatrough density derived from magnetospheric field line resonances, *J. Geophys. Res.*, *101*, 24,737–24,746, doi:10.1029/96JA01083.

Wright, D. M., and T. K. Yeoman (1999), High resolution bistatic HF radar observations of ULF waves in artificially generated backscatter, *Geophys. Res. Lett.*, *26*, 2825–2828, doi:10.1029/1999GL900606.

Yahnin, A., and T. Yahnina (2007), Energetic proton precipitation related to ion cyclotron waves, *Journal of Atmospheric and Solar-Terrestrial Physics*, *69*, 1690–1706, doi:10.1016/j.jastp.2007.02.010.

Yahnin, A., T. Yahnina, A. Demekhov, J. Manninen, J. Kultima, and J. Kangas (2004), Multiple sources as a possible cause of multiband spectra of Pc1 geomagnetic pulsations, *Geomagnetism and Aeronomy*, *44*, 288291.

Zolotukhina, N., V. Pilipenko, M. Engebretson, and A. Rodger (2007), Response of the inner and outer magnetosphere to solar wind density fluctuations during the recovery phase of a moderate magnetic storm, *Journal of Atmospheric and Solar-Terrestrial Physics*, *69*, 1707–1722, doi:10.1016/j.jastp.2007.02.011.

Chapter 3

Test Particle Simulations of Ion Dynamics in the Inner Magnetosphere

In this chapter physical mechanisms leading to the formation of anisotropic ion distributions with $T_\perp > T_\parallel$ necessary for EMIC wave generation will be considered. For this, motion of an ensemble of ring current protons trapped in the Earth's magnetic field is simulated using a test-particle approach. In this approach, the particle's distribution function is approximated by a finite number of test-particles that are independent of each other and immersed in the external magnetic field, while the fields produced by the particles in the course of their motion are neglected.

3.1 Distribution Function

Each particle is fully described by its position in a 6-D phase space defined by the three spatial coordinates $\mathbf{r} = \{r_1, r_2, r_3\}$ and the three generalized momenta $\mathbf{p} = \{p_1, p_2, p_3\}$. Each particle is related to the point in phase space $\mathbf{R} = \{\mathbf{r}, \mathbf{p}\}$. The phase space density (PSD), also called the particle's distribution function $f(\mathbf{r}, \mathbf{p}, t)$ enables the calculation of bulk properties of the distribution. For example, the particle density is given by the zero-order velocity moment of the distribution:

$$n(\mathbf{r}, t) = \int f(\mathbf{r}, \mathbf{p}, t) d^3\mathbf{p}. \tag{3.1}$$

3.2 Differential Particle Flux

The distribution function cannot be measured directly in experiments, however, it can be related to the observed quantity. The distribution function in Cartesian coordinates can be expressed as

$$f(\mathbf{r}, \mathbf{p}, t) = \frac{dN}{dx\,dy\,dz\,dp_x\,dp_y\,dp_z}, \tag{3.2}$$

where N represents the total number of particles of a given type in volume V.

If the z-axis of the chosen coordinate system is oriented along the particle velocity vector $\mathbf{v}$, as shown in Figure 3.1, the area element perpendicular to $\mathbf{v}$ is given by $dA = dx\,dy$. Then, $dz = v\,dt$, and $dp_x\,dp_y\,dp_z = p\,dp\sin\theta\,d\theta\,d\phi = p^2\,dp\,d\Omega$, where $d\Omega$ is an element of solid angle. Considering only those particles with energy between E and $E + dE$ and using $v\,dp = dE$, the phase space density can
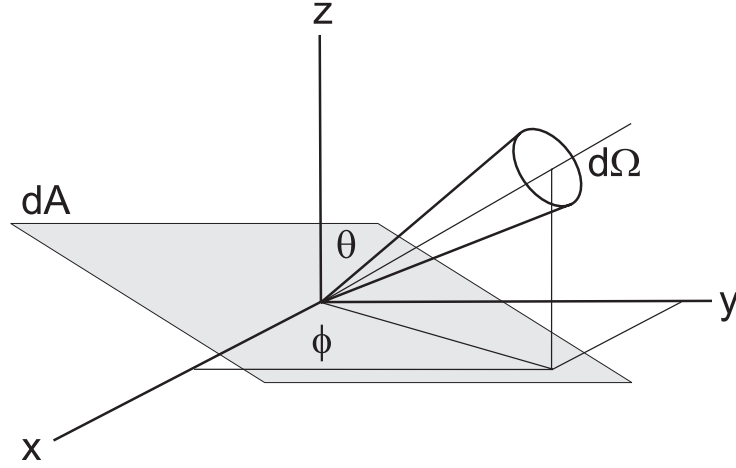
Figure 3.1: Definition of the differential flux. Adapted from (*Parks*, 2004).

be expressed in terms of the new variables as

$$f(\mathbf{r}, \mathbf{p}, t) = \frac{dN}{p^2 dA d\Omega dt dE}. \tag{3.3}$$

The quantity $dN(dA d\Omega dt dE)^{-1}$ is the differential flux $j(E, \mathbf{\Omega}, \mathbf{r}, t)$ measured by a particle detector in units of $(\text{cm}^2 \cdot \text{ster} \cdot \text{s} \cdot \text{MeV})^{-1}$ or $(\text{cm}^2 \cdot \text{ster} \cdot \text{s} \cdot \text{keV})^{-1}$. Therefore, the phase space density can be defined from the differential flux measurements using

$$f(\mathbf{r}, \mathbf{p}, t) = \frac{j(E, \mathbf{\Omega}, \mathbf{r}, t)}{p^2}. \tag{3.4}$$

Since the differential flux depends on the direction $\mathbf{\Omega}$, it can be also interpreted as the angular distribution of particles. However, often due to limitations in the angular resolution of particle detectors, the omnidirectional differential flux is often measured. The omnidirectional flux can be obtained by integration

of the differential flux over the solid angle $d\Omega$:

$$j_{omni}(E, \mathbf{r}, t) = \frac{1}{4\pi} \int j(E, \mathbf{\Omega}, \mathbf{r}, t) d\mathbf{\Omega}. \tag{3.5}$$

Another quantity, which is often used in space physics, is the integral omni-directional flux $J(E, \mathbf{r}, t)$. The integral omnidirectional flux $J(E, \mathbf{r}, t)$ gives the flux of all particles with energies above the threshold E:

$$J(E, \mathbf{r}, t) = \frac{1}{4\pi} \int \int_E^\infty j(E, \mathbf{\Omega}, \mathbf{r}, t) dE d\mathbf{\Omega}. \tag{3.6}$$

3.3 The NASA AP8 Model

In this thesis, for the purpose of our modelling, an initial distribution function is calculated using the AP8 model (*Vette*, 1992). AP8 is an empirical model that describes the differential or integral omnidirectional flux of protons between $E = 0.1 - 400$ MeV and $L = 1.1 - 6.6$ for two epochs representing solar maximum (1970) and minimum (1964) conditions. For each epoch, the model consists of a three-dimensional table of (logarithm of) proton flux in energy, L-value, and B/B_0 (magnetic field strength normalized to the equatorial field strength) based on data from more than 20 satellites. The code provided along with the AP8 flux tables, computes the proton flux for a given energy, L-value and B/B_0 by interpolating in energy and in $(L, B/B_0)$ space and is available at

ftp://hanna.ccmc.gsfc.nasa.gov/pub/modelweb/radiation_belt.

Figure 3.2 shows the equatorial AP8 differential flux (left panel) and the AP8 differential flux divided by energy which multiplied by the proton mass will
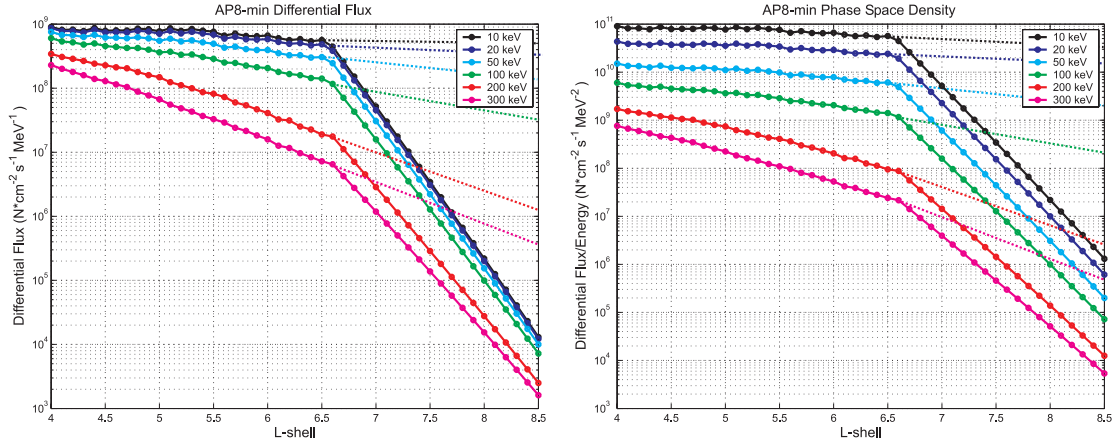
Figure 3.2: Equatorial AP8 solar minimum differential flux (left panel) and phase space density divided by m_p (right panel) for protons with energies 10 keV (black), 20 keV (blue), 50 keV (cyan), 100 keV (green), 200 keV (red), and 300 keV (magenta). The dashed lines show AP8 flux and PSD extrapolated to beyond $L > 6.6$ based on the function slopes for $L < 6.6$ (see discussion in text).

give a value of phase space density (right panel) for protons with energies between $10 - 300$ keV as a function of L. As follows from the figure, the proton differential flux and the phase space density are maximum for lower energies.

Figure 3.3 shows the equatorial AP8 (solar minimum) differential flux as a function of energy computed for multiple L-shells. It illustrates the fact that the phase space density has the maximal values at lower L-shells. Therefore, the least energetic particles at lower L-shells have the highest PSD.

The AP8 model has the following limitations:

- the model is valid only below $L = 6.6$;

- the model does not include flux measurements for protons with $E < 100$ keV and the lower energy flux has to be extrapolated from higher energy flux;

- the flux is omnidirectional, therefore, all information about the particle
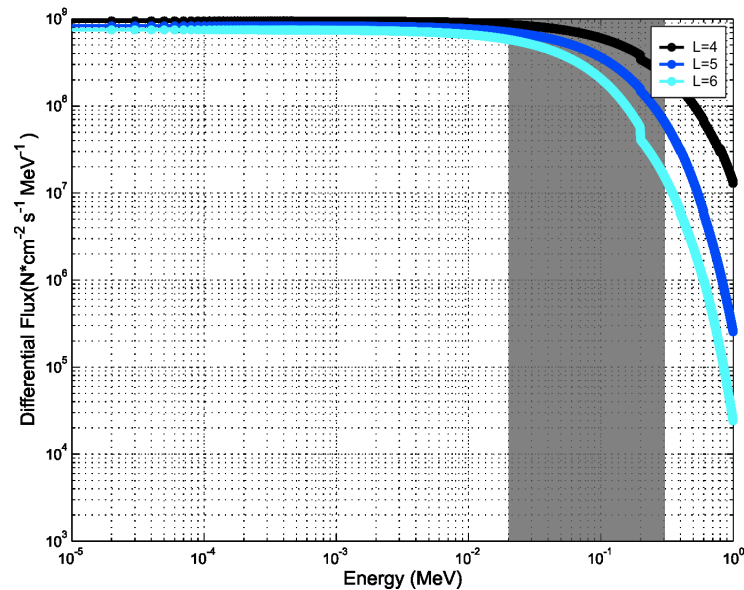
Figure 3.3: Equatorial AP8 differential flux as a function of energy computed for $L = 4 - 6$ and solar minimum conditions. The shaded bar shows the energy range for protons used in the particle tracing. The colour coding: $L = 4$ (black), $L = 5$ (blue), $L = 6$ (cyan).

pitch-angle distribution is lost;

- large errors may occur in the regions where steep gradients of plasma density exist and where the flux time variations are not well understood. The AP8 model generally under-estimates proton fluxes by a factor of two (*Cabrera et al.*, 2005);

- an even larger error must be considered for differential fluxes (in angle or energy) computed from the omnidirectional integral flux tables.

Despite its limitations, the AP8 is the only model predicting the energetic proton fluxes in the magnetosphere reaching as far as geosynchronous orbit. At $L = 6.6$ the AP8 flux experiences a rapid decrease resulting in the stronger negative PSD slope (see Figure 3.2). Since the goal of this thesis is to examine

the formation of anisotropic particle distributions at $L \approx 5 - 7$ (the L-range supported by the observations, where initialization of PSD is required), the differential flux and phase space density were extrapolated to beyond $L > 6.6$ based on the function slopes for $L < 6.6$ (the extrapolated differential flux and PSD values are shown in Figure 3.2 by the dashed lines). However, to study the effects of strong negative gradients in PSD on the formation of temperature anisotropies, we will use the original AP8 flux profiles in our computations, too. Note that other similar models are less suitable for the purpose of this thesis as they describe the proton flux behaviour at even lower L-shells. For example, analogous to AP8, the CRRESPRO proton flux model is valid only up to $L = 5.5$ (*Gussenhoven et al.*, 1994).

3.4   Liouville's Theorem and Backward Particle Tracing

In collisionless space plasmas, the dynamic evolution of the particle distribution function is described by the Vlasov equation:

$$\frac{\partial f}{\partial t} + \frac{\mathbf{p}}{m} \cdot \frac{\partial f}{\partial \mathbf{r}} + q \left[\mathbf{E} + \frac{\mathbf{p}}{m} \times \mathbf{B} \right] \cdot \frac{\partial f}{\partial \mathbf{p}} = 0, \qquad (3.7)$$

where $\mathbf{E}$ and $\mathbf{B}$ are the mean electric and magnetic fields, q is the particle charge and m is its mass. The Vlasov equation is a particular case of a more general expression known as Liouville's theorem which states that in the absence of energy dissipation (or input) and collisions phase space density is constant along a particle trajectory. This theorem is a powerful tool for studying the evolu-

tion of the distribution function $f(\mathbf{r}, \mathbf{p}, t)$ and it also gives us the possibility to reconstruct particle distributions at positions where they cannot be measured.

To understand the mechanisms leading to EMIC wave generation in a compressed magnetosphere, we want to determine how the distribution function for an ensemble of ring current protons evolves in time and space as the particles drift from the nightside to the dayside. We assume the initial distribution function to be known in the midnight magnetosphere. The most intuitive way to address this problem would be to trace the trajectory of each particle from the nightside to the dayside magnetosphere. However, particles for a single fixed location but with different initial velocities will end up at different positions. Therefore, in order to compute the distribution function at any particular point in coordinate space, one would have to perform an interpolation, which would introduce interpolation errors and would also require a large number of particles. Instead of tracing particle trajectories forwards in time we will trace them backwards in time from the position where the distribution function has to be computed (see Figure 3.4). This method is called the backward Liouville tracing (see, e.g., *Marchand*, 2010). The advantage of this method is that it does not introduce any statistical (interpolation) errors and requires a relatively small number (a few thousands) of particles.
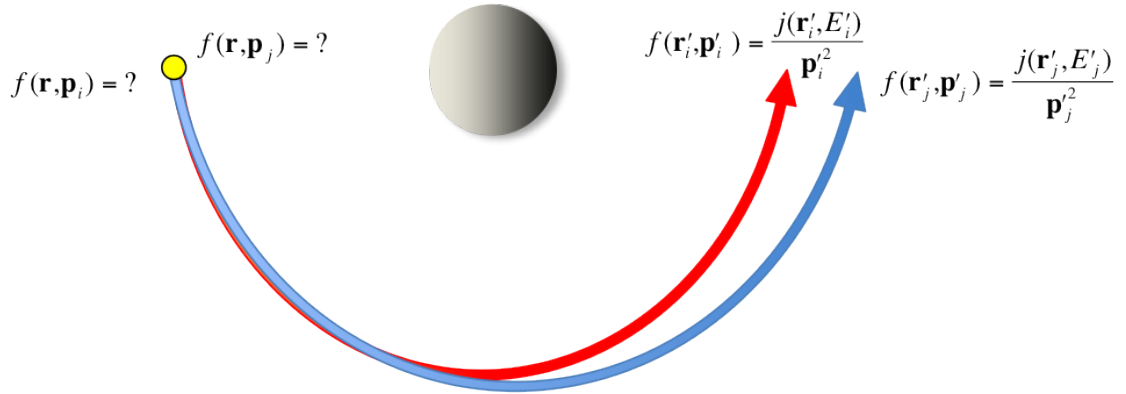
Figure 3.4: Schematic illustration of the backward tracing approach. The distribution function is to be computed at the position shown by the yellow circle. The distribution function is defined in the nightside equatorial magnetosphere. The red and the blue curves show drift trajectories of two particles launched from the same starting point with different initial velocities.

3.5 Integration of Particle Trajectories

The non-relativistic equation of motion of an individual particle in the external electric and magnetic fields takes the form

$$m\frac{d\mathbf{v}}{dt} = q(\mathbf{E} + \mathbf{v} \times \mathbf{B}). \tag{3.8}$$

In order to find the particle position, the equation of motion has to be completed by

$$\frac{d\mathbf{r}}{dt} = \mathbf{v}. \tag{3.9}$$

This system of equations is integrated using the leapfrog method (see, e.g., *Birdsall and Langdon*, 1985). In leapfrog schemes, the velocity, $\mathbf{v}$, is defined at integer time steps and the coordinate, $\mathbf{r}$, at the mid-points, as illustrated in Figure 3.5. Then the equations of motion 3.8 and 3.9 take the following finite-difference

form:

$$\frac{\mathbf{v^{i+1}} - \mathbf{v^i}}{\Delta t} = \frac{q}{m}(\mathbf{E^i} + \frac{\mathbf{v^{i+1}} + \mathbf{v^i}}{2} \times \mathbf{B^i}), \tag{3.10}$$

$$\frac{\mathbf{r^{i+3/2}} - \mathbf{r^{i+1/2}}}{\Delta t} = \mathbf{v^{i+1}}, \tag{3.11}$$

where **E** and **B** are the external electric and magnetic fields, and **i** is the time step number.

To switch from a forward to a backward particle trajectory integration, the signs of the magnetic field and the time increment should be changed to the opposite.
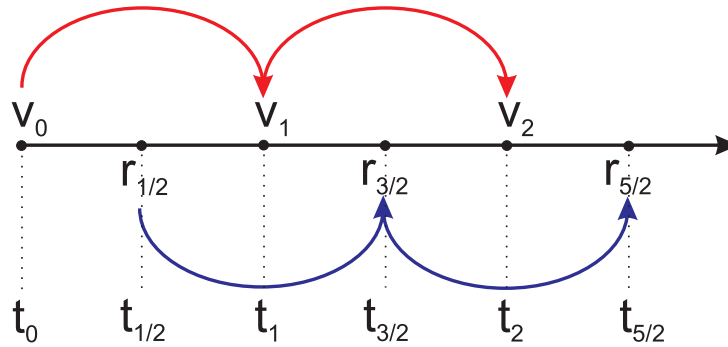
Figure 3.5: The leapfrog time-stepping.

The leapfrog integrator is exactly time reversible because of the symmetric way in which it is defined, and the time reversibility gives this method some very important advantages. It guarantees conservation of energy and angular momentum, which is important for the preservation of phase space density. It is often used for simulations of dynamics of oscillatory systems, where it is important to resolve long-term small changes in the properties of a nearly periodic orbit and where the systematic numerical errors must be minimized. Given the characteristic gyromotion of particles in our problem, it is well-suited for our

needs.

According to *Birdsall and Langdon* (1985), there is no amplitude error in energy associated with this method for $\omega \delta t \leqslant 2$, where ω is a characteristic oscillation frequency (here, the gyrofrequency). However, the method introduces a phase error. These authors estimated the phase error accumulated after N_{steps} steps to be $\sigma_\phi = \frac{1}{24} N_{steps} (\omega \delta t)^3$. This formula gives a phase error estimate of $\sigma_\phi < 1.5$ rad for our simulations. This error is not critical here, however it may become important when the exact ratio between two individual perpendicular (to the background magnetic field) velocity components has to be defined.

3.6 Magnetic Field Model

This section discusses the magnetic field model that gives a simple analytic description for a dipole magnetic field deformed by interaction with the solar wind. We have neglected the magnetospheric convection electric field assuming that it is small during undisturbed geomagnetic conditions. This assumption has also been adopted by *McCollough et al.* (2010). *McCollough et al.* (2010) have performed global MHD simulations for the event of June 29, 2007 and have shown that the effects of convection electric field on the particle dynamics during this event are minor. Therefore, the integration of particle trajectories presented here was performed only in the presence of a compressed magnetic field with the convection electric field neglected.

The analytic magnetic field model used for this work is described in *Mead* (1964). It results from a superposition of the Earth's dipole magnetic field and the magnetic field produced by the magnetopause current due to interaction of

the geomagnetic field and the solar wind. This model does not account for the fields created by the ring current and ionospheric currents (which are included in more advanced semiempirical magnetic field models like, for example, T96 (*Tsyganenko*, 1996) mentioned in the previous chapter). We have intentionally selected such a simple model to enable a parameterized study of the effect of magnetospheric compression on particle dynamics. The B_x, B_y, and B_z components of the magnetic field are given by the equations:

$$B_x = -\frac{3Mxz}{r^5} + \frac{\sqrt{3}g_2z}{b^4}, \tag{3.12}$$

$$B_y = -\frac{3Myz}{r^5}, \tag{3.13}$$

$$B_z = -\frac{M(3z^2 - r^2)}{r^5} - \frac{g_1}{b^3} + \frac{\sqrt{3}g_2x}{b^4}, \tag{3.14}$$

where $M = 8.02 \cdot 10^{22}$ Am^2 is the Earth's dipole moment, b is a subsolar standoff distance of the magnetopause measured in R$_e$, $g_1b^3 = -0.2515 \times 10^{-4}$ T, and $g_2b^4 = 0.1215 \times 10^{-4}$ T. Numerical values for g_1 and g_2 were obtained by *Mead and Beard* (1964).

Kivelson and Russell (1995) derived the following semi-empirical formula relating the magnetopause subsolar standoff distance b in units of R$_e$ and the solar wind proton number density, n_{sw} and velocity, v_{sw}:

$$b = 107.4(n_{sw}v_{sw}^2)^{-\frac{1}{6}}, \tag{3.15}$$

where n_{sw} is defined in cm^{-3} and v_{sw} is in km/s.

For the EMIC wave event from June 29, 2007 (see Chapter 2, Section 2.1), the magnetopause subsolar standoff distance estimated from Equation 3.15, ranges
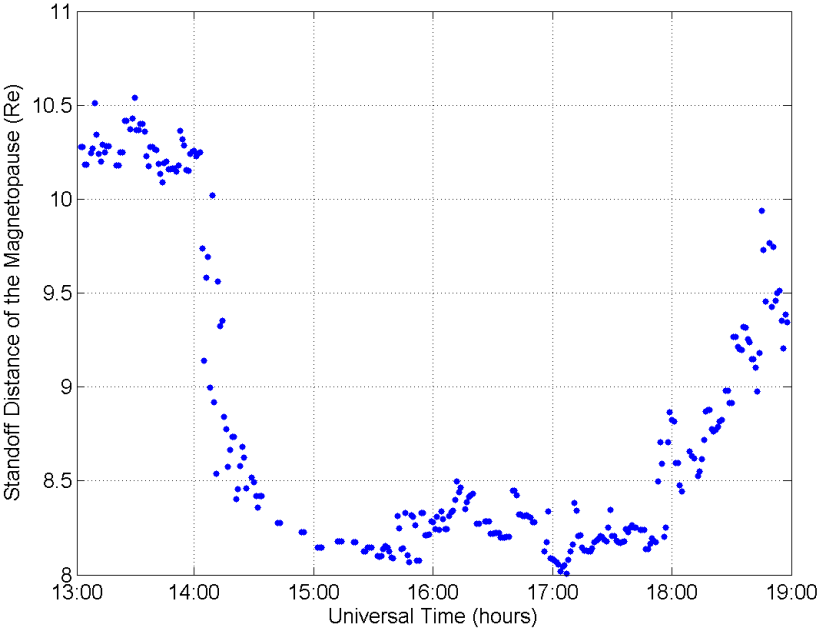
Figure 3.6: Magnetopause subsolar standoff distance during the compression event of June 29, 2007.
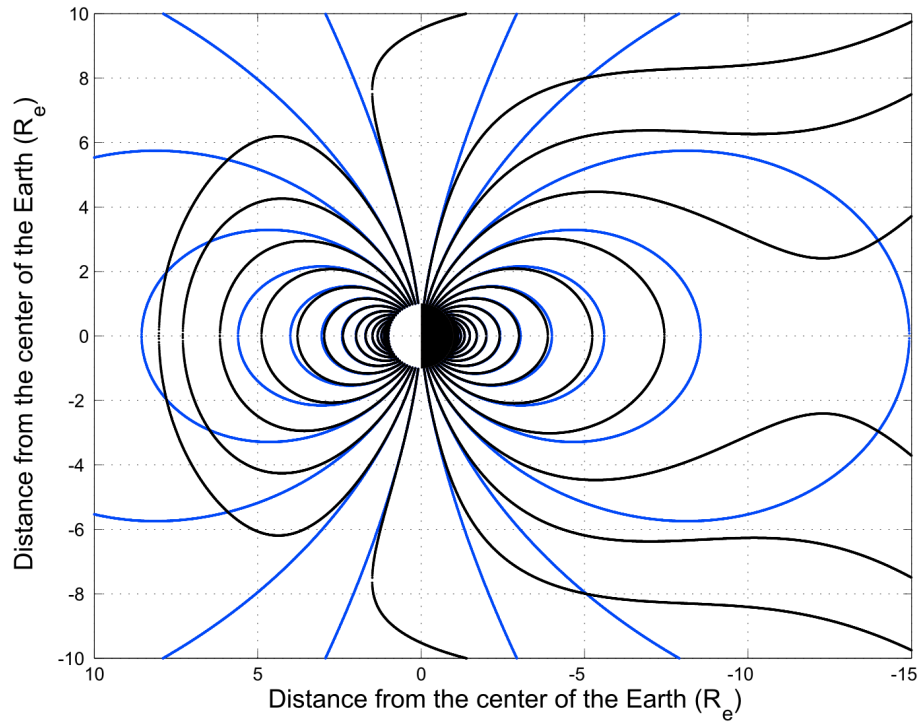
Figure 3.7: Magnetic field lines obtained by the 4th order Runge-Kutta integration of the analytic magnetic field from Equations 3.12 - 3.14 for $b = 8$ (black curves) and for the dipole magnetic field (blue curves). The positive x-direction points towards the Sun and z is along the magnetic dipole axis. Dipole tilt is neglected.
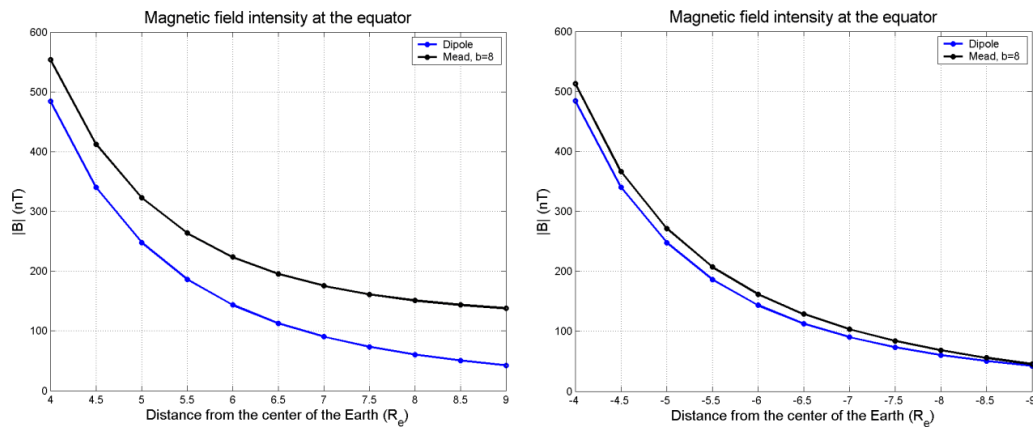
Figure 3.8: Magnetic field strength along the subsolar equatorial line for the dipole (blue line) and for the Mead field model for $b = 8$ (black line) at noon (left panel) and midnight (right panel) meridian.

between 8 and 10.5 R$_e$, as shown in Figure 3.6. This range of the standoff distance values are used in the test-particle simulations. The magnetic field lines computed from Equations 3.12 - 3.14 by the 4th order Runge-Kutta method for $b = 8$ are shown in Figure 3.7. Compared to the dipole field, the Mead magnetic field is compressed at noon and at midnight. Figure 3.8 shows the radial profile of the magnetic field strength at the magnetic equator between $L = 4 - 9$ for the dayside (left panel) and for the nightside (right panel).

3.7 Calculation of the Distribution Function
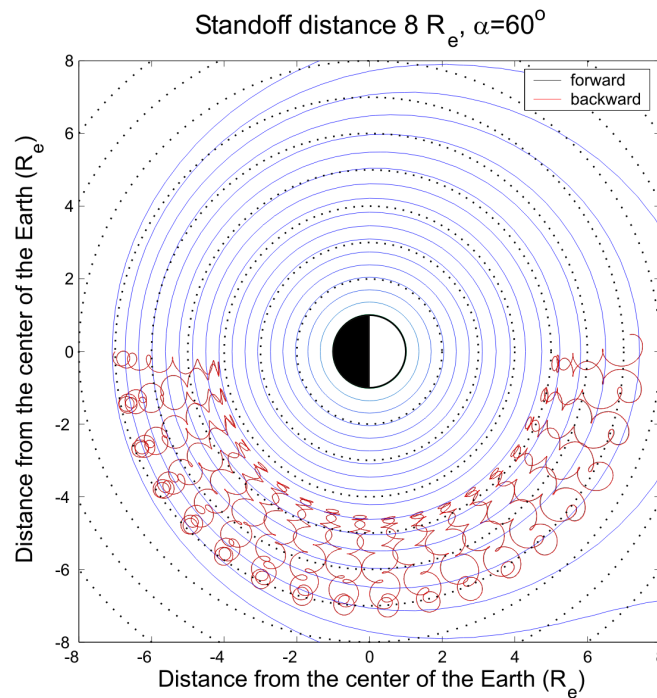
Figure 3.9: Forward and backward (right underneath the forward) trajectories of a $60°$ pitch-angle particle superposed over the contours of constant magnetic field (in blue colour). The dotted lines are equally spaced every 1 R$_e$. Similar results were obtained for particles with different pitch angles and for multiple levels of compression.

Figure 3.9 shows the trajectory of a particle with an initial pitch angle $\alpha = 60°$ launched in the external magnetic field (described in the next section) from the nightside magnetosphere and drifting around the Earth towards the dayside. The trajectory for the same particle launched backwards in time is also shown. The forward and the backward trajectories are the same on the scale of the figure, as shown by the red curve.

The leapfrog integrator was also tested against the Runge-Kutta integrator (provided by Konstantin Kabin, University of Alberta) which is 5th-order accurate but is not fully reversible. With the proper time step, the forward particle trajectories computed by both of these methods are in pretty good agreement.

Multiple particle tracing was then performed in order to construct distribution functions for protons with energies between $20 - 200$ keV grouped into eight energy bins. The initial velocity grid was chosen to be uniform in spherical coordinates and spaced every $10°$ producing the isotropic initial pitch-angle distribution shown in Figure 3.10. The total number of particles used in the simulations was $36 \times 19 \times 8 = 5472$. To expedite computations, the particle trajectories were integrated on a shared memory machine with multiple cores using OpenMP parallel architecture.

This ensemble of particles was launched backwards in time from the equatorial magnetic plane in the noon meridian where the distribution function has to be constructed to the equatorial midnight where it is known. The tracing of each particle trajectory was stopped once the particle crossed the equatorial magnetosphere ($z = 0$) in the nearest vicinity (within one bounce period) of the midnight plane (this offset in the final particle's position from the y-axis does not introduce noticeable errors). Note that as all the particles perform a bounce
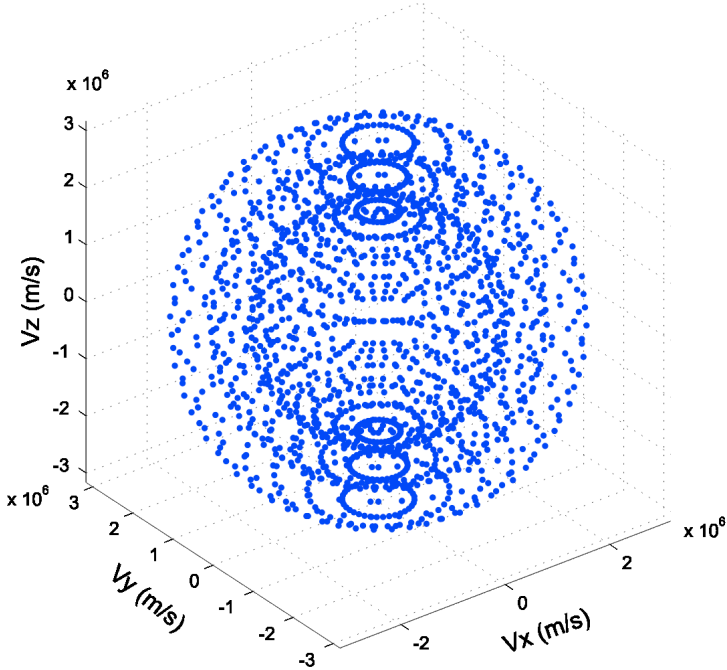
Figure 3.10: The initial velocity grid for the three lowest energy levels. The points in velocity space are evenly distributed every 10° and produce a uniform pitch-angle distribution.

motion during their azimuthal drift, they do not necessarily cross the magnetic equator ($z = 0$) at $y = 0$.

The distribution function in the nightside equatorial magnetosphere was initialized based on the AP8 model using the integral unidirectional flux J_{AP8}:

$$f(\mathbf{r}, \mathbf{p}) = \frac{1}{p^2} \cdot \frac{J_{AP8}(E + \Delta E, \mathbf{r}) - J_{AP8}(E, \mathbf{r})}{\Delta E}. \tag{3.16}$$

As we do not have angular distribution measurements from the nightside magnetosphere for the event of June 29, 2007, we have to initialize pitch angle distributions based on earlier observations. *De Benedetti et al.* (2005) analyzed proton pitch angle distribution from three years of AMPTE/CCE/CHEM proton data between $L = 3 - 9$ and found that nightside pitch angle distributions of protons with energies $E > 10$ keV are nearly isotropic (when protons are newly injected in the nightside) at $L > 5.5$ and anisotropic (peaked at $90°$ pitch angles) at $L < 5.5$. The latter is formed for particles on closed trajectories during quiet geomagnetic periods and is typical for all MLT sectors. *Zhang et al.* (2006) performed a statistical study of pitch angle distributions of ions with energies between $1 - 30$ keV at geosynchronous orbit (measured by the Los Alamos Magnetospheric Plasma Analyzer instrument) during magnetic storms and found that at times preceding the magnetic storm the nightside pitch angle distributions have temperature anisotropies $A \approx 1 - 1.2$. *Garcia and Spjeldvik* (1985) analyzed ion distributions with energy in the range between 20 keV and several MeV based on data from the Explorer 45 and ISEE 1 spacecraft. These authors approximated the observed angular distributions as

$$j = j_{||} + j_{\perp} sin^n(\alpha), \tag{3.17}$$

where n is anisotropy index, α is equatorial pitch angle, j is the total flux, $j_{\parallel}$ and $j_{\perp}$ are the fluxes parallel and perpendicular to the background magnetic field, respectively. *Garcia and Spjeldvik* (1985) found that nightside pitch angle distributions of protons with $E \approx 10 - 200$ keV have anisotropy index $n \leqslant 2$ between $L = 4 - 8$. Hence, to simulate evolution of temperature anisotropy during the azimuthal drift from the nightside to the dayside, we consider two types of initial pitch angle distributions. In the first case the initial distribution function was assumed to be isotropic in pitch angle, as shown in Figure 3.11 (left). In the second case the initial distribution function was assigned to be anisotropic, multiplied by a factor of $\sin^2(\alpha)$. Figure 3.11 (right) shows a 2D contour plot of the anisotropic PSD.
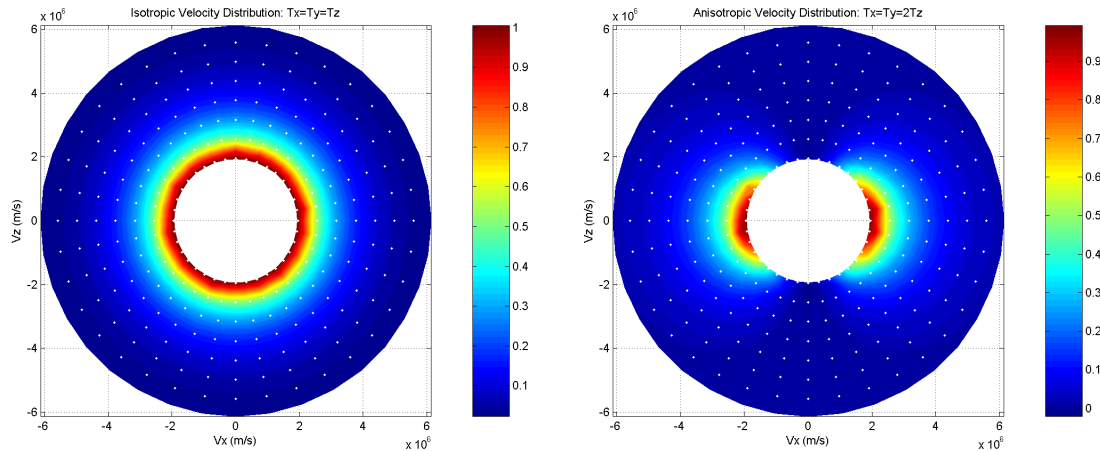
Figure 3.11: A 2D contour plot of the isotropic (left) and anisotropic $\sin^2(\alpha)$ (right) PSD. The white dots superposed over the contour plots indicate computational grid in velocity space. The contour plot was produced in MATLAB using the "contourf" function.

3.8 Simulation Results

Figure 3.12 shows the shape of PSD at the subsolar location at $L = 7$ for the protons which completed a half-orbit around the Earth from the night side magnetosphere for the case when the magnetosphere was strongly compressed ($b = 8$). The distribution function in the left panel of Figure 3.12 was initialized in the midnight meridian being isotropic in pitch angle. In contrast, the right panel of Figure 3.12 shows the final velocity distribution that was anisotropic $\sin^2(\alpha)$ distribution in the midnight meridian. These two panels illustrate the fact that in the course of the azimuthal drift from the nightside to the dayside in the compressed magnetic field, initially isotropic velocity distribution become anisotropic and initially anisotropic distribution increased its anisotropy and perpendicular temperature.
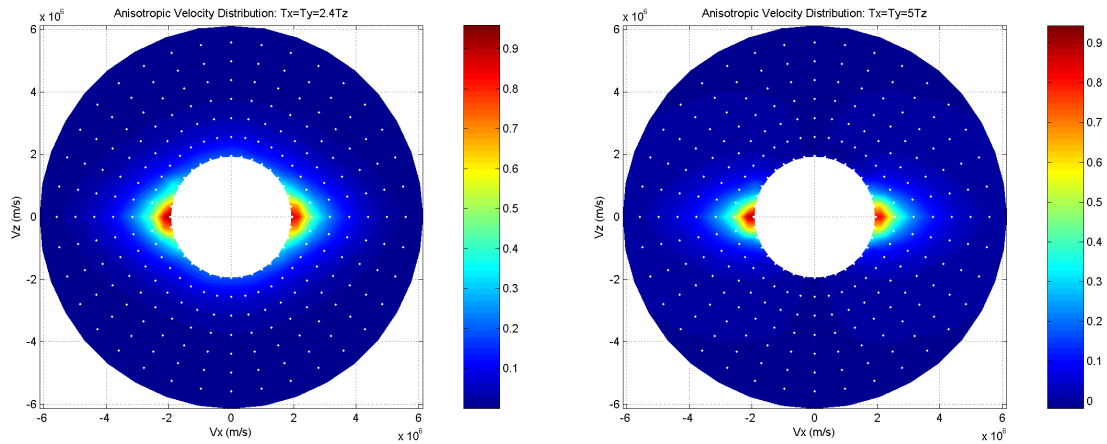
Figure 3.12: Anisotropic PSD formed in the subsolar equatorial noon magnetosphere at $L = 7$. The distributions were generated from an initially isotropic (left) and anisotropic $\sin^2(\alpha)$ (right) velocity distribution in the midnight meridian.

In addition to the 2D contour plots, the 1D anisotropic pitch angle distribution as a function of pitch angle for particles with energy $E = 20$ keV at $L = 7$

for $b = 8$ is shown in Figure 3.13. This pitch angle distribution has evolved from uniform initial pitch-angle distribution in the midnight meridian.
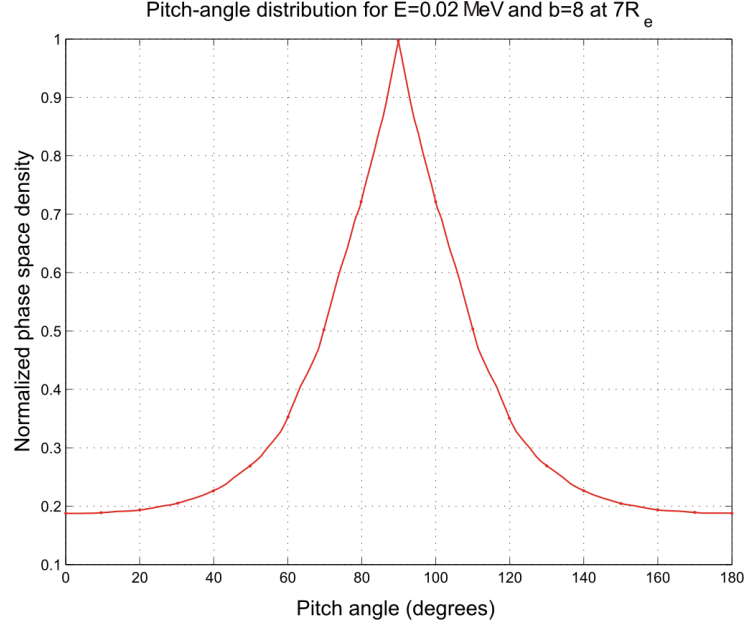
Figure 3.13: Pitch-angle distribution for $E = 20$ keV at $L = 7$ for $b = 8$ in the noon equatorial magnetosphere. The distribution function has evolved from uniform initial pitch-angle distribution in the midnight meridian.

We now compute the temperature anisotropies for the distributions shown above. Assigning a value of distribution function to each particle based on Equation 3.16, it is possible to compute the density and temperatures for the ensemble of particles using

$$n(\mathbf{r}) = \int f(\mathbf{r}, \mathbf{v}) dv_x dv_y dv_z, \tag{3.18}$$

$$T_x(\mathbf{r}) = \frac{m}{3k_B n(\mathbf{r})} \int f(\mathbf{r}, \mathbf{v}) v_x^2 dv_x dv_y dv_z, \tag{3.19}$$

$$T_y(\mathbf{r}) = \frac{m}{3k_B n(\mathbf{r})} \int f(\mathbf{r}, \mathbf{v}) v_y^2 dv_x dv_y dv_z, \tag{3.20}$$

$$T_z(\mathbf{r}) = \frac{m}{3k_B n(\mathbf{r})} \int f(\mathbf{r}, \mathbf{v}) v_z^2 dv_x dv_y dv_z, \tag{3.21}$$

where $m = 1.67 \times 10^{-27}$ kg is the proton mass and $k_B = 1.38 \times 10^{-23} JK^{-1}$ is the Boltzmann's constant.

Since we are interested in the equatorial temperatures, the z-direction represents the direction parallel to the magnetic field, and x and y – the two perpendicular directions. Due to the particle gyration in the xy plane, in the absence of drift and plasma waves that could distort the distribution, the distribution function should be gyrotropic in the xy plane. Therefore, we adopt the following definition to calculate the temperatures (here and in all future computations):

$$T_{\parallel} = T_z, \tag{3.22}$$

$$T_{\perp} = \frac{1}{2}(T_x + T_y), \tag{3.23}$$

$$A = T_{\perp}/T_{\parallel}. \tag{3.24}$$

In addition to nightside pitch-angle distribution ambiguity, the energetic proton flux behaviour beyond $L > 6.6$ is not well known, therefore, we consider two possibilities for energetic proton flux being defined as in the original AP8 flux tables and being extrapolated beyond $L > 6.6$ based on the slope for $L < 6.6$ (see Figure 3.2). This gives us a combination of four different cases which we will analyze below.

Test particles were launched from multiple L-shells in the magnetic equatorial plane. The temperature anisotropy profiles computed as a function of L
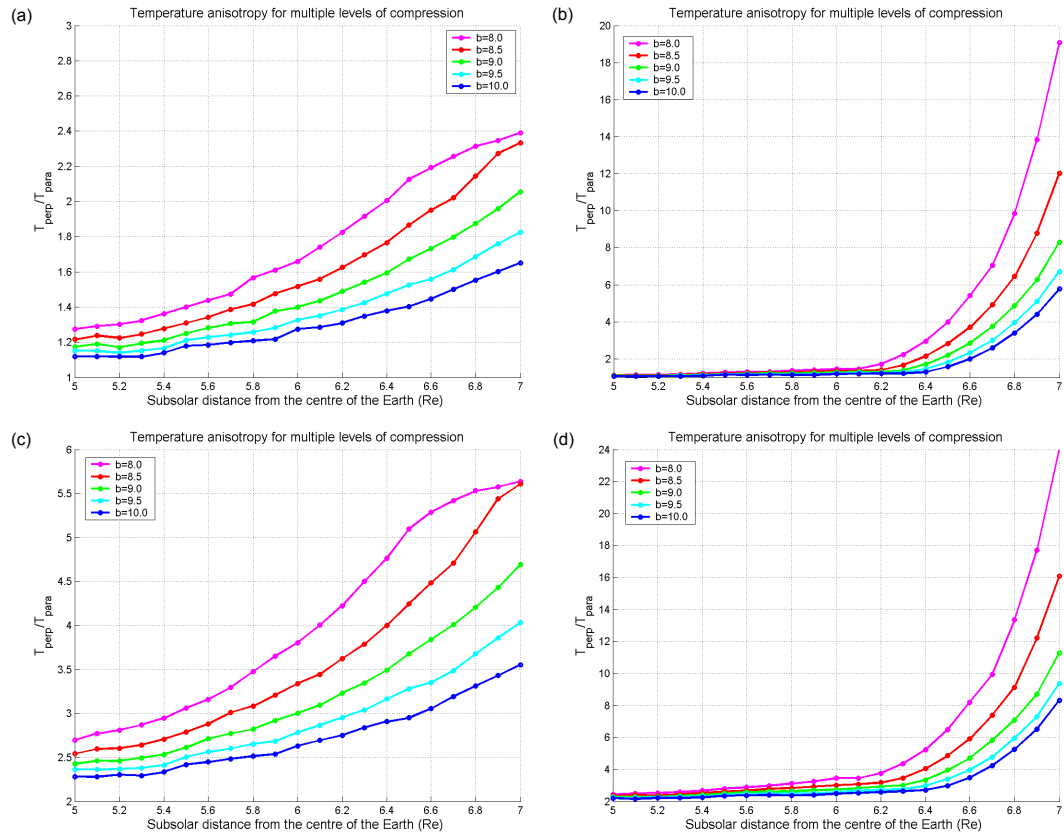
Figure 3.14: Temperature anisotropy profiles at the equatorial noon for the four sets of parameters at the midnight equator: (a) initially isotropic pitch angle distribution for fluxes extrapolated beyond $L = 6.6$; (b) $\sin^2(\alpha)$ pitch angle distribution for fluxes extrapolated beyond $L = 6.6$; (c) initially isotropic pitch angle distribution for original AP8 fluxes; (d) $\sin^2(\alpha)$ pitch angle distribution for original AP8 fluxes. The colours denote different levels of magnetospheric compression in the Mead magnetic field model (see label).

between $L = 5 - 7$ for multiple degrees of magnetospheric compression (as pa-
rameterized by b in the Mead model) are shown in Figure 3.14 (a – d). These
panels demonstrate that the degree of temperature anisotropy increases with L,
as well as with the degree of compression, having a maximum in the subsolar
equator at $L = 7$ (the outward boundary of the simulation domain) for $b = 8$.
Panels (a) and (b) show the temperature anisotropy profiles for initially iso-
topic pitch angle distributions in the midnight equator for fluxes extrapolated
beyond $L = 6.6$ and original AP8 fluxes, respectively. Again, panels (c) and (d)
show the temperature anisotropy profiles for $\sin^2(\alpha)$ pitch angle distributions in
the midnight equator for fluxes extrapolated beyond $L = 6.6$ and original AP8
fluxes, respectively. Note that the steep flux gradient in the original AP8 flux
above geosynchronous orbit leads to much higher degree of temperature aniso-
tropy. This suggests that the degree of temperature anisotropy developed will
be higher if energetic particle flux decreases with L-shell faster than in the AP8
model.

Finally, temperature anisotropies were computed for multiple magnetic local
time (MLT) sectors for $b = 8$. Initial pitch angle distributions were again set in
the midnight equator in the same fashion as for the earlier computations. Con-
tour plots for temperature anisotropy as a function of L and MLT are shown in
Figure 3.15. This figure illustrates that the anisotropy decreases away from the
subsolar point. Nevertheless it remains relatively high along the whole dayside
MLT sector at the outer L-shells.

Dayside observations of ion temperature anisotropy for the range of energies
and L-shells, we used in the simulations show the following. *Zhang et al.* (2006)
observed dayside ion distributions with degree of anisotropy $A \approx 1.3 - 1.7$
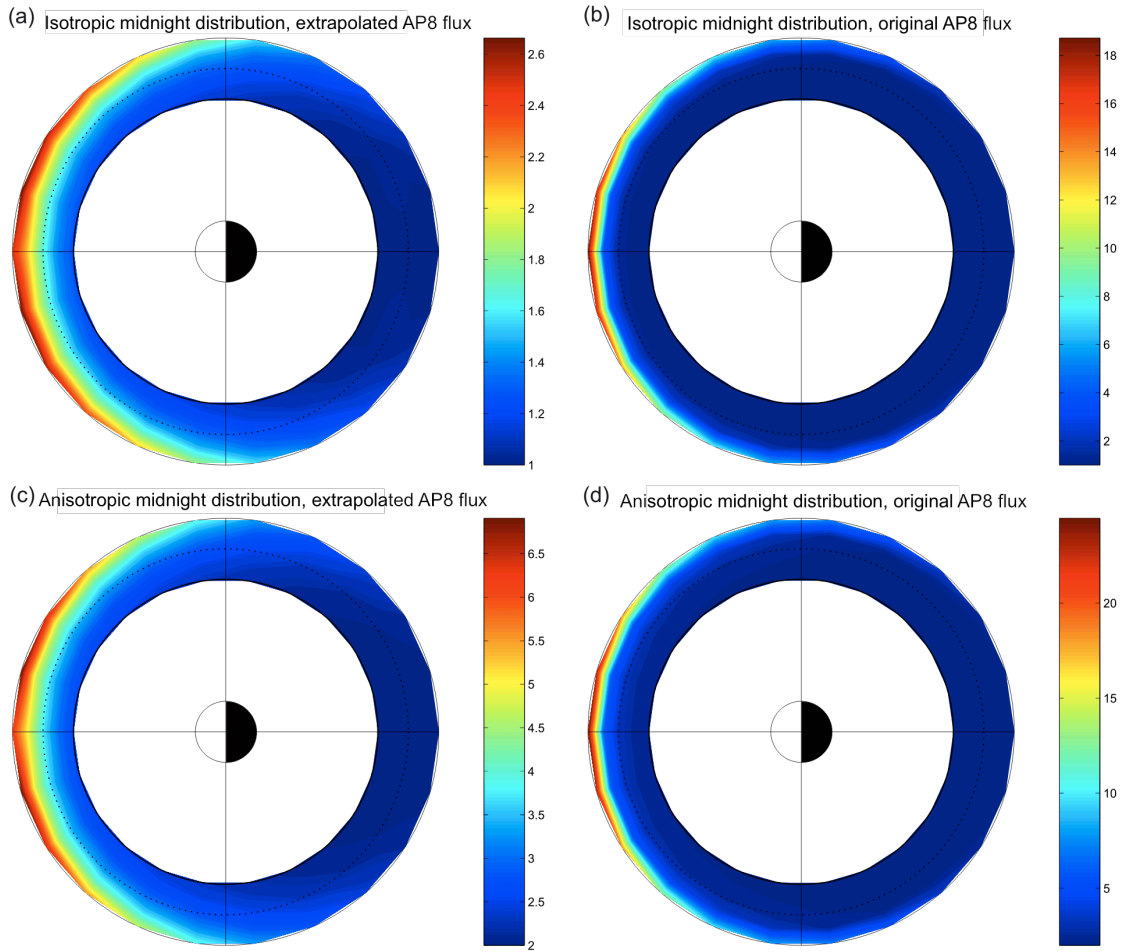
Figure 3.15: Temperature anisotropy contours between $L = 5 - 7$ for $b = 8$ in the equatorial plane for different MLT sectors. (a) isotropic nightside distribution, extrapolated AP8 flux; (b) isotropic nightside distribution, original AP8 flux; (c) $\sin^2(\alpha)$ nightside distribution, extrapolated AP8 flux; (d) $\sin^2(\alpha)$ nightside distribution, original AP8 flux.

at $L = 6.6$, while *Garcia and Spjeldvik* (1985) reported $A \approx 2 - 4$ for $L = 6$. This means that both the isotropic and $\sin^2(\alpha)$ nightside distributions provide dayside anisotropies that are generally consistent with observations. The high anisotropy values that follow from using original AP8 flux profile at $L > 6.6$ are not likely to be realistic since they are not supported by observations. Also, it is important to mention that as soon as the temperature anisotropy exceeds the threshold for EMIC wave excitation, EMIC instability will reduce the anisotropy bringing it back to a marginally stable value. Therefore direct comparison between temperature anisotropies obtained from these simulations and observations can be only done with the help of EMIC instability numerical modelling which we will address in the next chapter.

In the next section, some of the physical mechanisms leading to the development of temperature anisotropy in a compressed magnetosphere will be discussed.

3.9 The Role of Magnetic Field Topology in the Formation of Anisotropic Pitch-angle Distributions

3.9.1 Magnetic Drift Shell Splitting

Generation of anisotropic pitch angle distributions in the magnetosphere due to azimuthal particle drift has been studied by many authors (see, e.g. *Pfitzer et al.*, 1969; *Sibeck et al.*, 1987; *Fritz et al.*, 2003; *McCollough et al.*, 2010). *Sibeck et al.* (1987) have examined mechanisms leading to the formation of anisotropic so-called "butterfly" (with lack of $90°$ pitch-angle particles) and "head-and-shoulders"

(with excess of $90°$ pitch-angle particles, as in Figure 3.13) distributions in the dayside magnetosphere. *Sibeck et al.* (1987) concluded that these distributions are generated due to different drift paths for particles with different pitch-angles bringing particles with different origins together.

While in the symmetric dipole magnetic field all particles drift around the Earth at the same (initial) equatorial distance, in a compressed magnetic field particles with near $90°$ pitch angles follow lines of constant magnetic field (conserving magnetic moment $\mu = mV_\perp^2/B$), and particles with smaller pitch-angles move along more circular orbits. This is known as drift-shell splitting. This situation is illustrated in our model results in Figure 3.16. The figure shows the trajectories of particles launched from the nightside equatorial magnetosphere with $90°$, $75°$, and $60°$ pitch angles, respectively. The $90°$ pitch-angle particles follow contours of constant magnetic field (shown in blue). At the same time, the $60°$ and $75°$ pitch-angle particles drift closer to the dashed circles. The particles start their drift motion at $L = 5$ and $L = 6.5$ (the top and the bottom panels, respectively) in a more ($b = 8$, left panels) and less ($b = 10$, right panels) compressed magnetosphere. The drift trajectory splitting is more prominent for particles at higher L-shells and for the higher degree of compression, for example, as shown in panel (c). For particles orbiting the Earth at lower radial distances, the drift-shell splitting effect is negligible.

In a situation where PSD decreases with radial distance from the Earth as shown in Figure 3.2, the $90°$ pitch-angle particles drifting closer to the Earth (as compared to smaller pitch-angle particles) will have a larger PSD. This leads to the enhancement of the perpendicular temperature with respect to the parallel temperature and makes the distribution anisotropic with $T_\perp > T_\parallel$. However, if

occasionally PSD increases with radial distances from the Earth, the distribution will become anisotropic with $T_{||} > T_{\perp}$.
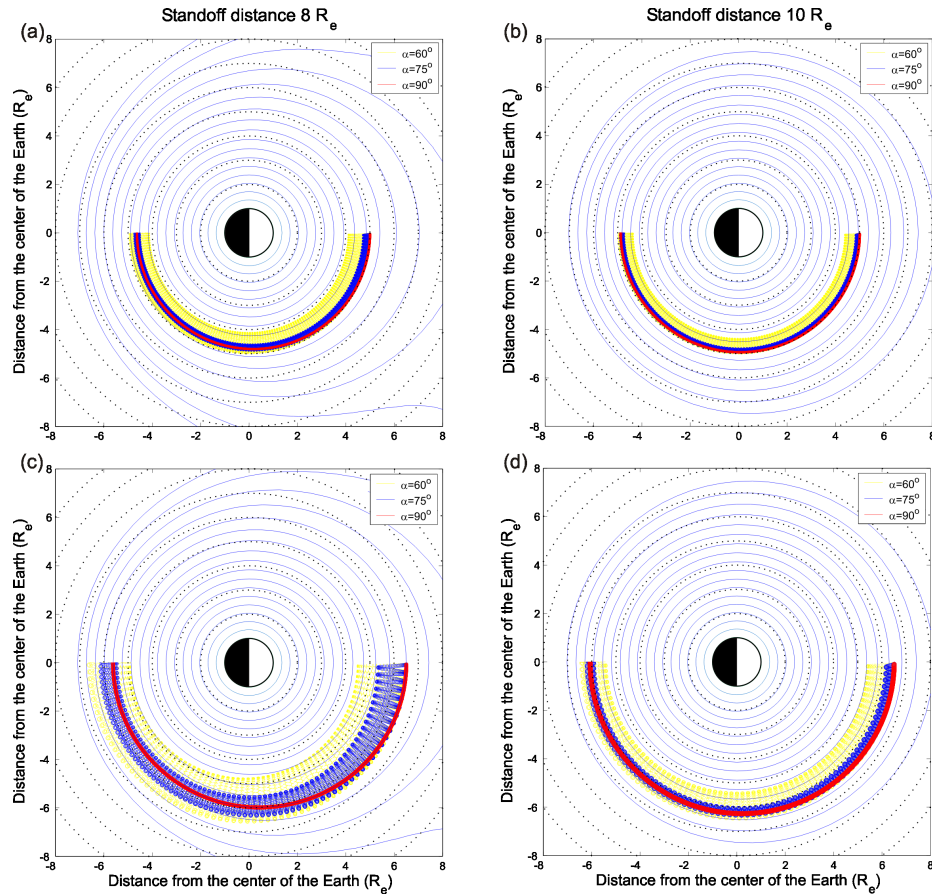
Figure 3.16: Illustration of magnetic drift shell splitting. Trajectories of particles launched from the nightside equatorial magnetosphere with the $90°$ (red curves), $75°$ (blue curves), and $60°$ (yellow curves) pitch angles. The contours of constant magnetic field are shown by the thin blue lines. Panels (a) and (c) show a more compressed magnetosphere ($b = 8$), (b) and (d) a less compressed magnetosphere ($b = 10$).

The magnetic drift shell splitting occurs independent of the particle's mass and energy and depends only on the particle's pitch angle. Therefore, the degree of anisotropy developed by different ion populations (H^+, He^+, O^+) due to the magnetic drift shell splitting in a static magnetic field will be the same. This is
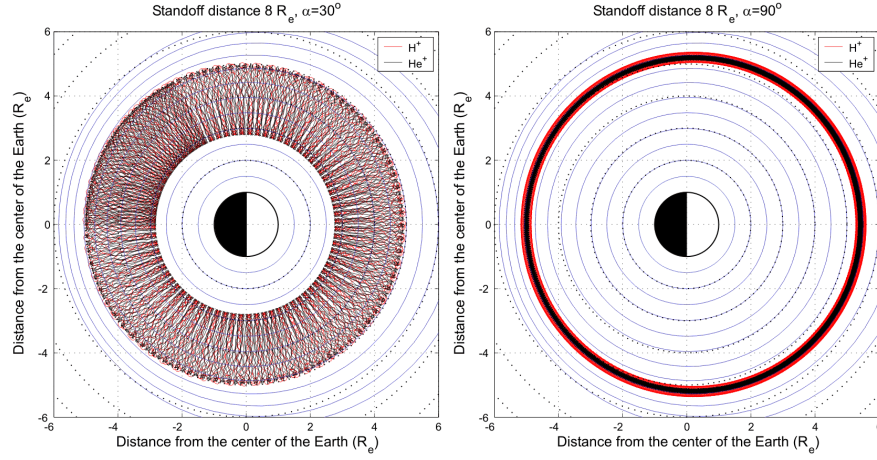
Figure 3.17: Trajectories of H^+ (red curve) and He^+ (black curve) ions with $30°$ (left) and $90°$ (right) pitch angles in a compressed magnetosphere ($b = 8$).

illustrated in Figure 3.17 showing trajectories of H^+ and He^+ ions with the same energy for two different ($30°$ and $90°$) pitch angles.

3.9.2 Shabansky Orbits

Close to the magnetopause, a compressed magnetic field can have B_{min} regions located not in the equatorial plane but off the equator. This was first discovered by *Shabansky* (1971). In such a field topology, particles do not traverse the equatorial plane but rather continue their drift through regions away from equator as shown in Figure 3.18. *Northrop* (1963) derived the equation of motion for the center of gyration (guiding center) of a charged particle in magnetic field:

$$\frac{m}{q}\dot{v}_{||} = \frac{m}{q}g_{||} - \frac{\mu}{q}\frac{\partial B}{\partial s}, \qquad (3.25)$$

where m is the particle mass, q is its charge, $v_{||}$ is its speed parallel to the magnetic field B, μ is its magnetic moment, $g_{||}$ is the gravitational acceleration par-

allel to B, and s is the curvilinear coordinate along the field line. In a dipole field the mirror force $\frac{\mu}{q}\frac{\partial B}{\partial s} > 0$ always acts towards the magnetic equatorial plane and moves particles towards the magnetic equator resulting in a regular bounce motion. In "Shabansky" regions of off-equatorial B_{min}, the mirror force $\frac{\mu}{q}\frac{\partial B}{\partial s} < 0$ pulls particles away from the equatorial plane and traps them in off-equatorial regions bounded by two mirror points. Whether the particle hops into the northern or the southern hemisphere depends on its gyrophase at the moment when it approaches the $\frac{\partial B}{\partial s} < 0$ region.
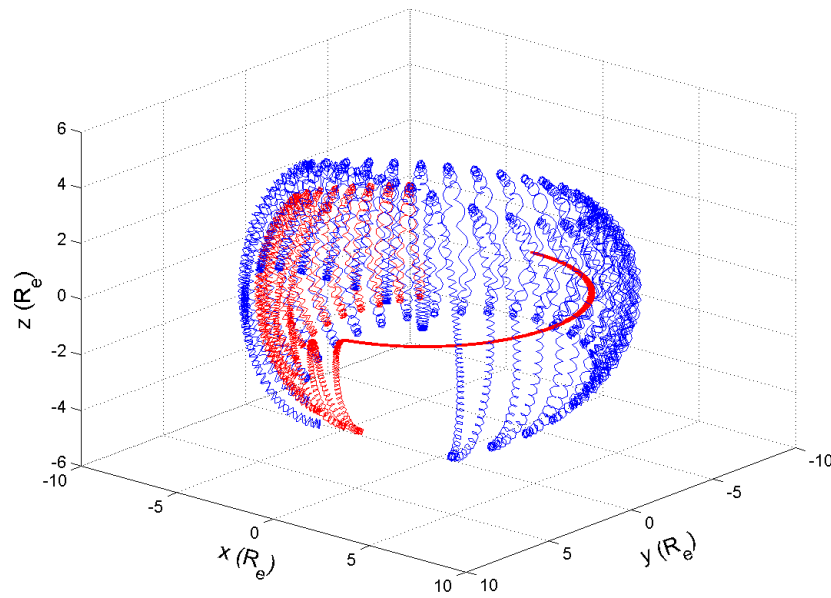
Figure 3.18: Particle trajectories for two different pitch-angles. In the vicinity of the magnetopause, the $90°$ pitch-angle particle (red curve) and the $30°$ pitch-angle particle drift through the off-equatorial region. Note that after passing through the "Shabansky" region the $90°$ pitch-angle particle is no longer trapped in the equatorial plane.

McCollough et al. (2010) have argued that in the off-equatorial B_{min} regions the particle velocity distribution can gain anisotropy due to a particle's pitch-

angle shifting towards higher pitch-angles. This can also lead to the formation of regions of enhanced temperature anisotropy off the equator. Together with the magnetic drift shell splitting, the Shabansky mechanism may be responsible for the generation of anisotropic velocity distributions on high L-shells close to the magnetopause.

3.9.3 Other Mechanisms Responsible for the Temperature Anisotropy

In addition to the processes responsible for the formation of anisotropic particle distributions mentioned above, there are other mechanisms that may provide anisotropy. For example, *Olson and Lee* (1983) considered short-term adiabatic heating of plasma as the source of EMIC waves during sudden enhancements in solar wind dynamic pressure. Enhanced solar wind dynamic pressure will increase the magnetic field as well as ion temperature. However the perpendicular temperature will be intensified more strongly than the parallel temperature which results in temperature anisotropy. Nevertheless, this mechanism cannot explain why EMIC wave activity can last for many hours while the magnetic field remains compressed by enhanced solar wind dynamic pressure.

Temperature anisotropy may be also generated by processes leading to global radial transport of plasma. For example, the convection electric field can provide anisotropy by conserving the first adiabatic invariant as the particle is transported radially inward due to $\mathbf{E} \times \mathbf{B}$ drift (*Summers et al.*, 1998), temperature anisotropy being generated since the perpendicular energization due to conservation of the first adiabatic invariant exceeds that arising in the parallel

direction due to conservation of the second invariant. However, this mechanism is shown to be relatively unimportant during undisturbed geomagnetic conditions (*McCollough et al.*, 2010). Radial transport can also happen as a result of interaction with ULF waves (*Elkington et al.*, 2003). We have not studied this mechanism as a possible source of EMIC wave activity. It may be addressed in the future work.

EMIC Wave Duration and Drift Time of Energetic Particles

Since we do not have unambiguous measurements of the exact proton resonant energy for the EMIC wave event simulated here, we should consider different possible particle energies and discuss how they may be related to our observations. Magnetic drift shell splitting can be considered as the only source of temperature anisotropy if the particle's drift time around the Earth is longer than the observed EMIC event duration, which is about 5 hours for the event of June 29, 2007. Based on the drift time estimate from Chapter 1, the lower energy particles (with energy ~ 10 keV) drifting on closed orbits may solely provide a source for these waves since their drift time period is longer than 10 hours. However, the higher energy which drift around the Earth faster may encircle the source region twice (or more). After the first crossing of the source region, the anisotropy may decrease due to EMIC instability down to the level of marginal stability (see Chapter 4) and on the subsequent passes through the subsolar magnetosphere, these higher energy particles may not have enough anisotropy to excite the waves. Therefore, magnetic drift shell splitting on its own does not suffice to sustain wave activity on a timescale of more than one particle drift period and additional processes (not included in our simulations) responsible for the

formation of anisotropic distributions should be considered. The convection electric field neglected here for simplicity, may provide the source of sustained anisotropy as it may supply "fresh" particles by injection from the nightside magnetosphere.

There are two possible effects of the convection electric field on the particle dynamics. First, due to $\mathbf{E} \times \mathbf{B}$ drift, particles may end up on open drift trajectories and will escape from the magnetosphere by crossing the magnetopause and therefore a constant supply of new particles is required. In such a case the convection electric field may provide a source and sink of energetic particles. Second, both the pre-existing particles on closed drift trajectories and the newly injected particles will be mixed together. This may, nevertheless, sustain sufficient anisotropy for ongoing EMIC wave generation. However, the resulting level of anisotropy in this case should be obtained from further simulations.

3.10 Conclusions

In this chapter, the motion of an ensemble of particles in a compressed magnetosphere has been simulated using a test particle approach. Particle trajectories have been traced backwards in time from the dayside magnetosphere, where the velocity distribution function is unknown, to the midnight magnetosphere where it is defined from the AP8 model. Using Liouville's theorem we have computed the corresponding distribution functions in the dayside equatorial magnetosphere. It is found that the ion distributions in the noon equatorial magnetosphere become anisotropic with $T_\perp > T_\parallel$ as a result of their development due to drift from the nightside.

The dayside temperature anisotropy gradually increases towards the magnetopause, consistent with observations of EMIC wave activity in the dayside magnetosphere by *Anderson and Hamilton* (1993) who found that the probability of observing EMIC waves increases with L-shell. We also looked at the temperature anisotropy MLT dependence and found that the anisotropy remains relatively high within few hours away from the subsolar point which suggests the observable MLT extent of EMIC wave activity of several hours.

By looking at individual particle trajectories, we have concluded that the temperature anisotropy develops due to magnetic drift shell splitting. It has been shown that radial gradients in particle flux in the nightside may produce especially strong temperature anisotropy on the dayside. In addition, it has been shown that the temperature anisotropy for different ion species produced due drift shell splitting will be the same. The next chapter will investigate whether the temperature anisotropy generated due to magnetic drift shell splitting suffices to initiate EMIC wave growth.

Bibliography

Anderson, B., and D. Hamilton (1993), Electromagnetic ion cyclotron waves stimulated by modest magnetospheric compressions, *J. Geophys. Res.*, *98*, 11,369–11,382.

Birdsall, C. K., and A. B. Langdon (1985), *Plasma Physics via Computer simulations*, Graw-Hill, New York.

Cabrera, J., M. Cyamukungu, P. Stauning, A. Leonov, P. Leleux, J. Lemaire, and G. Grgoire (2005), Fluxes of energetic protons and electrons measured on board the oersted satellite, *Annales Geophysicae*, *23*(9), 2975–2982, doi: 10.5194/angeo-23-2975-2005.

De Benedetti, J., A. Milillo, S. O. A. Mura, E. de Angelis, and I. A. Daglis (2005), Empirical Model of the Inner Magnetosphere H Pitch Angle Distributions, in *The Inner Magnetosphere: Physics and Modeling*, *Washington DC American Geophysical Union Geophysical Monograph Series*, vol. 155, edited by T. I. Pulkkinen, N. A. Tsyganenko, & R. H. W. Friedel, p. 283.

Elkington, S. R., M. K. Hudson, and A. A. Chan (2003), Resonant acceleration and diffusion of outer zone electrons in an asymmetric geomagnetic field, *J. Geophys. Res.*, *108*, 1116–+, doi:10.1029/2001JA009202.

Fritz, T. A., M. Alothman, J. Bhattacharjya, D. L. Matthews, and J. Chen (2003), Butterfly pitch-angle distributions observed by isee-1, *Planetary and Space Science*, *51*(3), 205 – 219, doi:10.1016/S0032-0633(02)00202-7.

Garcia, H. A., and W. N. Spjeldvik (1985), Anisotropy characteristics of geomagnetically trapped ions, *J. Geophys. Res.*, *90*, 347–358, doi:10.1029/JA090iA01p00347.

Gussenhoven, M. S., E. G. Mullen, and D. H. Brautigam (1994), Near-earth radiation model deficiencies as seen on CRRES, *Adv. Space Res.*, *14*, 927–941, doi:10.1016/0273-1177(94)90559-2.

Kivelson, M., and C. Russell (1995), *Introduction to Space Physics*, 172 pp., Cambridge Univ. Press, New York.

Marchand, R. (2010), Test-Particle Simulation of Space Plasmas, *Commun. Comput. Phys.*, *8*(3), 471–483, doi:10.4208/cicp.201009.280110a.

McCollough, J. P., S. R. Elkington, M. E. Usanova, I. R. Mann, D. N. Baker, and Z. C. Kale (2010), Physical mechanisms of compressional emic wave growth, *J. Geophys. Res.*

Mead, G. (1964), Deformation of the geomagnetic field by the solar wind, *J. Geophys. Res.*, *69*(7), 1181–1195.

Mead, G., and D. Beard (1964), Shape of the geomagnetic field solar wind boundary, *J. Geophys. Res.*, *69*(7).

Northrop, T. (1963), *The Adiabatic Motion of Charged Particles*, Wiley-Interscience, New York.

Olson, J. V., and L. C. Lee (1983), Pc1 wave generation by sudden impulses, *Planetary and Space Science*, *31*(3), 295 – 302, doi:10.1016/0032-0633(83)90079-X.

Parks, G. (2004), *Physics of space plasmas: an introduction*, Westview Press.

Pfitzer, K. A., T. W. Lezniak, and J. R. Winckler (1969), Experimental verification of drift-shell splitting in the distorted magnetosphere., *J. Geophys. Res.*, *74*, 4687–4693, doi:10.1029/JA074i019p04687.

Shabansky, V. (1971), Some processes in the magnetosphere, *Space Sci. Rev.*, *12*(3), 299–418.

Sibeck, D. G., R. W. McEntire, A. T. Y. Lui, R. E. Lopez, and S. M. Krimigis (1987), Magnetic field drift shell splitting - Cause of unusual dayside particle pitch angle distributions during storms and substorms, *J. Geophys. Res.*, *92*, 13,485–13,497, doi:10.1029/JA092iA12p13485.

Summers, D., R. Thorne, and F. Xiao (1998), Relativistic theory of wave-particle resonant diffusion with application to electron acceleration in the magnetosphere, *J. Geophys. Res.*, *103*(A9), 20,487.

Tsyganenko, N. A. (1996), Effects of the solar wind conditions in the global magnetospheric configurations as deduced from data-based field models, in *International Conference on Substorms*, *ESA Special Publication*, vol. 389, edited by E. J. Rolfe & B. Kaldeich, p. 181.

Vette, J. (1992), AE/AP trapped particle flux maps (1966-1980), *Planetary and Space Science*, *40*(4), 566 – 568, doi:10.1016/0032-0633(92)90240-O.

Zhang, J., M. W. Liemohn, M. F. Thomsen, J. U. Kozyra, M. H. Denton, and J. E. Borovsky (2006), A statistical comparison of hot-ion properties at geosynchronous orbit during intense and moderate geomagnetic storms at solar maximum and minimum, *J. Geophys. Res.*, *111*, 7206, doi:10.1029/2005JA011559.

Chapter 4

Linear Analysis and Nonlinear Kinetic Simulations of EMIC Waves

In this chapter nonlinear EMIC wave generation will be examined by means of linear dispersion theory and numerical simulations. First, we will solve the linearized Vlasov equation which points to the situations where the distribution function may become unstable and describes the linear growth phase of plasma instabilities. It allows us to examine the initial conditions required for EMIC wave generation. Further, we will consider nonlinear evolution of the waves using a hybrid particle-in-cell (PIC) code and will explain some of the observed EMIC wave properties described in Chapter 2.

4.1   Kinetic Description of Plasmas

Plasma may be defined as a statistical ensemble of mobile charged particles moving in the system, interacting with each other through electromagnetic forces

and responding to the electromagnetic disturbances, which may be applied from external sources. Plasmas are, therefore, capable of sustaining rich classes of electromagnetic phenomena. The main approach used in analyzing the plasma waves is the description of plasmas as continuous dielectric medium: applying the dielectric tensor to a set of macroscopic electrodynamics equations and finding a solution in the form of a dispersion relation. The way the dispersion relation is calculated depends on the initial plasma state, electromagnetic fields configuration, and charge and current density profiles. This also determines the types of wave modes that could potentially arise in the system. Important questions to consider in plasma theory, from the wave point of view, are:

- What is the source of free energy in the plasma?

- Which particle species are important for the waves under consideration?

- Is the external magnetic field important or not?

- Are collisions between the particles important?

- What is the amplitude of the waves? Can the linear perturbation theory be applied?

The scope of the present work is limited to collisionless plasmas. Following *Davidson and Ogden* (1975), the behaviour of such plasmas is described by the Vlasov-Maxwell equations in which the distribution function of a species s, $f_s(\mathbf{r}, \mathbf{v}, t)$, evolves according to the Vlasov equation

$$\frac{\partial f_s}{\partial t} + \mathbf{v} \cdot \frac{\partial f_s}{\partial \mathbf{r}} + \frac{q_s}{m_s} \left[\mathbf{E}(\mathbf{r}, t) + \mathbf{v} \times \mathbf{B}(\mathbf{r}, t) \right] \cdot \frac{\partial f_s}{\partial \mathbf{v}} = 0, \tag{4.1}$$

where $\mathbf{E}(\mathbf{r}, t)$ and $\mathbf{B}(\mathbf{r}, t)$ are the average electric and magnetic fields, q_s and m_s are the particle charge and mass. The electromagnetic fields $\mathbf{E}(\mathbf{r}, t)$ and $\mathbf{B}(\mathbf{r}, t)$ in this equation are the sum of those applied from outside sources and those induced from the internal particle distributions. Individually they may be determined from

$$\nabla \times \mathbf{E_{ext}} + \frac{\partial \mathbf{B_{ext}}}{\partial t} = 0, \tag{4.2}$$

$$\nabla \times \mathbf{B_{ext}} - \frac{1}{c^2}\frac{\partial \mathbf{E_{ext}}}{\partial t} = \mu_0 \mathbf{J_{ext}}, \tag{4.3}$$

$$\nabla \cdot \mathbf{E_{ext}} = \rho_{ext}/\epsilon_0, \tag{4.4}$$

$$\nabla \cdot \mathbf{B_{ext}} = 0. \tag{4.5}$$

The same set of equations should be written for the induced fields, where the induced current

$$\mathbf{J_{ind}} = \sum_s q_s \int \mathbf{v} f(\mathbf{v}, \mathbf{r}, t) d^3\mathbf{v}, \tag{4.6}$$

and the induced charge density

$$\rho_{ind} = \sum_s q_s \int f(\mathbf{v}, \mathbf{r}, t) d^3\mathbf{v}. \tag{4.7}$$

The set of Vlasov-Maxwell equation provides a complete kinetic description of the collisionless plasma.

4.2 Linear Stability Theory

Throughout the present analysis, it is assumed that the plasma is immersed in a uniform externally applied magnetic field and that the plasma equilibrium state ($\partial/\partial t = 0$) is characterized by charge neutrality $\sum_s n_s q_s = 0$, and zero external electric field. It is also assumed that the equilibrium plasma current (if any) is sufficiently weak that the corresponding equilibrium self-magnetic field has a negligibly small effect on stability in comparison with the applied magnetic field. It is also assumed that the equilibrium distribution function $f_s^o(\mathbf{r}, \mathbf{v})$ for the species s is spatially uniform $f_s^o(\mathbf{r}, \mathbf{v}) = n_s \mathcal{F}_s(v_\perp^2, v_{||})$. Then, for small adiabatic electromagnetic wave perturbations $\delta\mathbf{E}(\mathbf{r}, t)$ and $\delta\mathbf{B}(\mathbf{r}, t)$ the Vlasov equation for the perturbed distribution function can be written in the linearized form:

$$\frac{n_s q_s}{m_s} \left[\delta\mathbf{E}(\mathbf{r}, t) + \mathbf{v} \times \delta\mathbf{B}(\mathbf{r}, t)\right] \frac{\partial}{\partial\mathbf{v}} \mathcal{F}_s(v_\perp^2, v_{||}) = 0. \tag{4.8}$$

For some trivial cases it is possible to obtain a solution of the linearized Vlasov equation analytically and examine the plasma behaviour based on the linear stability theory. It involves calculation of the plasma dielectric tensor, which will lead to the relation between the wave frequency and the wave vector. We will not show the derivation of the general dispersion relation in magnetized plasmas and only consider linear dispersion relation for transverse electromagnetic waves propagation parallel to the background magnetic field (see *Davidson and Ogden*, 1975):

$$\omega^2 - c^2 k_{||}^2 - \sum_s \omega_{ps}^2 + \sum_s \frac{\omega_{ps}^2}{2} \int \frac{k_{||} v_\perp^2 \partial \mathcal{F}_s/\partial v_{||} \pm 2\Omega_s \mathcal{F}_s}{\omega - k_{||} v_{||} \pm \Omega_s} d^3\mathbf{v} = 0, \tag{4.9}$$

where $\omega = \omega_r + i\gamma$ is the complex wave frequency, $k_{||}$ is the wave number in the direction along the background magnetic field, $\omega_{ps} = (n_s q_s^2 / m_s \epsilon_0)^{1/2}$ is the plasma frequency for the s component, and $\Omega = q_s B / m_s$ is the cyclotron frequency. The +(-) signs denote the waves with right (left)- handed polarization.

In our model, electron distribution function is assumed to be an isotropic Maxwellian, while the ion distribution function is set to be a bi-Maxwellian with perpendicular temperature $T_\perp$ and parallel temperature $T_{||}$. Then the dispersion relation becomes:

$$\omega^2 - c^2 k_{||}^2 + \omega_{pe}^2 \frac{\omega}{k_{||} v_e} Z(\zeta_e^\pm) + \sum_i \omega_{pi}^2 \frac{\omega}{k_{||} v_{i||}} Z(\zeta_i^\pm)$$

$$- \sum_i \omega_{pi}^2 (1 - T_{i\perp}/T_{i||})(1 + \zeta_i^\pm Z(\zeta_i^\pm)) = 0, \qquad (4.10)$$

where $\zeta_e^\pm = (\omega \pm \Omega_e)/k_{||} v_e$, $v_e = (2T_e/m_e)^{1/2}$, $\zeta_i^\pm = (\omega \pm \Omega_i)/k_{||} v_{i||}$, $v_i = (2T_{i||}/m_i)^{1/2}$, i denotes ions and e - electrons, and $Z(\zeta)$ is the plasma dispersion function,

$$Z(\zeta) = \frac{1}{\sqrt{\pi}} \int_{-\infty}^{+\infty} \frac{exp(-x^2)}{x - \zeta}. \qquad (4.11)$$

4.2.1 EMIC Wave Linear Dispersion Relation

Equation 4.10 has been solved using code provided by K. Sauer. The code finds the roots of Equation 4.10 numerically, utilizing the Newton-Raphson method. The results for different input parameters (the ion temperature anisotropy $T_{i\perp}/T_{i||}$ and the ratio of the ion thermal energy to the magnetic field energy $\beta_i = 2\mu_0 n_i k_B T_i / B^2$) are summarized in Figures 4.1 – 4.4. In each figure, the panels show (starting

from the top) the real wave frequency, the wave growth rate (imaginary part of wave frequency) and the wave phase velocity as a function of the wave number. The frequency is in units of the H^+ cyclotron frequency, Ω_{H^+}, and the length is in units of V_A/Ω_{H^+}, where V_A is the Alfvén speed.

Anisotropic H^+ Species

First, we consider the case when only anisotropic H^+ population is present. The Figures 4.1 – 4.4 illustrate that the cyclotron instability requires larger values of the temperature anisotropy A for low β. For example, no instability is generated for $A = 2$ and $\beta = 0.01$ ($\gamma \simeq 0$) while for the same level of anisotropy with $\beta = 1$ the unstable solution (see Figure 4.2) exists. These results are consistent with earlier findings by *Gary et al.* (1993); *Anderson et al.* (1994); *Fuselier et al.* (1994); *Gary et al.* (1994) that the EMIC marginal stability is determined by hydrogen anisotropy and parallel plasma β, where A and β are inversely correlated. For example, based on a statistical satellite data analysis, (*Anderson et al.*, 1994) derived the following relationship between the temperature anisotropy and parallel hydrogen plasma β for the magnetosheath: $T_{H\perp}/T_{H||} - 1 = 0.85\beta_{H||}^{-0.48}$.

Figures 4.1 – 4.4 also show that the unstable $\omega - k$ range for EMIC wave growth in a H^+ plasma with $\beta = 1$ is wider and shifted towards lower wave numbers with respect to the case of $\beta = 0.01$. The phase velocity generally decreases with k as well as with ω. This is consistent with typical observations of dispersion within EMIC wave packets on the ground showing that the lower frequency reaches the ground first, before the higher frequencies of the wave spectrum. However, in the case of relatively high A and plasma β (for example, $A = 5$ and $\beta = 1$) the phase velocity profile as a function of k has a knee. For

some range of the wave numbers in this case the phase velocity increases with k which may explain the inverse EMIC wave dispersion, for example, observation reported by *Feygin et al.* (2007).
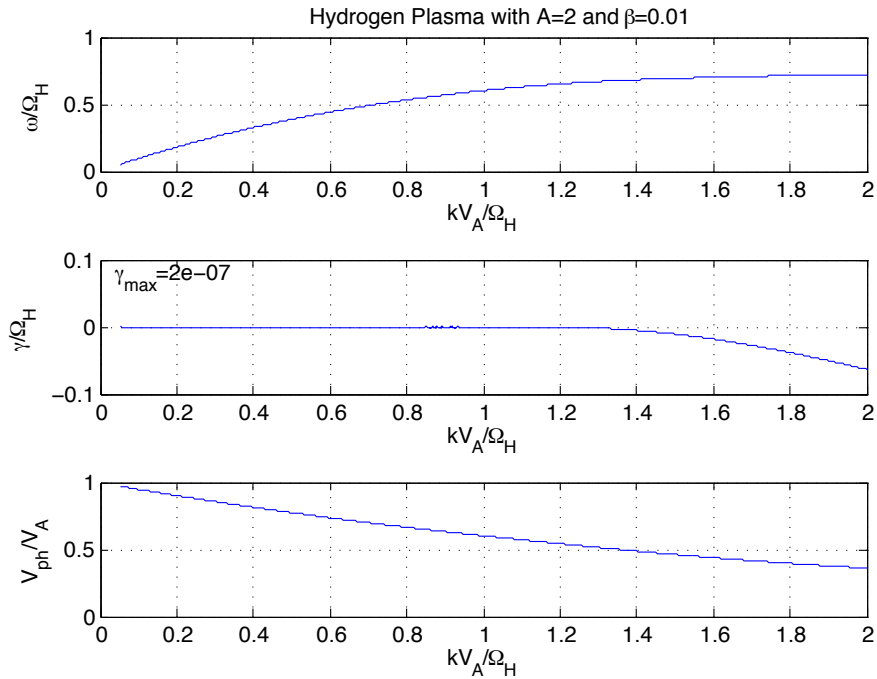
Figure 4.1: Solution of the linear dispersion relation for a H^+ plasma with $A = 2$ and $\beta = 0.01$. The top panel shows the real part of the wave frequency ω as a function of the wave number k, the middle panel shows the wave growth rate γ as a function of the wave number k, and the bottom panel shows the wave phase velocity as a function of the wave number k.

Figure 4.5 shows solution of the dispersion relation for the case when the hot anisotropic H^+ population constitutes only 10% of the total density and the rest 90% is cold isotropic H^+ with $\beta = 0.001$. The figure illustrates the fact that the wave spectrum in the presence of the cold background becomes more narrow and the maximum wave growth rate is reduced.
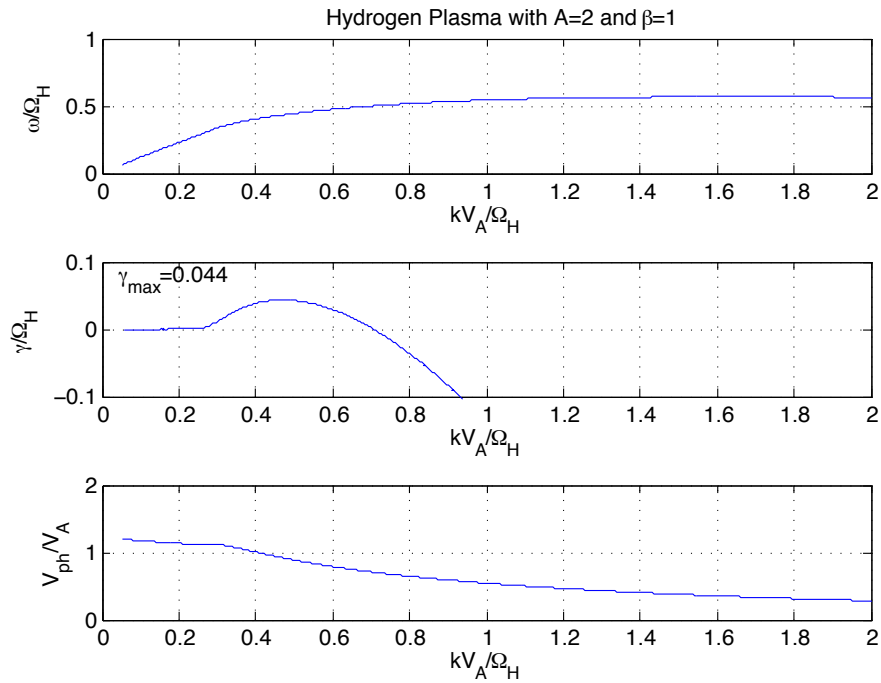
Figure 4.2: Solution of the linear dispersion relation for a H^+ plasma with $A = 2$ and $\beta = 1$. The top panel shows the real part of the wave frequency ω as a function of the wave number k, the middle panel shows the wave growth rate γ as a function of the wave number k, and the bottom panel shows the wave phase velocity as a function of the wave number k.
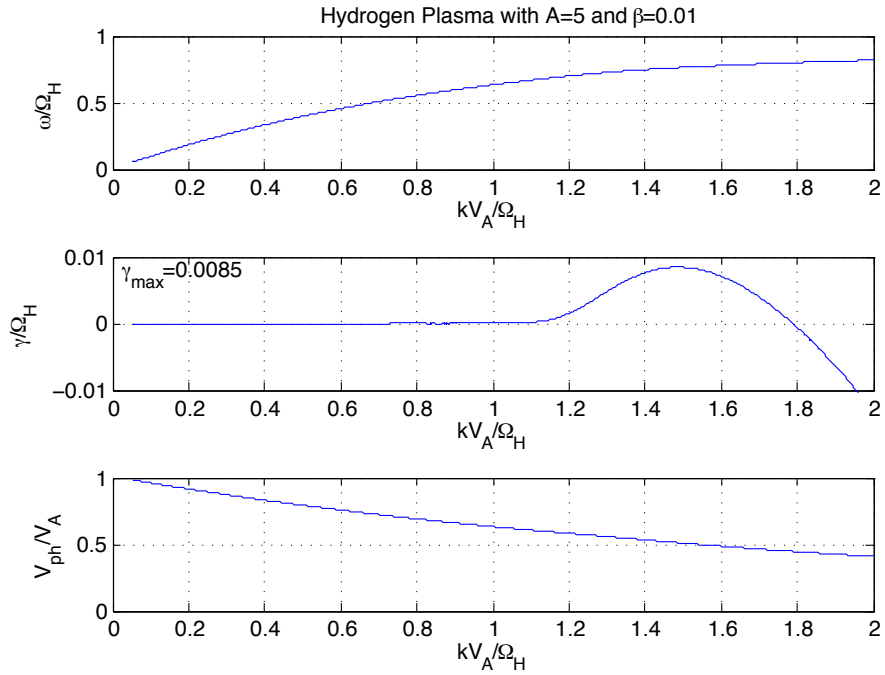
Figure 4.3: Solution of the linear dispersion relation for a H^+ plasma with $A = 5$ and $\beta = 0.01$. The top panel shows the real part of the wave frequency ω as a function of the wave number k, the middle panel shows the wave growth rate γ as a function of the wave number k, and the bottom panel shows the wave phase velocity as a function of the wave number k.
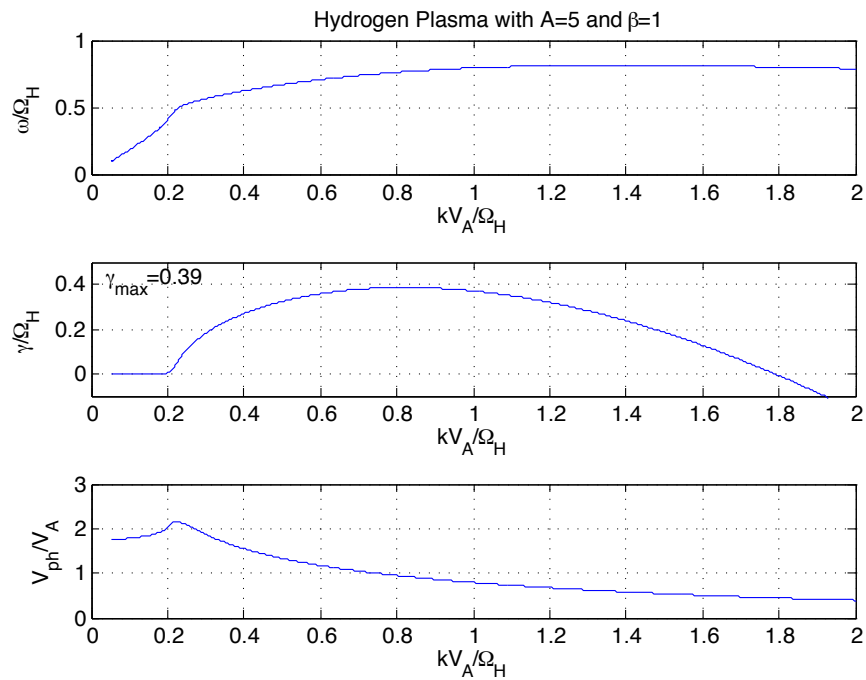
Figure 4.4: Solution of the linear dispersion relation for a H^+ plasma with $A = 5$ and $\beta = 1$. The top panel shows the real part of the wave frequency ω as a function of the wave number k, the middle panel shows the wave growth rate γ as a function of the wave number k, and the bottom panel shows the wave phase velocity as a function of the wave number k.
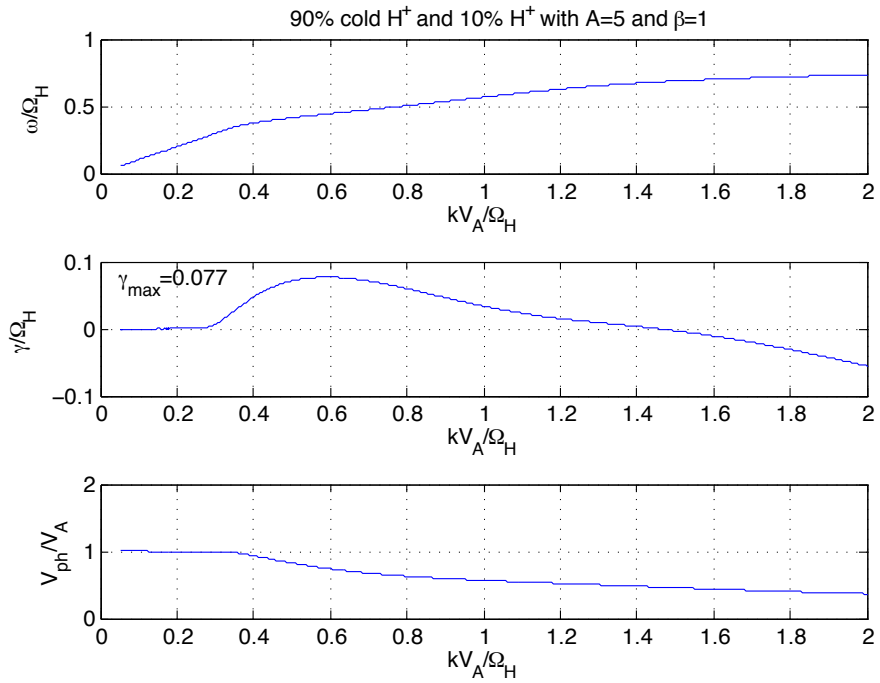
Figure 4.5: Solution of the linear dispersion relation for a plasma with 90% cold H^+ and 10% hot H^+ with $A = 5$, $\beta_H = 1$. The top panel shows the real part of the wave frequency ω as a function of the wave number k, the middle panel shows the wave growth rate γ as a function of the wave number k, and the bottom panel shows the wave phase velocity as a function of the wave number k.

Anisotropic H^+ and He^+ Species

For this set of simulations we considered a plasma with 90% of H^+ ions and a 10% admixture of He^+ ions by number with equal temperature anisotropies and temperature. The set of input parameters was the same as for those examined for the purely H^+ plasma. In the presence of He^+ ions, the wave spectrum has two branches: the H^+ branch which now starts at some frequency called the cut-off frequency, above the He^+ gyrofrequency, and the He^+ branch which exists in some limited range of wave numbers below and above the He^+ gyrofrequency but which is linearly stable (see Figure 4.6). Close to the He^+ cyclotron frequency there is a spectral gap in the wave activity due the wave energy resonant absorbtion by the He^+ species. Generally, the maximum wave growth rate in the two-component plasmas is higher for the H^+ as it has a larger amount of free energy due to larger number density and also gyrates faster. Also, the growth rate for the H^+ branch is slightly lower in the presence He^+ since the fraction of H^+ ion species is lower.

Figure 4.7 shows dispersion curves for the case of both H^+ and an admixture of He^+ being anisotropic with $A = 5$ and taken in the same proportion as in Figure 4.6 but for low β. The He^+ branch is stable and the maximum growth rate of the H^+ branch is slightly lower than in the case of pure hydrogen plasma with the same β.
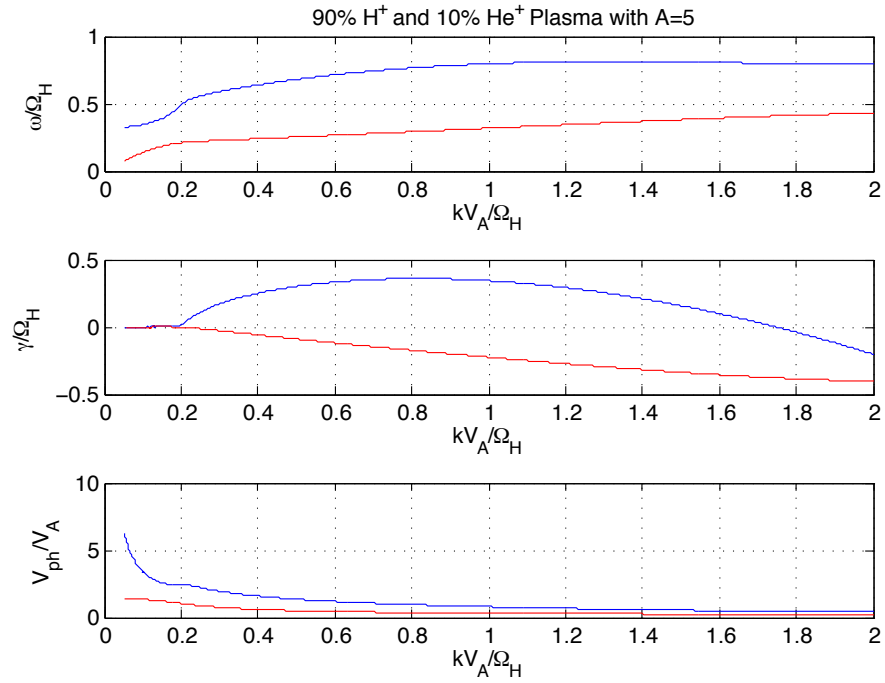
Figure 4.6: Solution of the linear dispersion relation for a plasma with $90\% \ H^+$ and $10\% \ He^+$ with $A = 5$, $\beta_H = 1$, $\beta_{He} = 0.1$. The top panel shows the real part of the wave frequency ω as a function of the wave number k, the middle panel shows the wave growth rate γ as a function of the wave number k, and the bottom panel shows the wave phase velocity as a function of the wave number k.
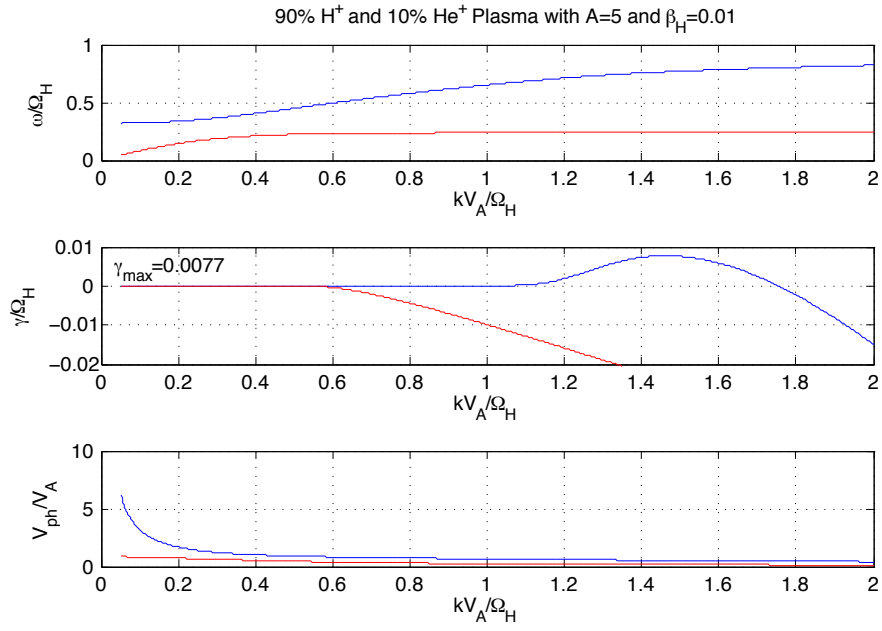
Figure 4.7: Solution of the linear dispersion relation for a plasma with 90% H^+ and 10% He^+ with $A = 5$, $\beta_H = 0.01$, $\beta_{He} = 0.001$. The top panel shows the real part of the wave frequency ω as a function of the wave number k, the middle panel shows the wave growth rate γ as a function of the wave number k, and the bottom panel shows the wave phase velocity as a function of the wave number k.

4.2.2 Linear Theory Predictions for EMIC Source Region Location

Using linear theory we can predict the anisotropy threshold level A for three possible scenarios ($\beta = 1$, $\beta = 0.3$, and $\beta = 0.01$). Utilizing the anisotropy profiles obtained from the previous chapter, one can make the following prediction for the location of EMIC source region:

- for high plasma β, initially isotropic distributions become unstable at $L > 5.5$ on the dayside during strong magnetospheric compression and at $L > 6.5$ during weak magnetospheric compression;

- for moderate plasma β, initially isotropic distributions are stable to EMIC waves during weak magnetospheric compression but become unstable at $L > 6.4$ on the dayside during strong magnetospheric compression;

- for low plasma β, initially isotropic distributions will always be stable to EMIC waves;

- for high and moderate plasma β, initially anisotropic $\sin^2(\alpha)$ pitch-angle distributions are always unstable to EMIC waves;

- for low plasma β, initially anisotropic $\sin^2(\alpha)$ pitch-angle distributions will be unstable at $L > 6.1$ on the dayside during strong magnetospheric compressions and stable during weak magnetospheric compressions.

Generally, the concept of EMIC wave generation due to magnetic drift shell splitting is credible, since the linear theory shows that sufficiently high rates of temperature anisotropy can be generated and gives a reasonable estimate for

the inner boundary of the source region (given by the threshold anisotropy for the EMIC instability). However, the ambiguity in plasma β value as well as the relatively simple magnetic field model used for the test particle simulations give some freedom in relation to the interpretation of the results. Therefore, one should not expect ideal agreement between the observations and the simulations. Most likely, as follows from the AP8 model estimate of plasma β in the region supported by the observations, the plasma β is moderate. However, in a more rigorous analysis more exact plasma parameters as ion temperature, plasma β, and ion composition are required and could be derived from observations.

4.3 Hybrid Particle-in-Cell Method

Usually, the term "hybrid code" in plasma physics refers to any simulation model in which one or more of the plasma species are treated as massless fluids, while the remaining species are treated kinetically as particles. Hybrid codes result from the requirement to model phenomena that occur on ion gyroscales but do not need to resolve processes that occur on electron spatial and temporal scales. In particle-in-cell (PIC) codes, ion distributions are treated kinetically using the following standard techniques. Similar to Chapter 3, a leapfrog method is used to advance the trajectories of ions in electric and magnetic fields. However the electric and magnetic fields produced by the ion distributions are no longer neglected and are computed self-consistently through moments of the ion distribution function: the ion number density n_i, charge density $q_i n_i$, flow velocity $\mathbf{v}_i$ and current $\mathbf{j}_i = q_i n_i \mathbf{v}_i$. For multiple ion species, the quantities for

each ion species are computed separately and then added together to determine the total charge and current densities. The magnetic field is advanced by Faraday's law:

$$\frac{\partial \mathbf{B}}{\partial t} = -\nabla \times \mathbf{E}. \tag{4.12}$$

Electrons are described as a charge-neutralizing massless fluid, therefore, no electron test-particles are advanced. Instead, an approximate form of the electron momentum equation is utilized. The form most often used only retains the $\mathbf{j} \times \mathbf{B}$ force, the gradient of a scalar electron pressure p, and a resistivity term $\eta \mathbf{j}$ (due to coupling between the electrons and ions). When the current density and ion velocity are substituted for the electron velocity, the electron momentum equation takes the form of a generalized Ohm's law:

$$\mathbf{E} = -\mathbf{v_i} \times \mathbf{B} + \frac{\mathbf{j} \times \mathbf{B}}{q_i n_i} - \frac{\nabla p_e}{q_i n_i} + \eta \mathbf{j}. \tag{4.13}$$

The hybrid PIC code (1D in coordinate space and 3D in velocity space, with periodic boundary conditions) used in this chapter, was developed by *Krauss-Varban and Omidi* (1995). Technical aspects addressing the numerical algorithm implementation are described in detail in *Harned* (1982).

4.3.1   Results of the Hybrid PIC Simulation

In this section, we considered the nonlinear evolution and saturation of the EMIC instability. Two cases have been analyzed and are presented in this chapter:

- plasma consisting of only hot anisotropic hydrogen species,

- plasma consisting of 90% of hot anisotropic hydrogen and 10% of hot anisotropic helium ions.

Anisotropic H^+ Ions

The first run was performed for the anisotropic H^+ population with $A = 4$ and $\beta = 1$. The set of figures below illustrates the fundamental features of the EMIC instability. The contour plot in Figure 4.8 (left) shows the magnetic field amplitude as a function of time (in H^+ cyclotron periods T_{H^+}) and position (in units of V_A/Ω_{H^+}). The figure demonstrates that the waves are travelling in the positive and negative directions with the same phase velocity, as follows from the slope of the wave fringes. The colorbar shows the wave amplitude normalized by the background magnetic field strength. While the instability develops, the wave number decreases (small-scale wave structures appear first, being replaced with time by large-scale structures). The slice through the center of the computational domain at the time $t = 150\,T_{H^+}$ shows the wave amplitude profile as a function of position (right panel in Figure 4.8).

Figure 4.9 (left) shows the natural logarithm of the wave magnetic field norm (the wave amplitudes squared summed over the computational domain, $\sum by_i^2$) as a function of time. It illustrates that the wave amplitude starts growing rapidly, after ~ 25 cyclotron periods reaches its saturation level, and then slowly decreases. The growth rate of the instability as well as the wave amplitude after saturation depends on the temperature anisotropy and hydrogen plasma β. The particle distribution function evolves together with the wave field as demon-
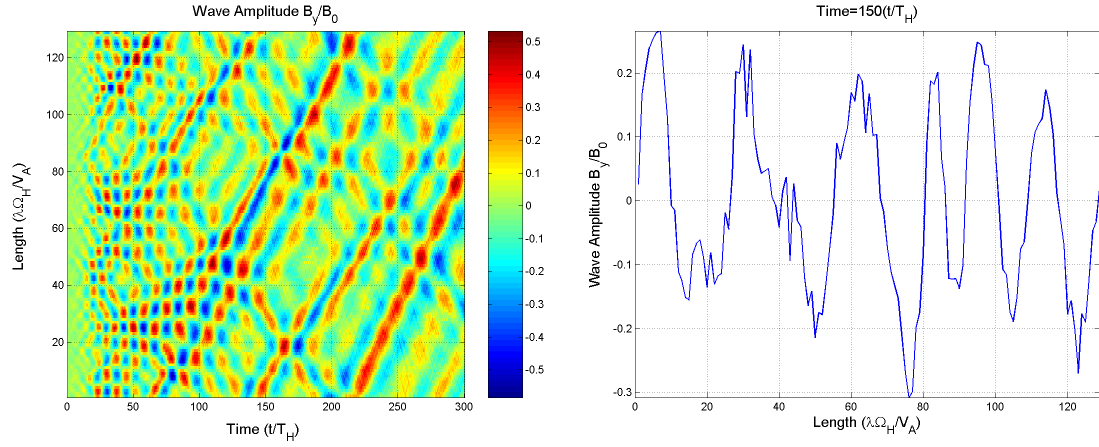
Figure 4.8: Normalized wave amplitude as a function of time and position (left) and as a function of position at $t = 150\ T_{H^+}$ (right) for a H^+ plasma with $A = 4$ and $\beta = 1$. See text for details.

strated in the right panel of Figure 4.9. The parallel temperature increases during the instability growth phase due to the nonlinear $\mathbf{j} \times \mathbf{B}$ force heating the distribution in the parallel direction. The perpendicular temperature decreases and so does the temperature anisotropy. The growth of the instability and consequent nonlinear system evolution lead to the isotropization of the distribution function. The final temperature anisotropy (similar to the wave amplitude) is determined by the initial conditions (A and plasma β).

The left panel in Figure 4.10 shows the wave spectrum obtained in our simulations together with the linear dispersion relation (superposed in red). The dispersion relation obtained from the simulations is in good agreement with the linear theory prediction. It illustrates the fact that in the range of the wave numbers and frequencies excited, the frequency is proportional to the wave number so that the phase velocity is nearly constant.

The right panel in Figure 4.10 illustrates the evolution of the wave spectrum with time. The EMIC growth starts from high wave numbers (short wave-
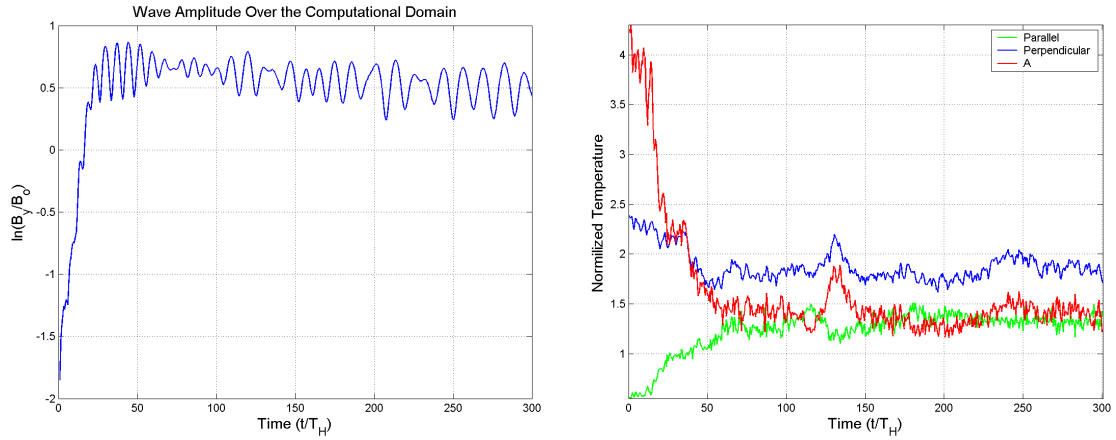
Figure 4.9: (left) Natural logarithm of the wave magnetic field norm ($\sum by_i^2$) and (right) parallel temperature (green curve), perpendicular temperature (blue curve) and their ratio (red curve) as a function of time for a H^+ plasma with $A = 4$ and $\beta = 1$.
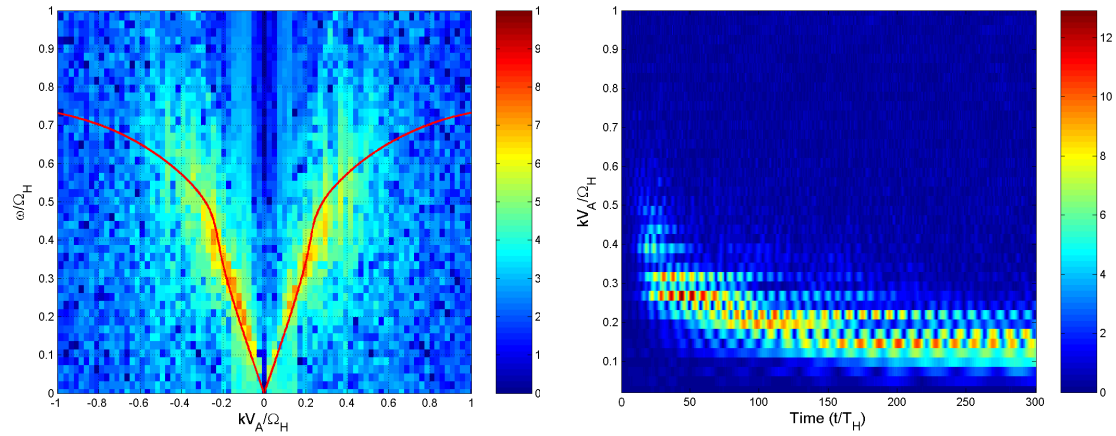
Figure 4.10: Contour plots of the wave spectrum for whole simulation (left) and of the wave number spectrum as a function of time (right) for a H^+ plasma with $A = 4$ and $\beta = 1$. Plotted on top of the wave spectrum (in red) is the dispersion relation obtained from the linear theory.

lengths) and shifts towards lower wave numbers (long wavelengths) as the simulation continues. As the wave spectrum evolves, the wave frequency decreases as well following the linear dispersion relation.

Figure 4.11 shows the development of the instability when the initial H^+ distribution is less anisotropic ($A = 2$). The linear dispersion relation for this case is shown by the red line in Figure 4.11 (left). One can see that the slope (the phase speed) is no longer a constant and becomes flatter at higher frequencies meaning the higher frequency waves within the spectrum propagate more slowly than the lower frequency waves. The wave number reduces with time but does so at a much slower rate when $A = 2$ than for the case of $A = 4$, as shown in Figure 4.11 (right). The same trend applies to both the rate at which the anisotropy decreases and to the wave growth rate, both being slower when $A = 2$ than when $A = 4$.
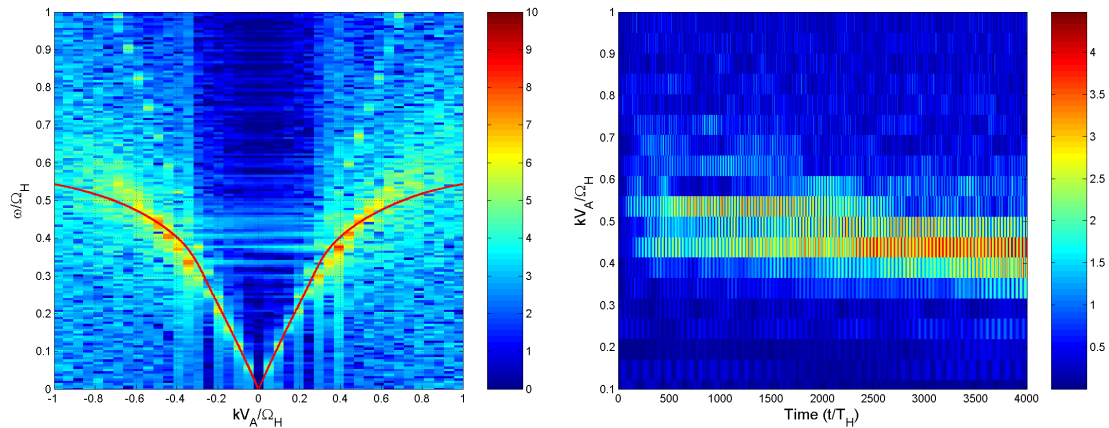
Figure 4.11: Contour plot of the wave spectrum (left) and the wave number spectrum as a function of time (right) obtained in the simulations for $A = 2$ and $\beta = 1$. Plotted on top of the wave spectrum (in red) is the dispersion relation obtained from the linear theory. The instability initiates at high wave numbers and continuously drifts towards lower wave numbers as the simulation continues.

Anisotropic H^+ and He^+ Ion Species

The second set of runs was executed for a plasma consisting of 90% (by number) of H^+ with $\beta = 1$ and 10% of He^+ with $\beta = 0.1$ and with both ion species having equal initial anisotropy $A = 5$ and equal temperatures. In the presence of the He^+ ion species the wave behaviour changes with respect to the case of a pure hydrogen plasma. First, the wave spectrum splits into two bands: below and above the He^+ gyrofrequency, Ω_{He^+}, as reflected in the wave spectrum in Figure 4.12 (left). Figure 4.12 also shows the second H^+ right-handed branch, which is expected to be stable in the range of wave numbers and frequencies considered here, but grows from the initial numerical noise. The nonlinear evolution of the wave number during the simulation is illustrated in Figure 4.12 (right). The instability starts at high wave numbers and gradually moves towards lower wave numbers (and hence frequencies) as in the case of pure anisotropic hydrogen plasma.

However, when the wave frequency approaches the helium gyrofrequency the wave energy is resonantly absorbed by the He^+ ions, resulting in the spectral slot region at the Ω_{He^+}. Further, the wave spectrum falls below the Ω_{He^+} and the wave activity continues in this band. This resonant absorption affects the wave amplitude which becomes lower (compared to the first run) as well as the final anisotropy level. The He^+ temperature anisotropy decreases within the first 50 cyclotron periods from 5 to 1.2 and the temperature of He^+ keeps on increasing in the course of the entire simulation (not shown here). At the same time, the H^+ population loses its free energy to EMIC wave growth and helium ion heating. The final H^+ anisotropy in this case is lower ($A \approx 1.1$) than in the previous
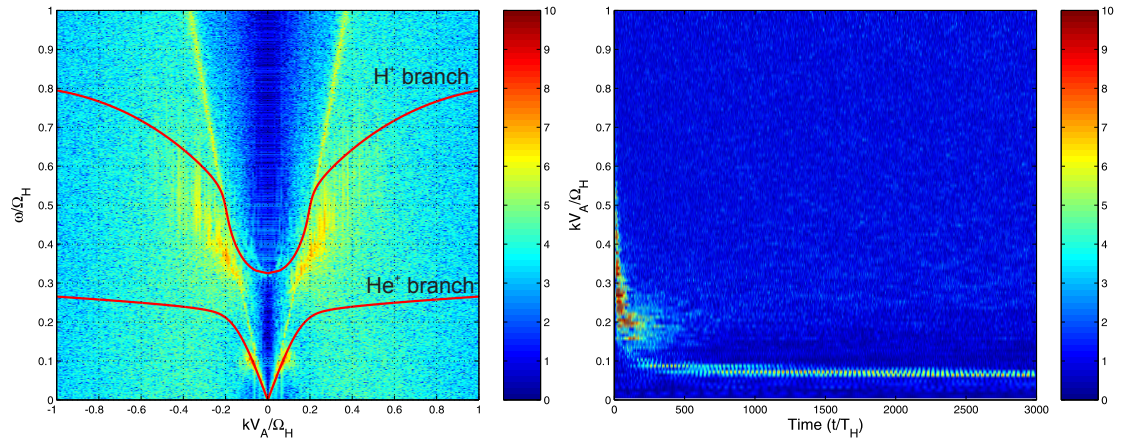
Figure 4.12: (left) Contour plot of the wave spectrum obtained in simulations for both H^+ and He^+ with $A = 5$, $\beta_H = 1$ and $\beta_{He} = 0.1$. Three modes are present in the figure: the H^+ branch, the He^+ branch, and the second H^+ right-handed branch, which is expected to be stable in the range of wave numbers and frequencies considered here, but grows from the initial numerical noise. Superposed (in red) is the dispersion relation obtained from the linear theory. (right) Contour plot of the wave number as a function of time for the same parameters as in the left panel. The instability initiates at high wave numbers and continuously drifts towards lower wave numbers below the helium gyrofrequency being absorbed at the helium gyrofrequency.

example, despite the fact that the initial anisotropy was higher ($A = 5$).
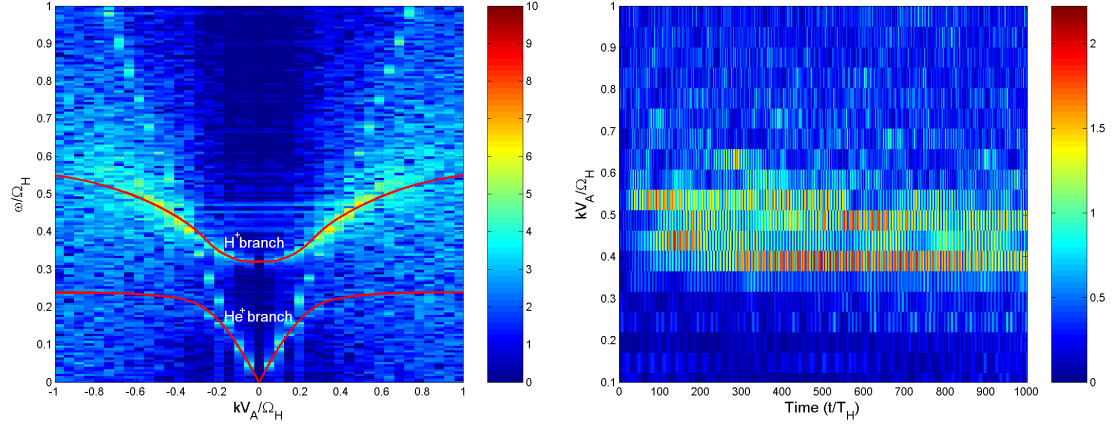
Figure 4.13: Contour plot of the wave spectrum (left) and the wave number spectrum as a function of time (right) for a H^+ and He^+ plasma both with $A = 2$, $\beta_H = 1$ and $\beta_{He} = 0.1$. Superposed on the wave spectrum (in red) is the dispersion relation obtained from the linear theory.

In the case of an initially lower temperature anisotropy ($A = 2$) only the H^+ branch is excited and present in the spectrum (see Figure 4.13). The He^+ branch is not excited. Therefore, the initial level of the temperature anisotropy (free energy) controls not only the final wave amplitude but also how the wave spectrum evolves.

4.3.2 EMIC Wave Packet Generation

In this subsection we investigate mechanisms leading to EMIC wave packet generation. As discussed earlier in Chapter 2, EMIC wave packet generation might occur during their propagation along the magnetic field line and their bouncing between conjugate hemispheres (bouncing wave packet model), or by the modulation of the source region plasma by lower frequency waves on a time-scale of the wave packet repetition period. The simulation runs presented

here were performed for a pure anisotropic H^+ plasma with $A = 2$ and $\beta = 1$. Note that in our model the background magnetic field is uniform, the computational domain covers only an anisotropic source region where temperature anisotropy is spatially constant and any external waves that could potentially modulate EMIC wave growth are absent. Under these conditions, our model clearly shows the formation of sustained quasi-regular EMIC wave packets as is demonstrated in Figure 4.14. The bottom panel of Figure 4.15 further shows the natural logarithm of the wave magnetic field norm ($\sum by_i^2$) computed over the computational box as a function of time and the top panel shows its spectrogram, both indicating packet behaviour.
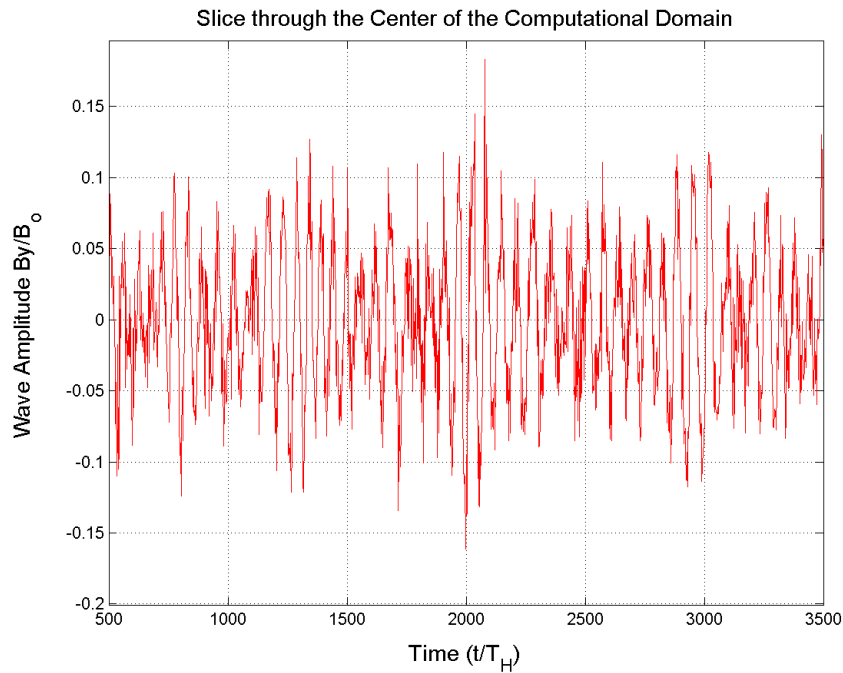
Figure 4.14: Wave amplitude, by, in the center of the computational domain as a function of time between $500 - 3500$ T_{H+} .

These simulation results look very similar to the spectrograms of magne-

tometer data presented earlier in this thesis. Our simulation results demonstrate that neither the bouncing wave packet model nor ULF modulation of EMIC growth rate in source region is required to explain the observed wave spectrum. *Sydora et al.* (2007) simulated a similar type of instability generated by the cyclotron resonance with anisotropic electrons, producing whistler waves on time-scales of an electron gyroperiod. Analogous to the results here, *Sydora et al.* (2007) observed almost monochromatic wave packets with a frequency about one half of the initial frequency of the instability. They found that the wave packets appear at the system saturated state (representing marginal stability) and their existence requires the coincidence of wave phase and group velocity. Our future studies will investigate whether this explanation holds in the case of EMIC wave packet generation. We will further investigate the effect of periodic boundary conditions on the wave packet structure obtained from simulations by varying the size of the simulation domain and by implementing open boundary conditions. This will help us to pinpoint the mechanism responsible for the wave packet generation and to relate the repetition period of the wave packets to the wave propagation in a finite size spatial domain.

4.4 Conclusions

In this chapter, the linear and nonlinear evolution of the EMIC wave instability have been presented. The linear dispersion relation for the case of wave propagation along the background magnetic field has been solved numerically. For EMIC instability, the important parameters are the temperature anisotropy and plasma β. First, based on the linear stability theory, the range of initial aniso-
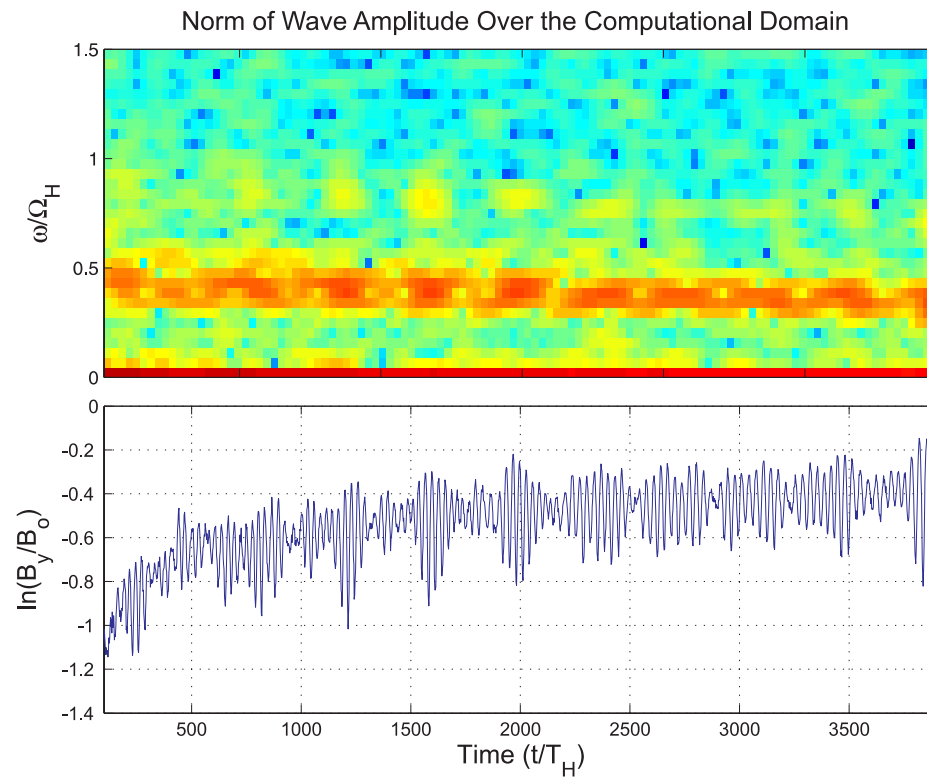
Figure 4.15: Spectrogram of the natural logarithm of the wave amplitude norm computed over the computational box (top panel). Natural logarithm of the wave amplitude norm computed over the computational box as a function of time (bottom panel).

tropy and plasma β that would lead to the growth of the instability was investigated. It was found that the instability initiates at $A \approx 1.4$ for high plasma β and at $A \approx 4$ for low plasma β. This restricts the location of the inner boundary of the EMIC source region which can be developed through drift shell splitting to $L \gtrsim 5.5$ based on the Mead magnetic field model results presented in Chapter 3.

It has been shown that the wave spectrum obtained from the nonlinear simulations is significantly different from the linear theory predictions, so it is important to consider the instability during its growth and saturation self-consistently. It has been found that the initial EMIC instability growth phase develops in agreement with the linear theory predictions. After the growth phase, a subsequent saturation process where the wave number and frequency gradually decrease with time to lower numbers takes place similar to the results presented by *Sydora et al.* (2007) in relation to the non-linear development of whistler waves. It has been found that during saturation, the wave frequency may fall below the Ω_{He^+} even in the absence of He^+ species. Earlier works, based solely on linear theory predictions were required to explain such wave spectral features by the presence of He^+ ions. Our results may explain the fact that EMIC waves below the helium gyrofrequency are those most often observed, and we show that this can occur even without the presence of He^+. When He^+ species are added, the wave activity is also sustained in the band below the Ω_{He^+}, the source of free energy still however being provided by the H^+ species.

In a saturated, nonlinear state, EMIC waves group into characteristic wave packets which according to the *Sydora et al.* (2007) theory for the whistler branch could be the result of nonlinear system evolution. Our results show that gen-

eration of these wave packets is not necessarily related to either the presence of ULF waves, or field inhomogeneities, or wave propagation in the magneto-sphere between conjugate hemispheres, as earlier theories have suggested.

Future studies will continue examining EMIC wave properties self-consistently, using numerical modelling. The role of the cold plasma background (shown to be important in our observations) in the wave growth will be investigated. In addition, EMIC wave propagation effects will be considered in a dipole ge-ometry allowing for a density profile varying along the field line. These fur-ther simulations are intended to answer the question of how the dispersive wave packets are being formed in the realistic magnetosphere and how they might evolve during propagation from the equatorial magnetosphere towards the ionosphere.

Bibliography

Anderson, B. J., S. A. Fuselier, S. P. Gary, and R. E. Denton (1994), Magnetic spectral signatures in the Earth's magnetosheath and plasma depletion layer, *J. Geophys. Res.*, *99*, 5877–5891, doi:10.1029/93JA02827.

Davidson, R., and J. Ogden (1975), Electromagnetic Ion-cyclotron Instability Driven by Ion Energy Anisotropy in High-beta Plasmas, *Phys. Fluids*, *18*(8), 1045–1050.

Feygin, F., A. Nekrasov, T. Pikkarainen, T. Raita, and K. Prikner (2007), Pc1 pearl waves with magnetosonic dispersion, *Journal of Atmospheric and Solar-Terrestrial Physics*, *69*(14), 1644 – 1650.

Fuselier, S. A., B. J. Anderson, S. P. Gary, and R. E. Denton (1994), Inverse correlations between the ion temperature anisotropy and plasma beta in the Earth's quasi-parallel magnetosheath, *J. Geophys. Res.*, *99*, 14,931–14,936, doi:10.1029/94JA00865.

Gary, S. P., B. J. Anderson, R. E. Denton, S. A. Fuselier, M. E. McKean, and D. Winske (1993), Ion anisotropies in the magnetosheath, *Geophys. Res. Lett.*, *20*, 1767–1770, doi:10.1029/93GL01700.

Gary, S. P., P. D. Convery, R. E. Denton, S. A. Fuselier, and B. J. Anderson (1994), Proton and helium cyclotron anisotropy instability thresholds in the magnetosheath, *J. Geophys. Res.*, *99*, 5915–5921, doi:10.1029/93JA03243.

Harned, D. S. (1982), Quasineutral hybrid simulation of macroscopic plasma phenomena, *J. Comp. Phys.*, *47*, 452–462.

Krauss-Varban, D., and H. Omidi (1995), Large-scale hybrid simulations of the magnetotail during reconnection, *Geophys. Res. Lett.*, *22*, 3271–3274.

Sydora, R. D., K. Sauer, and I. Silin (2007), Coherent whistler waves and oscilliton formation: Kinetic simulations, *Geophys. Res. Lett.*, *34*, 22,105, doi: 10.1029/2007GL031839.

Chapter 5

Concluding Remarks

5.1 Summary of Results

In this thesis the generation of compression-related EMIC waves in the inner dayside magnetosphere has been investigated using ground-based and in situ observations. These observational studies were supported by "global" test particle simulations of ring current dynamics as well as "local" simulations of the wave growth in the source region.

5.1.1 Observations

Multiple observations of EMIC wave activity both in space and on the ground have been presented. It has been shown that EMIC wave activity can be intensified during magnetospheric compressions associated with enhanced solar wind dynamic pressure. Contrary to earlier studies, it has been shown that magnetospheric compressions are important for EMIC wave generation not only close to the subsolar magnetopause but also in the inner dayside magnetosphere.

Using satellite measurements, it has been shown that the EMIC waves were generated in regions of enhanced plasma density, just inside the plasmapause. It has been also shown that for the events studied the EMIC wave repetition period on the ground could not be explained by the ULF wave modulation theory.

Our observations also confirm that EMIC waves can cause precipitation of energetic protons and in some cases also appear to be responsible for simultaneous pitch-angle diffusion of MeV energy electrons. Consequently, we suggest that compression-related EMIC waves can be responsible for an important loss of particles from the the ring current as well as perhaps from the radiation belts.

5.1.2 Test-particle Simulations

The motion of an ensemble of particles in a compressed magnetosphere has been simulated using a test particle approach. Particle trajectories have been traced backwards in time from the dayside magnetosphere, where the velocity distribution function is unknown to the midnight magnetosphere, where it is defined from the AP8 model. Using Liouville's theorem we have computed the corresponding distributions in the dayside equatorial magnetosphere. It is found that ion distributions in the noon equatorial magnetosphere become anisotropic with $T_\perp > T_\parallel$. By looking at individual particle trajectories, we have concluded that the temperature anisotropy develops due to magnetic drift shell splitting. It has been shown that radial gradients in particle flux in the night side may produce even stronger temperature anisotropy in the day side. In addition, it has been shown that the temperature anisotropy produced by drift shell splitting for different energetic ion species will be the same.

5.1.3   Self-consistent Simulations

The linear and nonlinear evolution of the EMIC wave instability has been presented. The linear dispersion relation for the case of wave propagation along the background magnetic field has been solved numerically. For EMIC instability the important parameters are the temperature anisotropy and plasma β. First, based on the linear stability theory, the range of initial anisotropy and plasma β that would lead to the growth of the instability has been investigated. It has been found that the instability initiates at $A \approx 1.4$ for high plasma β and at $A \approx 4$ for low plasma β. This restricts the location of the inner boundary of the EMIC source region which can develop through drift shell splitting to $L > 5.5$.

From self-consistent EMIC instability simulations, the observed characteristic wave packet structure has been reporoduced. The wave packets appear as the instability develops and progresses into the marginal stability regime as result of nonlinear system evolution. It has been shown that the wave packets can be generated without requiring the presence of "external" ULF waves (suggested by ULF modulation theory) or propagation effects as the waves travel along the field line (as in the bouncing wave packet model).

It has been shown that the wave spectrum obtained from the nonlinear simulations is different from the linear theory predictions. In particular, nonlinear wave evolution creates waves with properties which can be far from those predicted using linear stability theory alone. Hence, it is important to consider the nonlinear development of the instability during its growth and saturation self-consistently. It has been found that the wave frequency gradually decreases with time and may fall below the local helium gyrofrequency, Ω_{He^+}, even in the

absence of He^+ ions. When He^+ species are added, the wave activity is sustained in the band below Ω_{He^+}, the source of free energy still being provided by the H^+ ion species. These results may explain the fact that EMIC waves with frequencies below the helium gyrofrequency are most often observed.

5.2 Future Work

The future work will concentrate on examining EMIC instability using observations and numerical simulations.

We have collected a preliminary catalog of magnetic field compression events during the THEMIS mission. In addition, we have identified another 38 compression events associated with high solar wind density based on GOES magnetometer data and OMNI solar wind data. We will examine the catalogue of these events and characterize them to the largest extent possible in terms of solar wind conditions (e.g., solar wind density, flow speed, IMF orientation). Then we will analyze EMIC waves in situ based on THEMIS magnetometer data and examine plasma composition and temperature anisotropy in the wave source region, and the spatial, temporal, and spectral wave characteristics.

We will further proceed with investigations of the conditions required for MeV electron and energetic proton precipitation due to EMIC waves using the NOAA satellite instrumentation in conjunction with ground and space-borne magnetometer data.

We will continue to use test particle simulations of the dynamical evolution of magnetospheric ion populations in a compressed magnetic field by adding a global electric field model. This will allow us to investigate the formation

of anisotropic ion distributions during disturbed geomagnetic conditions when the convection electric field is expected to be enhanced and therefore cannot be neglected.

Finally, we will continue examining EMIC wave properties through self-consistent PIC simulations. We will investigate the role of a cold plasma background in EMIC wave growth and will simulate EMIC wave growth and propagation along a magnetic field line where initial plasma parameters no longer remain constant but vary along the field line. This step will allow us to examine evolution of the wave spectrum under more realistic conditions, in particular, due to inhomogeneity along background magnetic field and compare the simulation results to observations.

Appendix A

Ultra Low Frequency Waves

Geomagnetic pulsations, i.e., ultra-low-frequency (ULF) waves cover the frequency range from the lowest the magnetospheric cavity can support up to the hydrogen gyrofrequency (~ 1 mHz to ~ 1 Hz). Micropulsations can be divided into two main classes: those of a regular and mainly continuous character (Pc), and those with an irregular pattern (Pi).

The table presents a classification scheme for the ULF waves according to the pulsation's type and period (Jacobs, J. A., Y. Kato, S. Matsushita, and V. A. Troitskaya, Classification of geomagnetic micropulsations, (1964), *J. Geophys. Res.*, 69(1), 180 - 181):

Class	Continuous					Irregular	
Type	Pc1	Pc2	Pc3	Pc4	Pc5	Pi1	Pi2
T (s)	0.2 - 5	5 - 10	10 - 45	45 - 150	150 - 600	1 - 40	40 - 150
f (Hz)	0.2 - 5	0.1 - 0.2	$(22 - 100)$ $\times 10^{-3}$	$(7 - 22)$ $\times 10^{-3}$	$(2 - 7)$ $\times 10^{-3}$	0.025 - 1	$(2 - 25)$ $\times 10^{-3}$

Table A.1: Classification of the ULF waves.

Appendix B

Coordinate Systems

B.1 Geographic (GEO) Coordinates

The origin of the geographic system is defined at the centre of the Earth. The x-axis lies in the Earth's geographic equatorial plane, but is fixed with the rotation of the Earth so that it passes through the Greenwich meridian ($0°$ longitude), the z-axis is parallel to the rotation axis of the Earth, and the y-axis completes a right-handed orthogonal set: $\hat{\mathbf{y}} = \hat{\mathbf{z}} \times \hat{\mathbf{x}}$.

B.2 Geodetic Coordinates

The geodetic coordinate system defines a position in terms of latitude and longitude at the ellipsoidal surface of the Earth. The origin is defined at the centre of the Earth. The geodetic longitude is the same as the geographic longitude. The local horizon is defined as the plane tangential to the Earth's surface at a given location. The local zenith is the direction away from the point on the Earth's

surface perpendicular to the local horizon. The geodetic latitude, ϕ is the angle between the local zenith and the equatorial plane. Except at the poles and the equator, ϕ differs from the geocentric latitude.

B.3 Geomagnetic (GM) Coordinates

The z-axis of this system is parallel to the magnetic dipole axis. The y-axis is perpendicular to the line connecting geographic poles. Finally, the x-axis completes a right-handed orthogonal set. Components of the geomagnetic field along the geomagnetic North-South and East-West directions are called the H- and D-component, respectively.

B.4 Field-Aligned Coordinates (FAC)

In this coordinate system, the z-axis is directed along the background (large-scale) magnetic field. The x-axis lies in the plane containing the z-axis and the vector from the centre of the Earth to the point of observation and is perpendicular to the z-axis. The y-axis is defined as a cross product $\hat{\mathbf{y}} = \hat{\mathbf{z}} \times \hat{\mathbf{x}}$.

B.5 Geocentric Solar Ecliptic (GSE) Coordinates

The origin is defined at the centre of the Earth. The x-axis of the GSE coordinate system is defined along the line connecting the centre of the Earth to the Sun and is positive towards the Sun, the z-axis is perpendicular to the ecliptic plane, and $\hat{\mathbf{y}} = \hat{\mathbf{z}} \times \hat{\mathbf{x}}$.

B.6 Geocentric Solar Magnetospheric (GSM) Coordinates

The origin is defined at the centre of the Earth. The x-axis of the GSM coordinate system is defined along the line connecting the centre of the Sun to the Earth and is positive towards the Sun. The y-axis is defined as the cross product of the GSM x-axis and the magnetic dipole axis; directed positive towards dusk, $\hat{\mathbf{z}} = \hat{\mathbf{x}} \times \hat{\mathbf{y}}$. The magnetic dipole axis lies within the xz plane.

Appendix C

Geomagnetic Activity Indices

C.1 Dst index

The Dst index represents the axially symmetric disturbance magnetic field at the dipole equator on the Earth's surface. The Dst index is based on hourly averages of the H-component of magnetic field measured at four near-equatorial observatories approximately evenly distributed in local time and is measured in nT.

Major disturbances in Dst are negative, namely decreases in the geomagnetic field. These field decreases are produced mainly by the ring current during magnetic storms. The neutral sheet current flowing across the magnetospheric tail makes a small contribution to the field decreases near the Earth and hence to Dst. Positive variations in Dst are mostly due to the magnetopause currents generated by the compression of the magnetosphere from solar wind pressure increases.

C.2 Kp **index**

The global Kp index serves as a measure of all irregular disturbances of the geomagnetic field caused by solar particle radiation within the 3-hour intervals. It is obtained as the mean value of the disturbance levels (relative to a quiet day) in the H- and D- field components, observed at 13 selected, sub-auroral stations both in the northern and the southern hemispheres. The name Kp originates from german "planetarische Kennziffer" (planetary index). Local disturbance levels are determined by measuring the difference between the highest and lowest field values during three-hourly time intervals for the most disturbed horizontal magnetic field component (H or D), converted into a local K index taking the values from 0 to 9 on a quasi-logarithmic scale, then normalized and averaged to get a global Kp index on a scale 0o, 0+, 1-, 1o, 1+, 2-, 2o, 2+, ... , 8o, 8+, 9-, 9o. $Kp < 4$ indicates relatively quiet to moderate geomagnetic conditions; $Kp > 7$ corresponds to active geomagnetic conditions.

C.3 AE **index**

The auroral electrojet (AE) index was introduced as a measure of global electrojet activity in the auroral zone. The AE index is derived from geomagnetic variations in the H-component recorded every minute at selected magnetometer stations along the auroral zone in the northern hemisphere. Among the data from all the stations at each given time (UT), the largest and smallest values are selected. The AU and AL indices are respectively defined by the largest and the smallest values of the superposed envelope for all stations selected (in

nT). The symbols, AU and AL, denote the upper and lower envelopes of the superposed plots of all the data from these stations as functions of UT. The difference, $AU - AL$, defines the AE index, and $(AU + AL)/2$, defines the AO index. The AU and AL indices are intended to express the strongest current intensity of the eastward and westward auroral electrojets, respectively. The AE index represents the overall activity of the electrojets, and the AO index provides a measure of the equivalent zonal current.